Theses and Dissertations

May 2016

Numerical and Experimental Study of Liquid Breakup Process in Solid Rocket Motor Nozzle

Yi-Hsin Yen
University of Wisconsin-Milwaukee

Follow this and additional works at: https://dc.uwm.edu/etd

Part of the Aerospace Engineering Commons, Mathematics Commons, and the Mechanical Engineering Commons

Recommended Citation

NUMERICAL AND EXPERIMENTAL STUDY OF LIQUID BREAKUP

PROCESS IN SOLID ROCKET MOTOR NOZZLE

by

Yi-Hsin Yen

A Dissertation Submitted in

Partial Fulfillment of the

Requirements for the Degree of

Doctor of Philosophy

in Engineering

at

The University of Wisconsin-Milwaukee

May 2016

ABSTRACT

NUMERICAL AND EXPERIMENTAL STUDY OF LIQUID BREAKUP PROCESS IN
SOLID ROCKET MOTOR NOZZLE

by

Yi-Hsin Yen

The University of Wisconsin-Milwaukee, 2016
Under the Supervision of Professor Ryoichi S. Amano

Rocket propulsion is an important travel method for space exploration and national defense, rockets needs to be able to withstand wide range of operation environment and also stable and precise enough to carry sophisticated payload into orbit, those engineering requirement makes rocket becomes one of the state of the art industry. The rocket family have been classified into two major group of liquid and solid rocket based on the fuel phase of liquid or solid state. The solid rocket has the advantages of simple working mechanism, less maintenance and preparing procedure and higher storage safety, those characters of solid rocket make it becomes popular in aerospace industry. Aluminum based propellant is widely used in solid rocket motor (SRM) industry due to its avalibility, combusion performance and economical fuel option, however after aluminum react with oxidant of amonimum perchrate (AP), it will generate liquid phase alumina (Al_2O_3) as product in high temperature (2,700~3,000 K) combustion chamber enviornment. The liquid phase alumina particles aggromorate inside combustion chamber into larger particle which becomes major erosion calprit on inner nozzle wall while alumina aggromorates impinge on the nozzle wall surface. The erosion mechanism result nozzle throat material removal, increase the

performance optimized throat diameter and reduce nozzle exit to throat area ratio which leads to the reduction of exhaust gas velocity, Mach number and lower the propulsion thrust force. The approach to avoid particle erosion phenomenon taking place in SRM's nozzle is to reduce the alumina particle size inside combustion chamber which could be done by further breakup of the alumina droplet size in SRM's combustion chamber.

The study of liquid breakup mechanism is an important means to smaller combustion chamber alumina droplet size and mitigate the erosion tack place on rocket nozzle region. In this study, a straight two phase air-water flow channel experiment is set up for liquid breakup phenomenon observation. The liquid water material in this experiment will play a comparison role as liquid alumina in high temerature enviornment.

The method proposed to control the liquid breakup size of liquid droplet is done by the means of changing the liquid properties of surface tension. The surface tenion of liquid plays an inportant role of providing major liquid droplet bounding pressure or Laplace pressure. By reduceing surface tension of liquid leads to lower Laplace pressure of droplet and result in less droplet dynamic stability which could be breakup under external pressure difference. The reduction of surface tension of liquid aluminum could be achieved by adding magnisium and strontium, it is reported that the surface tension reeducation level could reach 10%~15% when those additive mension above are adding to aluminum.

This study of liquid breakup mechanism include two major part, first part is straight two-phase channel experiment and simulation comparison which provide a validation work of CFD simulation performance when compare to experiment. Second part is single droplet breakup

experiment, in this experiment the relation of surface tension and liquid breakup behavior is carefully studied.

The straight two-phase flow channel experiment setting will enable to us to study the liquid breakup process in macro scale. The quantification method is achieved by analyzing high-speed camera image by MatLab image process code develop in UW-Milwaukee wind tunnel lab which extract data in images and provide information including liquid droplet count and size distribution, wave frequency and time averaging two-phase free boundary. It was found that liquid breakup mechanism proportional to gas-droplet velocity difference square, gas density and liquid droplet size and inverse proportional to liquid surface tension. The single droplet experiment part is provide a close up view of liquid breakup and prove the reduced surface tension will enhance liquid breakup activity.

In this study, we could observe the evidence of enhance liquid breakup activity by the reduced surface tension of liquid. Therefor the approach of reducing surface tension of Solid Rocket Motor (SRM) fuel reacting product is a high potential solution to SRM nozzle erosion.

Dedicated to my parents and my lovely fiancée Ying-Ling

for their unconditional love, support and encouragement

TABLE OF CONTENTS

LIST OF FIGURES

xvi

LIST OF TABLES

LIST OF NOMENCLATURE

A   =   Area

c   =   Speed of sound

c_p =   Specific heat

D   =   Diameter

E   =   Total energy

e   =   Eccentricity

F   =   Force

g   =   Gravity

G   =   LES three dimensional filter function

H   =   Enthalpy (chemical reaction)

I_t =   Impulse

I_{sp} =   Specific impulse

k   =   temperature in Kelvin

K   =   Thermal conductivity of fluid

L   =   characteristic length scale

$\dot{m}$ =   Mass flow rate

M   =   Mass

Ma   =   Mach number

$\hat{n}$ =   Normal vector

P   =   Pressure

$P_{Lap.}$ =   Yong Laplace pressure from surface tension

P_{stag} =   Stagnation Pressure

Pr   =   Prandtl number

q_i =   Heat flux

r   =   Radius of droplet

s   =   Constant for approximate equation of ellipsoid surface area

$S_{a,b,c}$ =   Semi-principal axes length of ellipsoid

T   =   Temperature

t   =   Time

$\overline{u'}$ =   time averaged fluctuating velocity component in Reynolds Stress Model

u, U =   general velocity expression in RANS, RSM, LES

v, V	=	general velocity expression in Tsiolkovsky rocket equation
Re	=	Reynolds number	$\equiv Re = \rho v L / \mu$
We	=	Weber number	$\equiv We = (\rho v^2 L) / \sigma$

Greek

α	=	particle velocity to combustion gas velocity ratio
α_n	=	volume fraction of n th phase in VOF model
β	=	thermal expansion coefficient
δ_{ij}	=	Kronecker delta
ϵ_{ikm}	=	3rd Levi-Civita symbol
θ	=	temperature in Reynolds Stress Model
μ	=	viscosity
ρ	=	density of fluid
σ	=	surface tension
τ_{ij}	=	viscous stress
Ω	=	angular velocity

Subscript

i, j, k   Unit vector

n n th phase in VOF model

ACKNOWLEDGEMENTS

I also really thanks to my lovely parents and my two younger sisters. For their love and support throughout my life and give me strength to the journey of science exploration.

Last but not least, I would like to thank my loving fiancée Ying-Ling for her personal mental support, encouragement and great patience during my pursuit of this PhD.

1 Introduction

1.1 Rocket

Rocket is a mechanism which provides thrust for aerial vehicle like aircraft, missile, and spacecraft. Rocket engine works by action and reaction and obtain propulsion by discharge high speed exhaust gas in the opposite direction in accordance with Newton's third law [1]. The detailed derivation of Tsiolkovsky Equation is in chapter 0 which is the well-known equation describe the relation of rocket velocity to fuel mass and exhaust gas velocity in rocket industry. Although the Chinese used rockets over 800 years ago, the development of modern rocket propulsion took place in 20th century [2]. Rocket propulsion system could be classified by the type of energy source of chemical, solar or nuclear propulsion system. The rocket technology nowadays applies chemical propulsion system which is currently most mature and stable technology. By mixing and ignite the fuel and oxidizer in combustion chamber of rocket, they will release energy in the form of heat, the gas could heat up to the temperature level of 2500 to 4000K after combustion. The heated up gas subsequently expand in combustion chamber and accelerated to high velocity of 1800 to 4000 m/sec. By directing the high velocity exhaust gas to the opposite to the intended direction, rocket will get propulsion based on Newton's third law. According to physical state of the propellant there are two major classes of chemical rocket propulsion system which are liquid propellant rocket engines and solid propellant rocket motors, which means the propellants are in liquid and in solid state respectively.

1.2 History

In the first century, the Chinese discover the gunpowder made from mixture of saltpeter, sulfur and charcoal dust could be ingredient of firecracker which is use during religious festivals. Some firecracker failed to explode but propelled by discharged fire and gas from one end of firecracker which become the first form of rockets [3] . The first dated reporting the use of rockets was the war between Jin dynasty and Mongol during the battle of Kai-Feng in 1232. Figure 1-1 is the illustration of rocket arrows in the basket documented in Chinese military book of Wubei Zhi. The rocket performance didn't get significant improve until early 20th century, pioneers like Konstantin Tsiolkovsky, Robert Esnault-Pelterie, Robert Goddard and Wernher von Braun et al contributed the rapid growth of rocketry. Modern rocket technology is based on the research and development during this period of time.

Figure 1-1 Early Chinese rocket documented in Wubei Zhi in 17th century [4]

1.3 Classification of Propulsion

By power source, the rocket could be classified into nuclear, solar, electro and chemical rocket. Most of current rockets are chemical rocket and could be further classified in to two categories, solid fuel rocket and liquid fuel rocket based on the liquid or solid states of propellant. Both rockets have their own characters, advantages and disadvantages.

1.3.1 Solid Fuel Rocket Motor

The propellant of solid rocket motor (SRM) is contained and stored directly in the combustion chamber. A modern solid rocket booster for space shuttle is shown in Figure 1-2, it is less complicate and less moving part in final assembly compare to a liquid rocket engine. The preparation of the propellant require mixing of solid fuel and oxidizer in fine grain size ranging from 5 to 500μm depends on designed burn rate, fuel will burn faster with finer grain size [5]. It will be then mixed with binder (usually Polyethylene) in the manufacture process to provide the structure strength of propellant and held ingredients together, the process of mixing as shown in Figure 1-3 (a). The mixed propellant then will be mold casted and solidified in combustion chamber and become final product of fuel block as shown in Figure 1-3 (b). The fuel block geometry is based on design propulsion thrust, more reaction area enhance the thrust and reduce the burn time. Several different type of cross-section geometry is demonstrated in Figure 1-4. Fuel blocks with a cylindrical channel (a) develop their thrust progressively due to increasing reaction area inside combustion chamber, star profile (b) cross-section develops a relatively constant thrust which decreases slowly to zero thrust as fuel burned out.
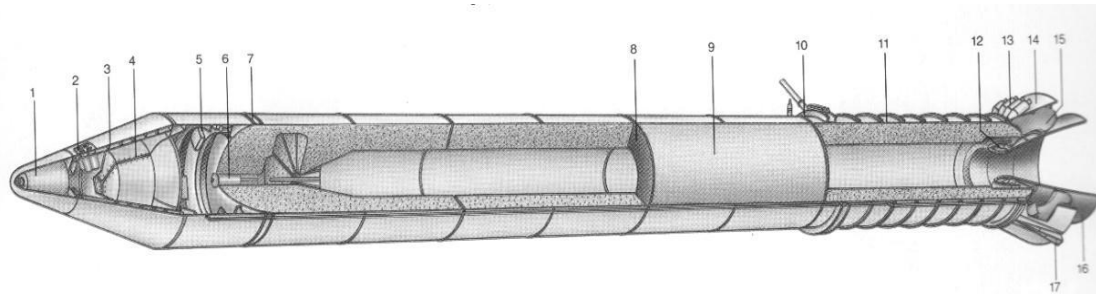
Solid Fuel Rocket Booster (SRB)

1. Primary parachute
2. Forward separation rockets
3. Flotation system
4. Principal parachutes
5. Platform for electronic equipment
6. Pyrotechnic ignition
7. Fixing harness to external tank
8. Joint between solid fuel segments

9. Solid fuel segment
10. Fixing harness to external tank
11. Solid fuel block
12. Articulated joint for nozzle
13. Rear separation rockets
14. Skirt
15. Thermal insulation
16. Diffuser nozzle
17. Anchor point

Figure 1-2 Solid rocket booster of space shuttle [4]

(a)

(b)

Mixed solid fuel (Al) and oxidizer (NH_4ClO_4) with binder material inside a mixing tank

Cross-section of solid fuel block
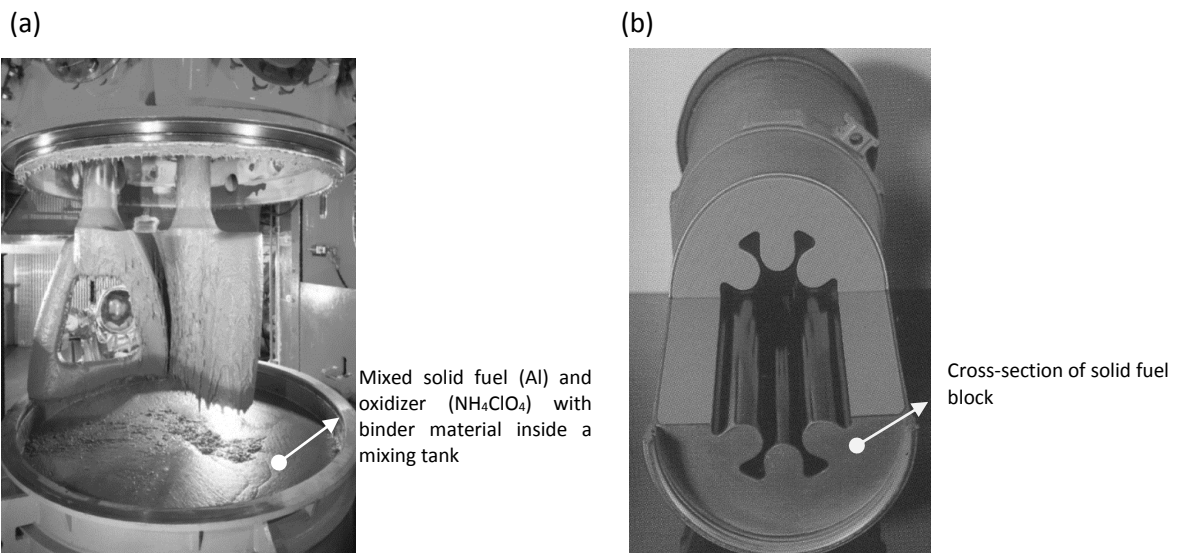
Figure 1-3 (a) Mixing process of solid propellant [6] (b) Cross-section of solid fuel block [7]

(a)

(b)
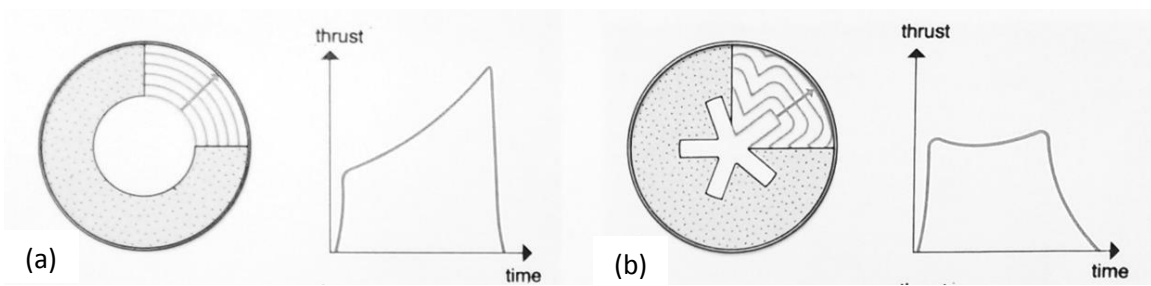
4

The advantages of solid rocket motor include (1) long time of storage of 5 to 20 years (2) no moving part makes SRM relatively simple and easy to apply, and require little servicing. However, some disadvantages company this solid propellant are (1) the thrust cannot be varied in flight and (2) nozzle erosion by solid fuel combustion product.

(a)   (b)   Pocket region

Fixed nozzle (simplest)   Submerged nozzle (shorter)

Figure 1-5 (a) Fixed nozzle and (b) Submerged nozzle

The nozzle layout in SRM also could be classified into fixed muzzle and submerged nozzle as shown in Figure 1-5. Fixed nozzle (a) is a simple and strait forward design, submerged nozzle (b) has been widely utilized in SRM for reducing motor length and weight, submerged nozzle also provides a pocket for accumulation of molten alumina slag (Al_2O_3) which can cause flight stability problems [8].

1.3.2   Liquid fuel rocket

Liquid propellant rocket engines use pressurized liquid propellants feed to combustion chamber of rocket nozzle and gain thrust from ejecting high velocity gas. The idea of this technology first appears in publication of Konstantin Tsiolkovsky in 1903 [9] and the first liquid rocket flight is realized by Robert Goddard in 1926, the world first rocket as shown in Figure 1-6 (b). The liquid

rocket engine system is schematically shown in Figure 1-6 (a). The liquid fuel and oxidant feed from fuel and oxidizer tank to a turbine fuel/oxidizer pump. The turbine pump pressurized the liquid fuel/oxidizer to overcome high pressure from combustion chamber and inject both liquid into it to react and formed hot gases then accelerated to high speed and finally discharged high speed gas to gain thrust. The turbine pump also use same source of fuel and oxidizer from branched fuel/oxidizer pipe, therefore the thrust could be adjust by controlling the fuel flow rate into turbine pump combustion chamber. The fuel also act as coolant to cool temperature down on the nozzle wall before it entering the nozzle combustion chamber, so this mechanisms helps the nozzle avoid from thermal damage and also preheat the fuel which enhance the combustion temperature and exhaust gas velocity.

(a)
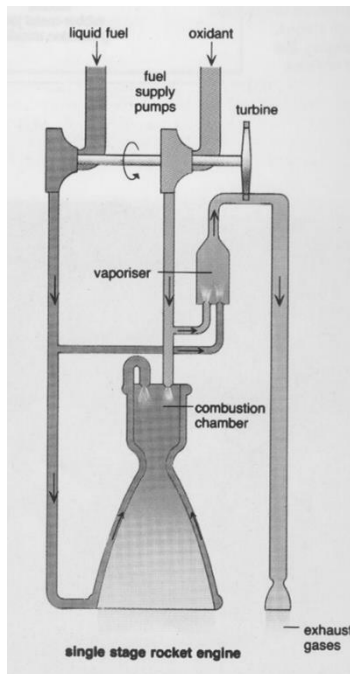
(b)
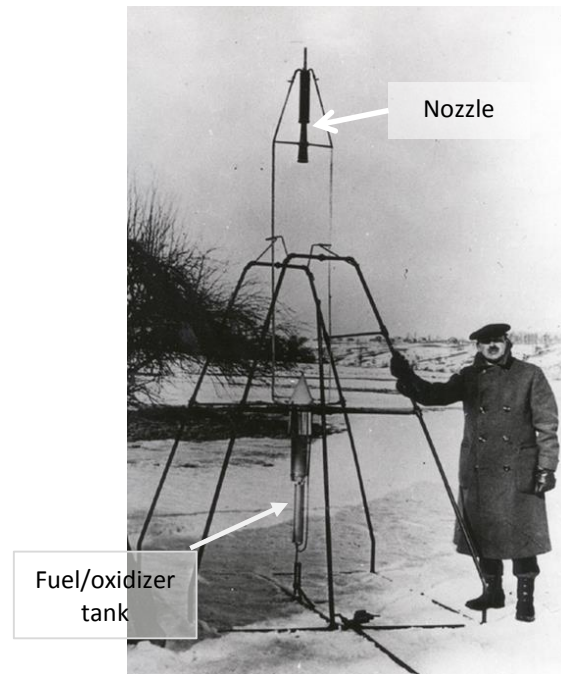
Figure 1-6 (a) the schematic of liquid fuel rocket [4] (b) Robert H. Goddard create the world's first liquid fuel rocket [10]

6

The advantages of liquid rocket engine are (1) the adjustable thrust: the thrust control can be achieve by limiting the fuel flow into combustion chamber, some liquid rocket engines permit repetitive operation and can be started and shut off at will, this feature provide the flexibility of space travel and trajectory control. (2) Liquid rocket engine suffers on solid particle erosion, it is possible to operate liquid rocket for more than one hour if fuel supply is enough due to less erosion occur on the nozzle part. However some disadvantages of liquid rocket engines are (1) complexity of the system: the assembly of many parts of fuel/oxidizer pipes, turbine pump, valves cooling pipes, gear box increased the chance of failure. (2) Liquid propellant is not easy to preserve, therefore liquid propellant only inject to propellant tank before launch. If launch is canceled, propellant need to be removed from the rocket propellant tank.

1.4 De-Laval Nozzle

De-Laval Nozzle or convergent-divergent nozzle (C-D nozzle) is a propulsion mechanism which is widely used for rocket motor due to its high performance in rate of momentum change or high velocity discharge of matter. The nozzle was developed by Swedish fluid mechanic engineering Gustaf de Laval and named after his contribution to isentropic flow study [11].The nozzle is a duct shape tube with designed narrower channel passage in the middle as shown in the Figure 1-7. The nozzle named after a Swedish engineer Gustaf de Laval who develop convergent-divergent nozzle for steam turbine [12].

Fluid velocity direction
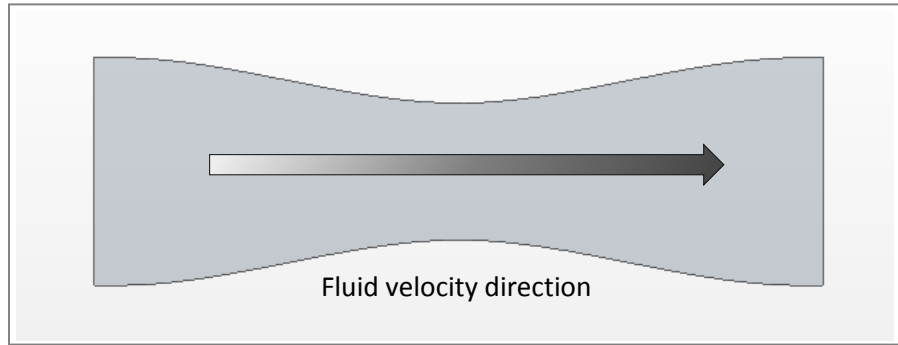
Figure 1-7 Geometry of de-Laval nozzle

1.4.1 Shock Diamond and Velocity Contour

A velocity contour of a de-Laval nozzle simulation is shown in Figure 1-8, we could observed that the air velocity reaches Mach 1 at throat and keep accelerating to max velocity at certain point, the location of max velocity is depend on the nozzle inlet pressure and temperature, after the point of maximum velocity we could observe the shock diamond which is the standing wave patterns of compressible fluid pressure adjustment process between high pressure inlet and low pressure environment. Shock diamond is the signature of supersonic jet since it only appears when compressible fluid reaches more than Mach 1, another Schlieren photography of shock diamond is also shown in Figure 1-9.
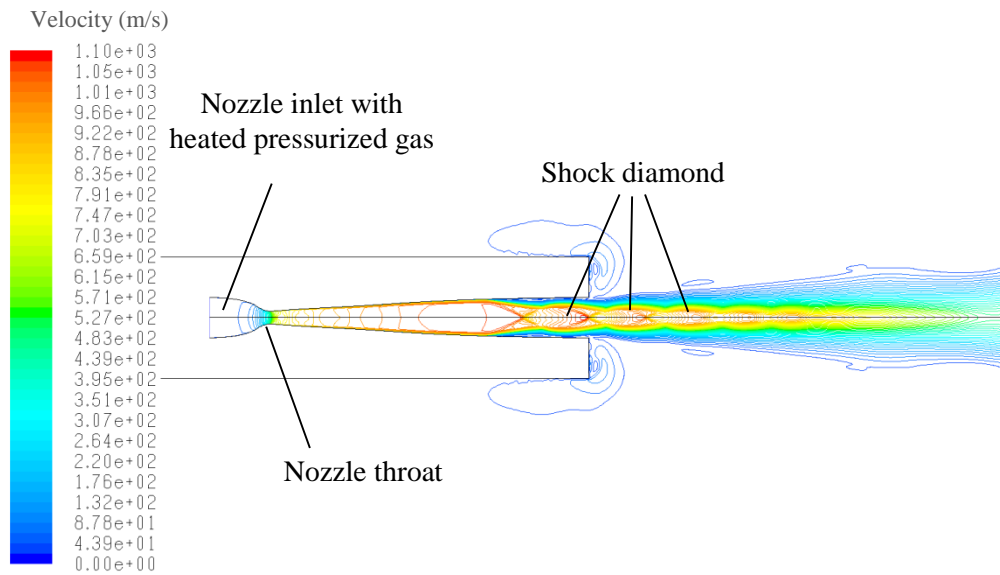
Figure 1-8 Velocity contour of a de-Laval nozzle [13]
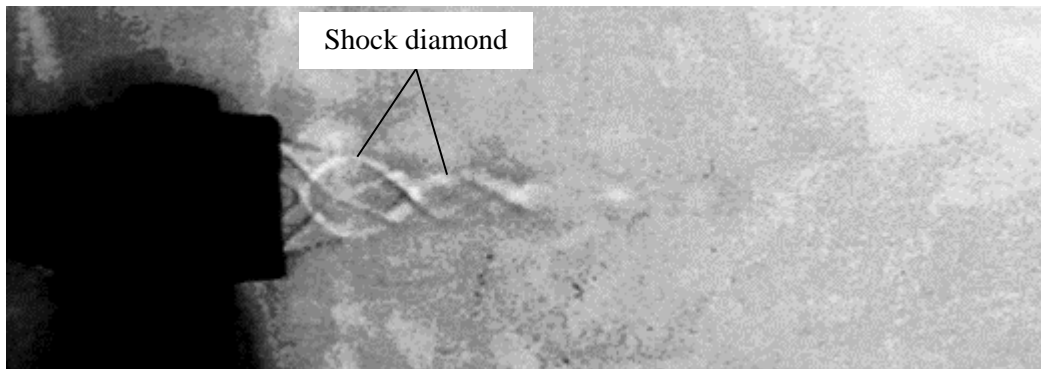
Figure 1-9 Schlieren photography of shock diamond (Photography by UW-Milwaukee Wind Tunnel Lab).

The difference of liquid and solid rocket could be distinguished from exhaust gas, one example of space shuttle is shown in Figure 1-10. Space shuttle has three main liquid fuel engines mount on the aft of shuttle fuselage and support with two large solid rocket boosters (SRB) on both side of orange external tank (ET). It is clear to tell the shock diamond from the exhaust of liquid rocket motor, however it is hard to observe the shock diamond from the exhaust of solid rocket booster due to the much brighter alumina particles.
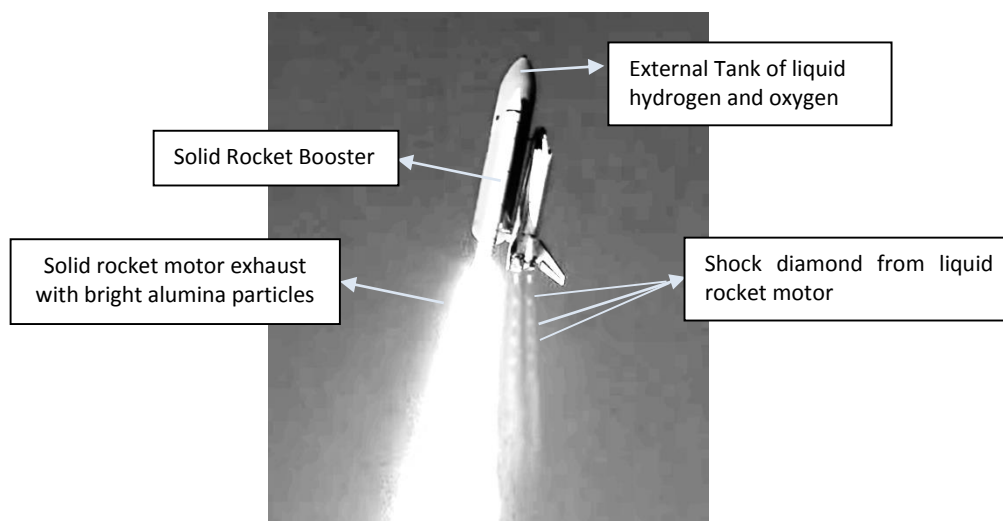
Figure 1-10 Space Shuttle use both solid and liquid motor [14]

1.5 Solid Fuel Chemical Reaction

The chemical equation of aluminum fuel and ammonium perchlorate (AP: NH_4ClO_4) is denoted in equation (1), after reaction, the aluminum fuel will release enthalpy 1670 kJ per mole in the form of heat [15]. The table of molar mass of reactant and product is denoted in Table 1-1. We could calculate the mass percentage of fuel, oxidizer and products based on this table.

$$6NH_4ClO_{4\,(s)} + 10Al_{\,(s)} \rightarrow 5Al_2O_{3\,(l)} + 3N_{2\,(g)} + 6HCl_{\,(g)} + 9H_2O_{\,(g)}$$

(1)

$$\Delta H = -1669.8 \text{ kJmol}^{-1}$$
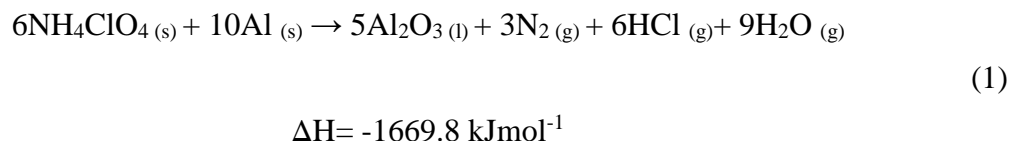
Table 1-1 Molar mass of reactant and product

	NH4ClO4	Al	Al2O3	N2	HCl	H2O
Molar Mass (g/mol)	117.49	26.98	101.96	28.013	36.46	18.015

10

Figure 1-11 (a) and (b) is the mass percentage of fuel, oxidizer and product of combustion in equation (1) without concerning the mass and volume fraction of binder material like polyethylene (PE), more than 50% of mass in product is contribute by alumina, however the volume percentage of alumina is much less in the exhaust gas. The volume percentage of equation (1) is shown in Figure 1-12, we could observed that despite alumina weight more than 50% in mass, but the volume percentage from alumina weight only 0.17%. Figure 1-13 is the volume ratio of all reactant and product to Aluminum fuel, in this figure, aluminum volume is set to be one. AP is 3.6 times more than aluminum in terms of volume in the left hand side of equation. In the product side, assume the combustion pressure is 4.8MPa and temperature is 3,000k, most of the volume are contribute by water vapor, hydrochloric acid vapor and nitrogen gas, the volume percentage of alumina will be 0.17% in the product side.
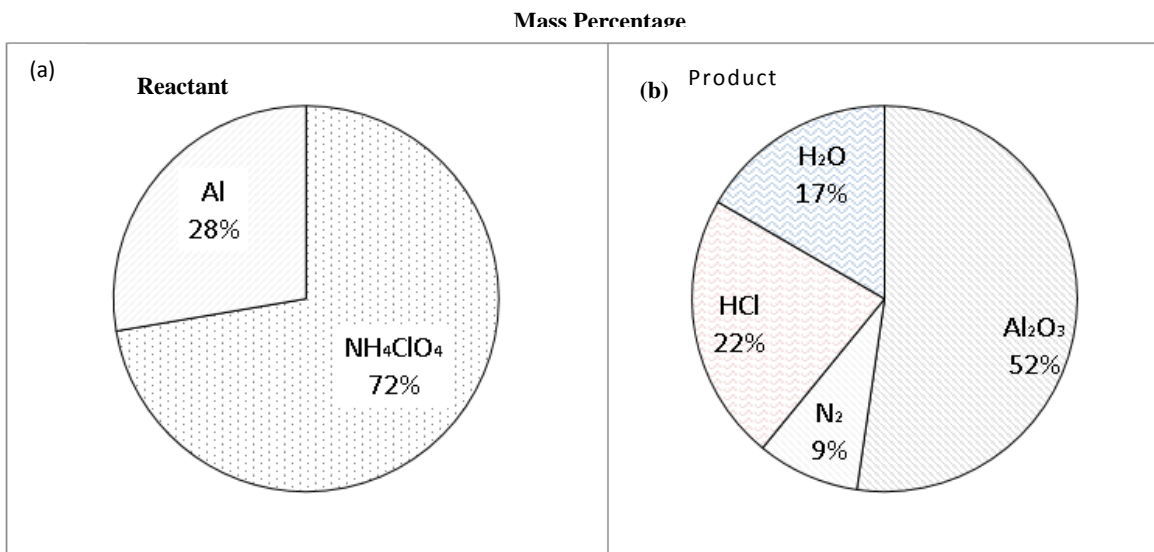
Mass Percentage

Figure 1-11 Mass percentage of (a) Fuel and Oxidizer (b) Product of combustion

11

Volume Percentage

(a) **Reactant**

Al
22%

NH4ClO4
78%

(b) Product

Al2O3
0.17%

N2
18%

H2O
54%

HCl
28%
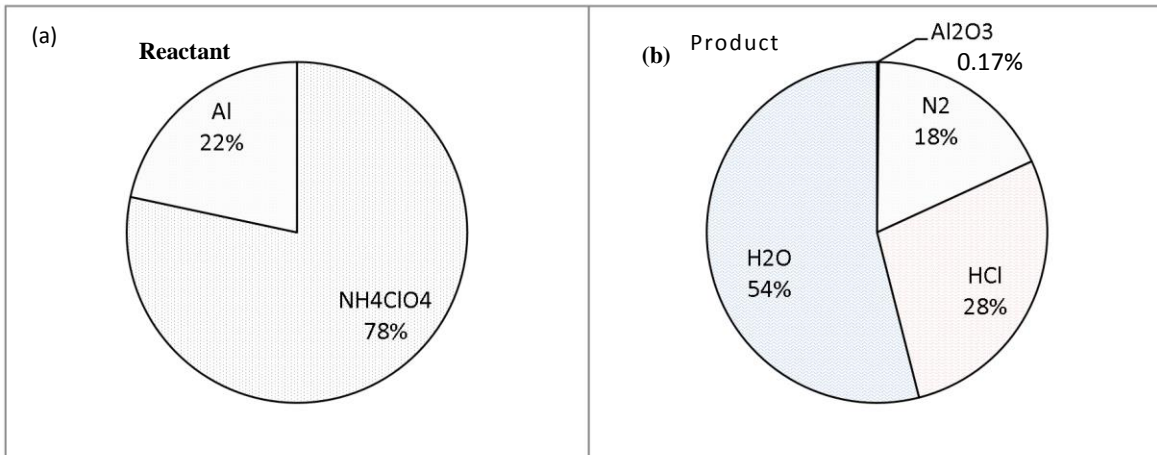
Figure 1-12 Volume percentage of (a) Fuel and Oxidizer (b) Product of combustion

(a)

(b)

Volume Ratio to Al

1.0

3.6

$\square$ Al
$\square$ NH$_4$ClO$_4$

403.3

208.3

134.4

1.3

$\square$ H$_2$O
$\square$ HCl
$\square$ N$_2$
$\square$ Al$_2$O$_3$
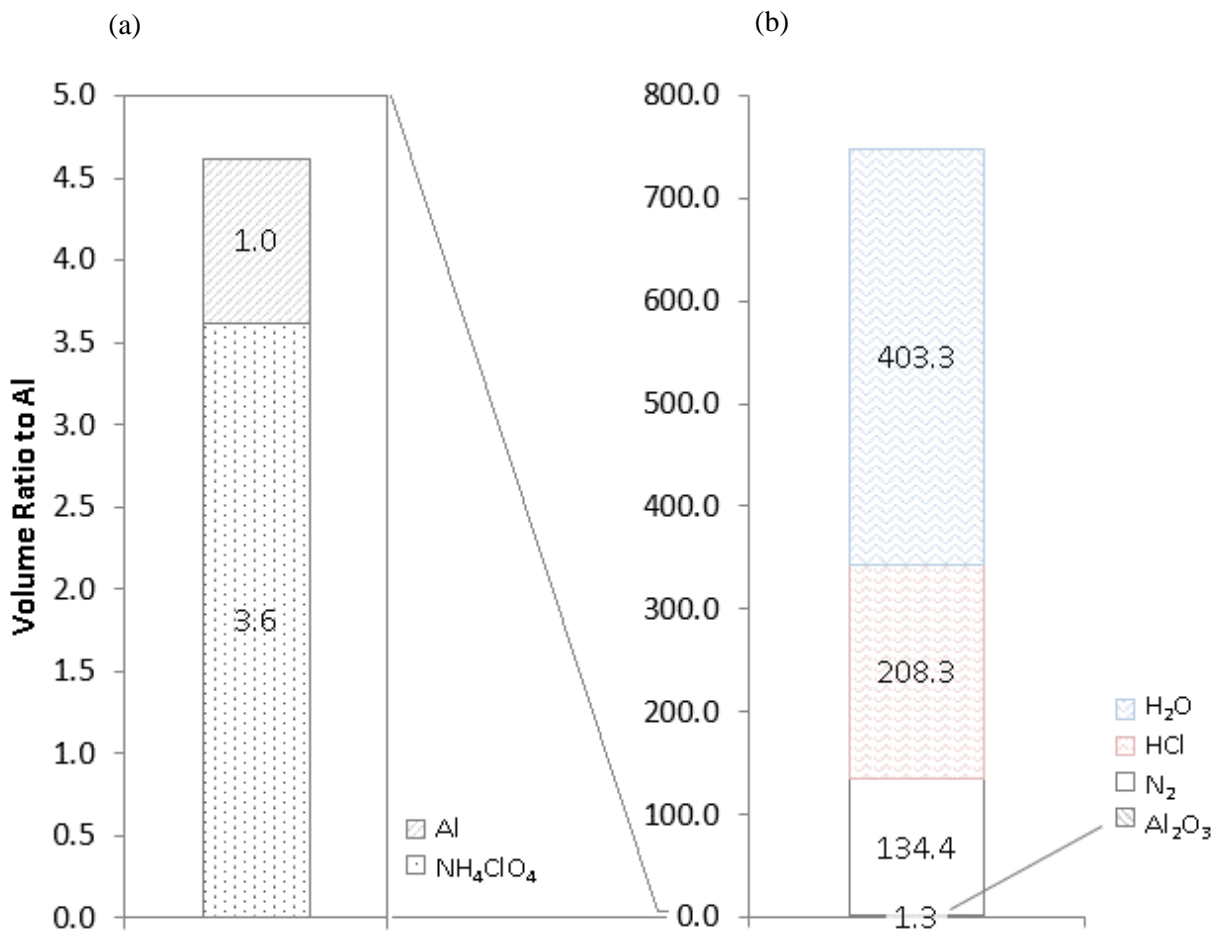
Figure 1-13 Volume ratio to Aluminum of (a) Fuel and Oxidizer (b) Product of combustion under pressure of 4.8MPa and temperature of 3,000k

1.6 Challenges of Solid Rocket

Solid rocket has the advantages of long period of storage, simple mechanism due to no moving part, however those advantages come from solid fuel lead to unavoidable challenges of liquid alumina particle erosion on the inner wall of the solid motor. The study from Kim, Laredo and Netzer [16] applied multiple-wavelength transmission measurement technique to obtain the Sauter mean diameter and the particle size distribution of alumina particle at the nozzle exit. The particles in the edge of the plume has diameter of 0.15±0.006µm, although the particle size distribution outside the nozzle could be investigated nowadays, the particle distribution inside SRM combustion chamber still need investigate. Also, the erosion rate for the submerged nozzle are not well predicted [8] as well. By understand the liquid particle breakup mechanism will help us to understand particle distribution inside combustion chamber and avoid nozzle erosion mechanism and further improve the performance of solid rocket motor.

1.7 Breakup Mechanism

In order to understand the erosion on solid rocket motor, we need to study the liquid breakup behavior of liquid alumina which might be a potential approach to protect nozzle geometry during flight.

1.7.1　Droplet Pressure Balance and Weber Number

As shown in Figure 1-14 (a) liquid surface tension (yellow arrow) which holds the liquid in shape of spherical in order to maintain least surface potential, the additional pressure inside droplet caused by surface tension is described as Laplace pressure. Figure 1-14 (b) is when air interact with droplet with certain speed, the stagnation pressure (black arrow) act on the surface of droplet and force it to deform. Whether the droplet will breakup or not depends on the balance of those two major pressures.
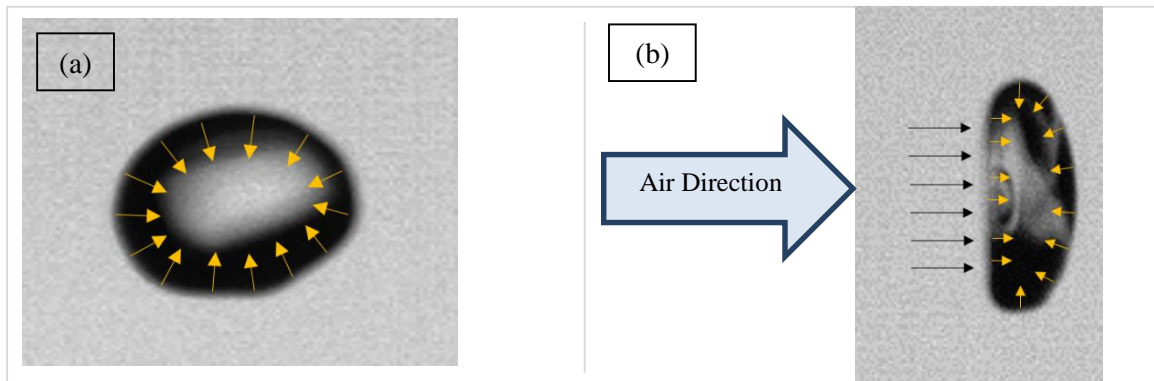
Figure 1-14 Laplace pressure and Stagnation pressure (Photography by UW-Milwaukee Wind Tunnel Lab)

The pressure difference between inside and outside of droplet caused by surface tension is described as Laplace pressure which could be expressed by Young-Laplace equation shown in the following.

$$\Delta P = -\sigma \, \nabla \cdot \hat{n} \tag{2}$$

Where σ is surface tension, the Laplace pressure is the product of surface tension and divergence of normal vector of droplet's surface. After expand Young-Laplace equation in spherical coordinate we could express the Laplace pressure in equation (3), and where r is radius of droplet

$$\Delta P = \frac{2\sigma}{r} \qquad (3)$$

The stagnation pressure of moving air which causes the deformation of droplet is described by equation (4)

$$P_{\text{Stag.}} = \frac{1}{2}\rho_{\text{air}}v^2 \qquad (4)$$

where ρ_{air} is density of air and v is the relative air velocity to droplet. By rearranging equation (4) and (5), we could find the breakup pressure ratio (BPR) of stagnation and Laplace pressure shown as following

$$\text{BPR} = \frac{P_{\text{Stag.}}}{P_{\text{Lap.}}} = \frac{\rho_{\text{air}}v^2 r}{4\sigma} \qquad (5)$$

In which the breakup pressure ratio is proportional to density of air, square of two-phase velocity difference, radius of droplet and inverse proportional to surface tension of liquid. We also found that the description of breakup pressure ratio is similar to Weber Number which described in equation (6).

$$\text{We} = \frac{\rho_{air} v^2 r}{\sigma} \tag{6}$$

Weber number characterizes the tendency of liquid to breakup due to balance between gas-phase inertia to liquid surface tension force [17]. When the Weber number is large, the surface tension is dominated by the deforming inertial forces of air, which leads to the liquid breakup process. Weber number of 5 or greater usually marks the threshold of breakup.

1.7.2 Droplet Breakup Process

A single droplet breakup process is demonstrated in Figure 1-15, the droplet has a diameter of 1.5mm and V_{air} blowing the droplet from right hand side with velocity of 30m/s. The process start in Figure 1-15 (a) with Weber number value of 23. In Figure 1-15 (b) and (c) the droplet star to interact with 30m/s of air and air stagnation pressure start to deform the droplet. In Figure 1-15 (d) we could observe the air blow into the center of droplet and form into bubble. In Figure 1-15 (e) and (f) the bubble burst into smaller droplet with main droplet body from into torus shape. In Figure 1-15 (g) to (i) the torus shape breakup into smaller droplet with diameter ranges from 0.25mm to 0.5mm, the corresponding Weber number ranges from 4 to 8.

16

V_air = 30 m/s Droplet size: 1.5mm		
Air direction → ⬤ ↕1.5mm		
(a) time= 0.0ms	(b) time= 0.5ms	(c) time= 1.5ms
(d) time= 2.5ms	(e) time= 3.0ms	(f) time= 3.5ms
(g) time= 4.0ms	(h) time= 4.5ms	(i) time= 5.5ms
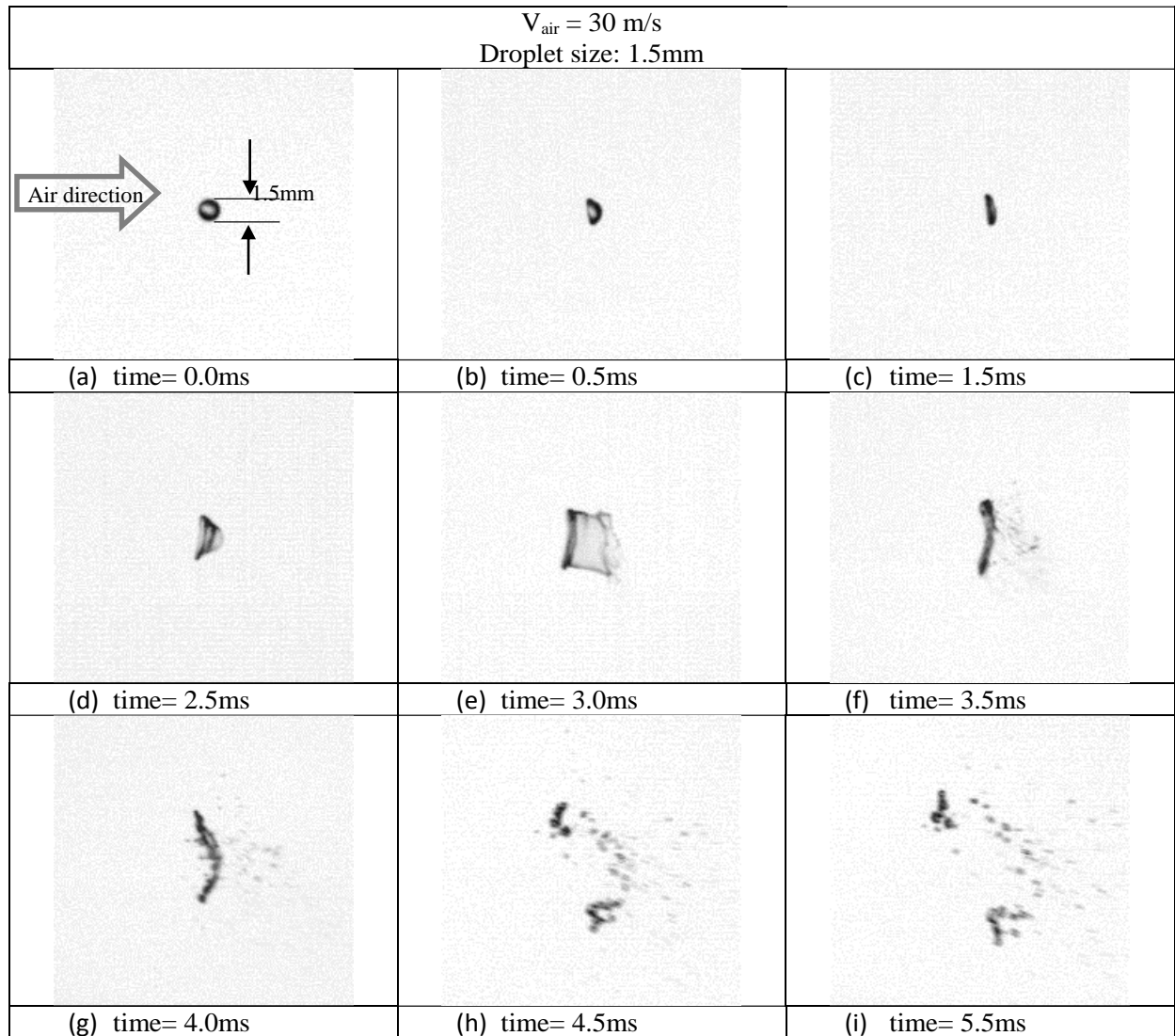
Figure 1-15 Single droplet breakup mechanism (Photography by UW-Milwaukee Wind Tunnel Lab)

2 Literature Review

2.1 Solid Fuel

Different solid fuel been used for solid rocket motor for their high flame temperatures which direct affect the specific impulse, reaction temperature and exhaust gas velocity. Table 2-1 is the list of the burning flame temperatures, price and remarks of different metal fuel, Beryllium solid fuel standout in terms flame temperature and specific impulse, the technology with of using powdered beryllium has been experimentally proven, however beryllium is highly toxic powder when human inhaled and it is also category 1 carcinogens [18], the application of beryllium is not an ideal fuel for public health and for environment [19]. Boron fuel is lighter than aluminum and has a high melting point (2577K), Boron powder is difficult to burn, however it can be oxidized at reasonable efficiency if the boron particle size is very small and can be used as a burning catalyst with some composite propellants [20]. The most widely use solid fuel is powdered aluminum particle with diameter of 5 to 60 μm. Small aluminum particle is mildly toxic if inhaled. In general aluminum is safe, less environmental impact and inexpensive which becomes a better option of fuel for current solid rocket motor. After aluminum burn, the oxide is in liquid form during combustion and solidifies on the nozzle wall as the exhaust gas temperature drops. The alumina molten slag can also accumulate in pockets of submerged nozzle and deposit on walls inside the combustion chamber [21], more detail will be covered in chapter 2.2.

Table 2-1 Metal Fuel Combustion Temperatures [22] [23] [24]

Metal	Flame Temperature (K)	Density (Kg/m^3)	Price (USD/MT)	Remarks
Al	3908	2700	1,700	High performance, Low cost
B	3786	2400	4,960	Inefficient combustion
Be	4210	2300	745,000	High performance, Toxic
Li	2846	534	6,900	Moderate performance
Mg	3229	1750	4,600	Clean propellant application
MgAl	3807	N/A	N/A	Combined

2.2 Aluminum Based Propellant

Typically Propellant of solid rocket motors (SRM) use aluminum as fuel and ammonium perchlorate (AP) as oxidizer which is the most widely used oxidizer in solid propellants due to compatibility with the other propellant material, quality uniformity and availability [25], both fuel and oxidizer are mixed with polyethylene (PE) binders which hold the fuel mixture together and provide structural strength, the chemical reaction of aluminum and AP is documented in equation (1), Aluminum based propellant is widely use due to its high energy density per unit volume [26] [27]. Table 2-2 is the list of comparison of different fuel compound percentage in weight.

Table 2-2 Optimum combustion temperature (T_c) and I_{sp} for Solid Propellants with Metal Fuels [22]

Binder	Oxidizer	Metal Content	Tc(k)	Theoretical I_{sp} (sec)
15% Polyethylene	65% AP	20% Al	3185	265
15% Polyethylene	67% AP	18%Li	2628	258
15% Polyethylene	70%AP	15%Be	3239	284
15% Polyethylene	60%AP	25%Mg	2926	258
15% Polyethylene	71%AP	14%B	2740	256

2.3   Alumina Properties

The operating environment of the combustion chamber of an SRM is extremely severe with temperatures reaching 3,000K to 3,500K and pressure over 2.0 x 10^7 Pa; alumina has an observed melting temperature of 2,345K and an evaporation temperature of 3,250K at atmospheric condition. Thus, the alumina exists as mostly liquid in the combustion chamber and in the nozzle with some evaporation possibly occurring. Sometimes the alumina film becomes re-entrained near the nozzle throat and impinges on the diverging section of the rocket nozzle causing erosive damage. Because of these effects, a better understanding of the phenomena is important for designing an SRM.

In gas-liquid two-phase flow, liquid droplet breakup behavior can be observed. Hinze [28] [29] proposed using non-dimensional quantities such as the Weber number to characterize the breakup process. Large droplets have relatively large cross-sectional areas that lead to higher aerodynamic forces acting on them compared to the weaker surface tension that is attempting to hold the droplet in shape, so a higher Weber number for a droplet indicates a higher likelihood of breakup. The liquid alumina breakup mechanism in an SRM is more complicated than the breakup of droplets. The liquid alumina accumulates and attaches on the wall of the de Laval nozzle forming a liquid film which is shear driven and interacts with the surrounding air. The liquid film forms waves due to the shear, and breakup occurs at the crests of the waves. The breakup level increases with the surrounding gas velocity; more liquid breakup in the nozzle throat reduces the liquid alumina droplet size, resulting in easier discharge of droplets by the carrier gas instead of the alumina adhering to the nozzle wall.

2.4 Alumina Slag and Agglomerates

The combustion of aluminum based solid propellant produces Al_2O_3 liquid droplets. Those liquid droplets are the source of slag material which remain in the combustion chamber and will lead to a rocket performance loss and possible damage to insulation surface due to excessive heat. Figure 2-1 is the close up view of the aft section of space shuttle SRM shown earlier in Figure 1-2, the submerged nozzle pocket region is where alumina slag accumulation take place. Figure 2-2(a) shows the flow recirculation region in the submerged nozzle near the start of the burn, the propellant burn prevent alumina droplet entering the pocket of submerged nozzle. Figure 2-2(b) shows the corresponding conditions near the end of the motor burn, less sweeping action due to few propellant in the pocket region result deposition takes place near the end of motor burn [21].

Submerged nozzle pocket region
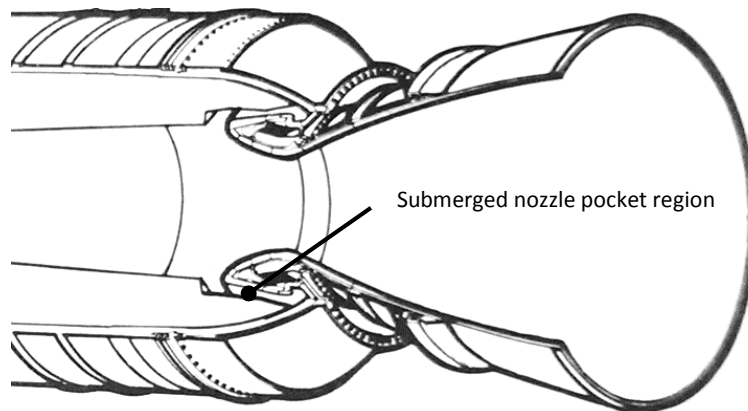
Figure 2-1 the close up view of the aft section of space shuttle SRB [30]
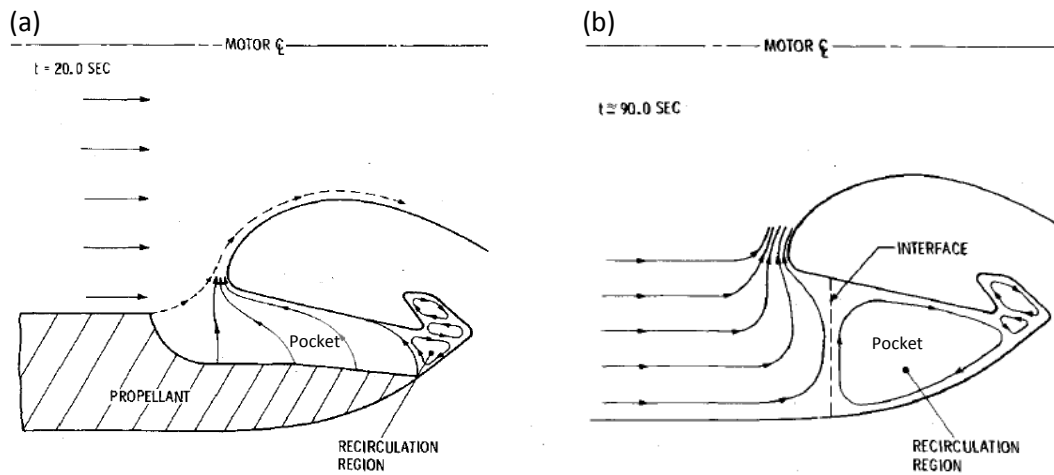
Figure 2-2 Flow in the submerged nozzle region (a) near the start of the burn (b) near the end of the burn [21]

After aluminum and AP's reaction the byproduct Al_2O_3 or alumina becomes a performance issues. Alumina (Al_2O_3) form particles in different size in the combustion chamber and impinge along the inner wall of nozzle. The chemical and mechanical erosion caused by the alumina particles is a particular problem to be avoided in an SRM because of the effects on ballistic performance [31]. Most erosion is carried out in the vicinity of the nozzle throat, changing the nozzle throat geometry. A 5% increase in SRM throat area due to erosion is considered excessive because of the resultant velocity decrease and loss of nozzle performance [32]. The velocity contours of SRM flow field are affected by the multiphase particle motion which further limits the performance, according to a study by Nayfeh and Saric [33]. Moreover, because of the geometry of the motor, molten alumina agglomerates can form resulting in two-phase flow losses [21] [34] [35]. These agglomerates lower the propulsive efficiency of the exhaust flow because the agglomerates do not expand in the nozzle and also create a drag force on the flow [36] [37]. Depending on the alumina

22

particle size and the alumina particle-gas mixture percentage, two-phase flow losses can reduce the propellant specific impulse by as much as 6% [38] [39]. For liquid fuel rockets, the geometry of De-Laval Nozzles are optimized for peak performance, however, the nozzle design of solid rocket motors cannot take advantages of optimize nozzle geometry due to particle impingement along the inner wall of De-Laval Nozzles [40]

For solid alumina agglomerate flow in the gas stream, the agglomerate size depends on many factors of propellant grain size, fuel burn rate, chamber pressure, and aluminum concentration. Overall, the chamber pressure effect is one of the most dominate parameters, as combustion pressure increases, the agglomerates becomes smaller [41] [42]. Caveny and Gany performed an experimental study using a two-dimensional windowed rocket motor to observe the breakup mechanism of alumina agglomerates with throat section diameter of 3×3 mm [43]. In this experiment result shows the agglomerate breakup usually occurs when critical Weber number of approximately 28 is reached. Figure 2-3 shows the alumina agglomerates breakup steps. In first sequence, a single agglomerate of 1040μm enters nozzle with gas velocity of 93m/s, it then breakup in the nozzle. Similar situation for larger and smaller agglomerates breakup steps shown in second sequence as well.
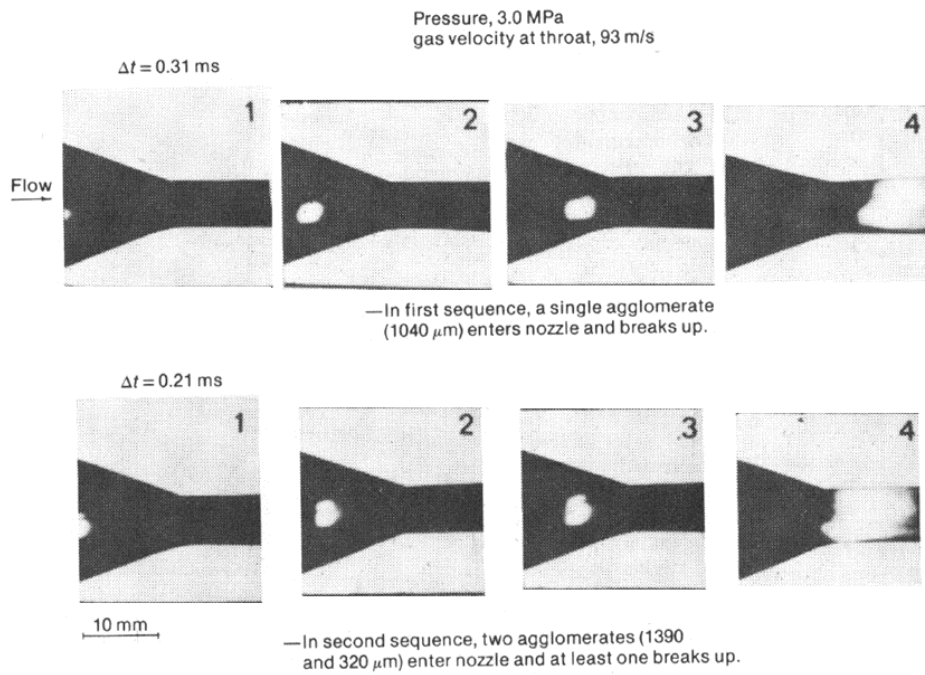
Figure 2-3 Agglomerates breaking up in nozzle [43]

2.5 Droplet Trajectory

Drag force is the driving force that accelerates the particle in carrier gas. The drag force is described by the following equation.

$$F_D = \frac{1}{2}\rho_g C_D A (V_g - V_p)^2 \tag{7}$$

Drag Force $F_D = 0.5\, \rho\ C_D A\, (V\text{-}V_P)^2$

Carrier Gas velocity (V)

Particle Frontal Area
$A = 0.25\ \pi\ D_P{}^2$

Diameter of the particle : D_P

Particle velocity V_P

Velocity difference
$\Delta V = (V\text{-}V_P)$
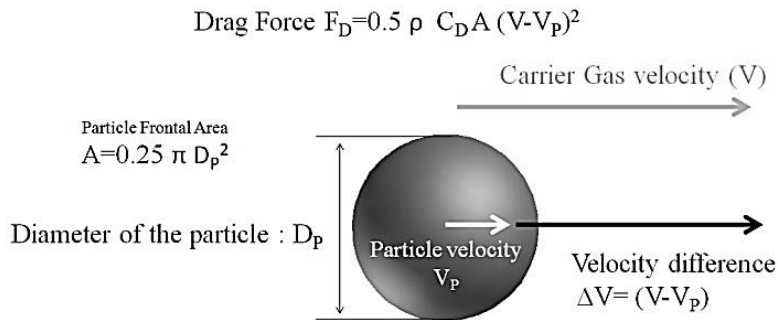
Figure 2-4 Particle acceleration driving force by carrier gas [13]

Where ρ_g is air density, C_D is drag coefficient, A is cross section area of droplet, V_g is the velocity of gas phase and V_P is the velocity of droplet particle. C_D is drag coefficient which a variable of Reynolds number [44], detailed function are described in appendix.

The calculation work the droplet trajectory in space shuttle SRM in terms of particle size is demonstrate in this paragraph, Figure 2-5 shows the cross section view of volume percentage of flow in combustion chamber with nozzle exit on the right hand side. The gas volume within nozzle throat radius contribute 37.5% of volume in the combustion chamber, all size of particle within this region will be able to escape without impinging on nozzle throat. This figure also shows the streamline of gas flow in combustion chamber, the streamline curvature becomes significant at out radius of combustion chamber when gas flow near the nozzle throat. For alumina particle outside escape zone will have chance to impinge on the throat, and the chance depends on the particle size. Larger particles has larger mass makes it less easy to follow streamline when moving in sever turning situation near nozzle, therefore smaller particle will have higher chance to escape in the outer diameter location of combustion chamber.
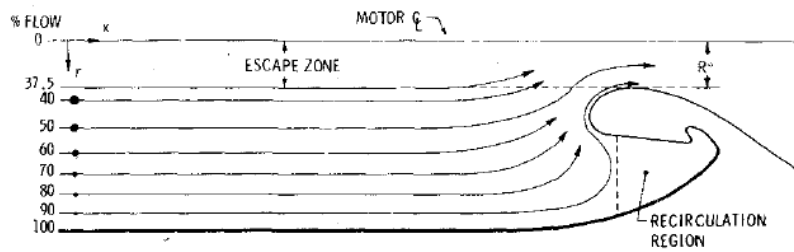
Figure 2-5 Relative size distribution of escaping droplets [21]

For the particle size which could escape to percent gas flow is shown in Figure 2-6. The burn time of space shuttle SRM is 127 sec, two different lines in this figure describe different burn time of space shuttle SRM of 97 sec and 120 sec which is at beginning and end stage of end burn of solid fuel. From the data of 97 sec, we could check that for particle diameter of 43 µm could escape from 90% of gas flow, but for larger alumina particle of 360 µm will be able to escape only from 60% of gas flow. Comparing same size particle at 120 sec of burn, alumina particle diameter of 43 µm could escape from 84% of gas flow and 360 µm will be able to escape only from 45% of gas flow, both 43 and 360 µm particle become less easy to escape through nozzle due to empty solid fuel in the pocket region of submerged nozzle make recirculation region has higher chance to trap alumina particles as demonstrated in Figure 2-2 (b).
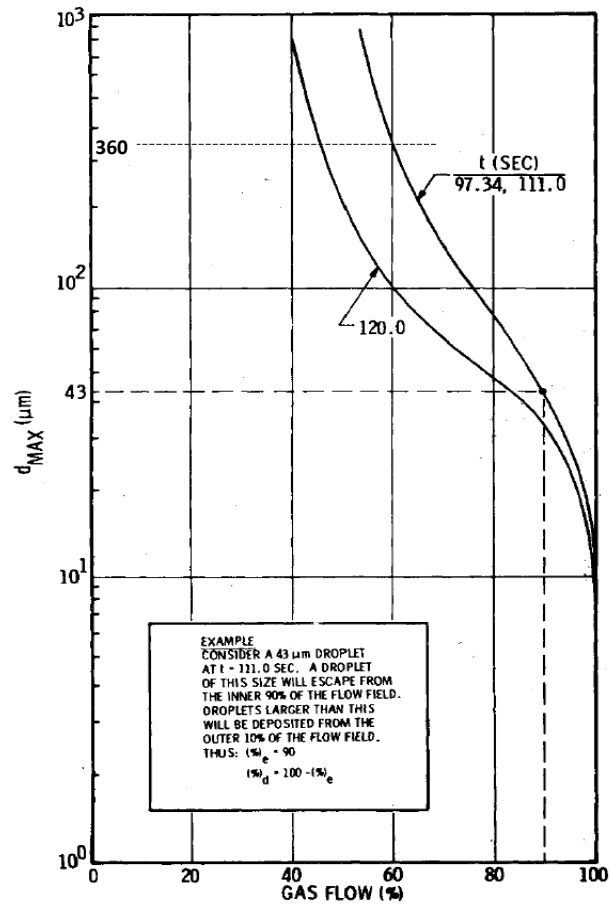
Figure 2-6 Maximum droplet size vs percent gas flow [21]

The one and two phase flow velocity distribution simulation of Jet Propulsion Laboratory (JPL) nozzle study [45] is shown in Figure 2-7. The nozzle simulation geometry used in this study is shown in part (a) with the simulated Mach number distributions along the nozzle wall and centerline shown in part (b), the velocity at wall varies more rapidly with x direction due to the gas need to follow the curvature of nozzle wall. The nozzle wall and centerline of two-phase nozzle flow gas-phase Mach number for various particle size with same particle/gas mass fraction of 30% are shown in figure (c) and (d), higher Mach number were observed for both wall and centerline flow field for gas only one-phase flow comparing with two-phase gas particle flow. Gas velocity

27

with larger particles is also faster than smaller particles. This is because smaller-sized particles are easier to accelerate by carrier gas due to higher area to mass ratio, which means it is easier for smaller particles to gain the kinetic energy transferred from gas-phase flow under same particle/gas mass fraction.
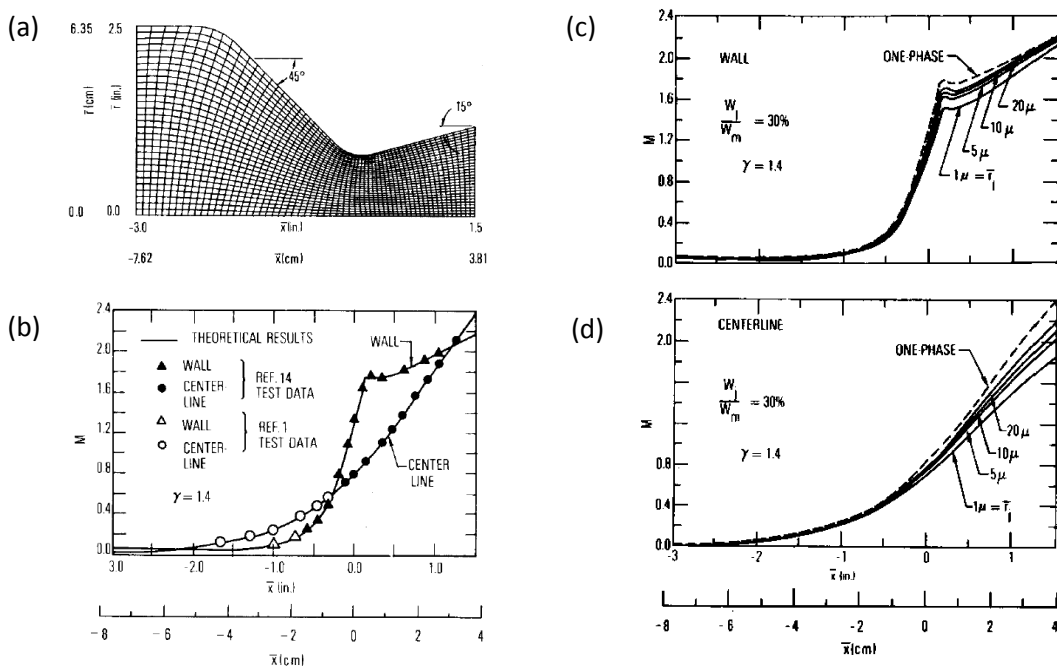
Figure 2-7 JPL nozzle (a) Mach number wall (b) Mach number centerline and particle density contour for particle size of (c) 1 μm and (d) 20 μm [45]

The study of particle trajectory path lines of different particle size is shown in Figure 2-8 [46], the particle size range from (a) to (d) are 1, 5, 10 and 20 μm respectively. The two-phase flow with 30% alumina particle mass fraction is simulated. It could be observed that the particle free zone is smaller for small sized particle than those of larger particles, as discussed in previous paragraph, smaller-sized particles are easier to follow flow stream of carrier gas due to higher area to mass ratio. On the other hand, larger particle also has higher chance to collide with nozzle wall as well.

28
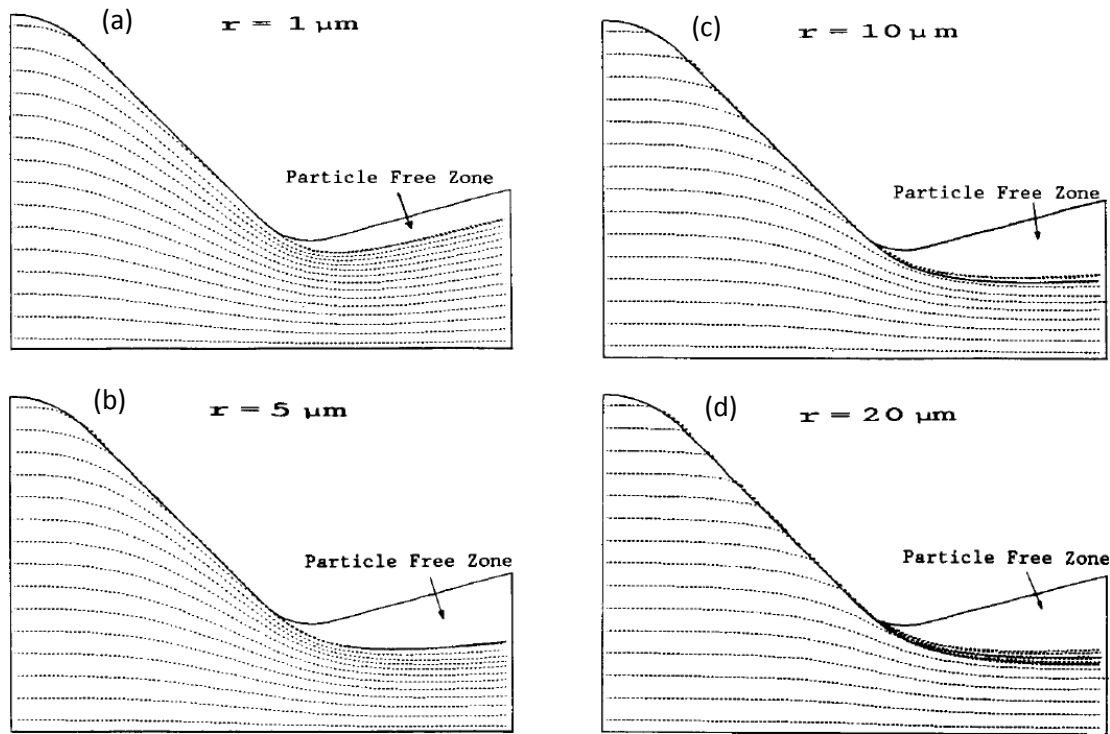
Figure 2-8 Trajectories for four different sizes particles [46]

Experiment work from Xiao and Amano [47] [48] contribute valuable real particle trajectory study. They apply X-ray Real time Radiography (RTR) technique to capture two-phase particle track in a solid rocket motor combustion chamber, their experiment sechmetic setup is shown in Figure 2-9 (a) , a thin tungsten (W) powder slot is bond with propellant for particle tracking, 3D view of the propellant and tungtan powder slot is shown in Figure 2-9 (b). The tungsten particle used in this study has average particle size of 75 µm with powder slot width of 0.5mm, experiemtn parameter detail are listed in Table 2-3.

Table 2-3 Tungsten particle RTR trace experiment parameters

Variables	Parameters
Combustion chamber	$200 \times 60 \times 50$ (± 0.1mm)
Propellant sample model	$150 \times 10 \times 50$ (± 0.1mm)
Tungsten powder Slot	0.5 ± 0.01mm
Tungsten powder	$\phi 75 \pm 1$ μm
Operation pressure	$6.75 \pm 0.25 \times 10^6$ Pa
Combustion temperature	2765 ± 10K

(a)

(b)

Figure 2-9 (a) Experiment setup and (b) Layout of propellant and tungsten powder [47]
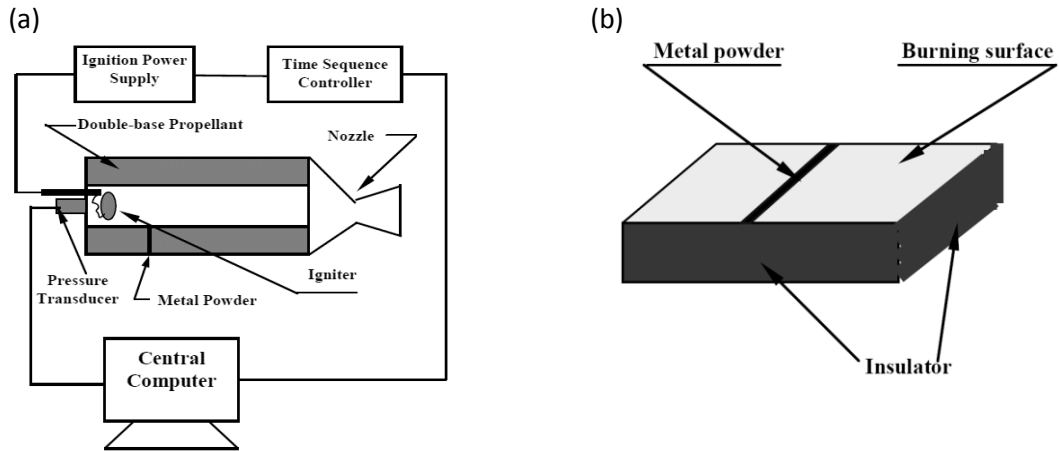
The X-ray image from Xiao and Amano's experiment are shown in Figure 2-10, it could be overserved that tungsten particle start leaving solid fuel surface and then following combustion gas moving toward nozzle exit.

30

t=0.408sec	t=0.412sec	t=0.416sec
t=0.420sec	t=0.424sec	t=0.428sec
t=0.432sec	t=0.436sec	t=0.440sec
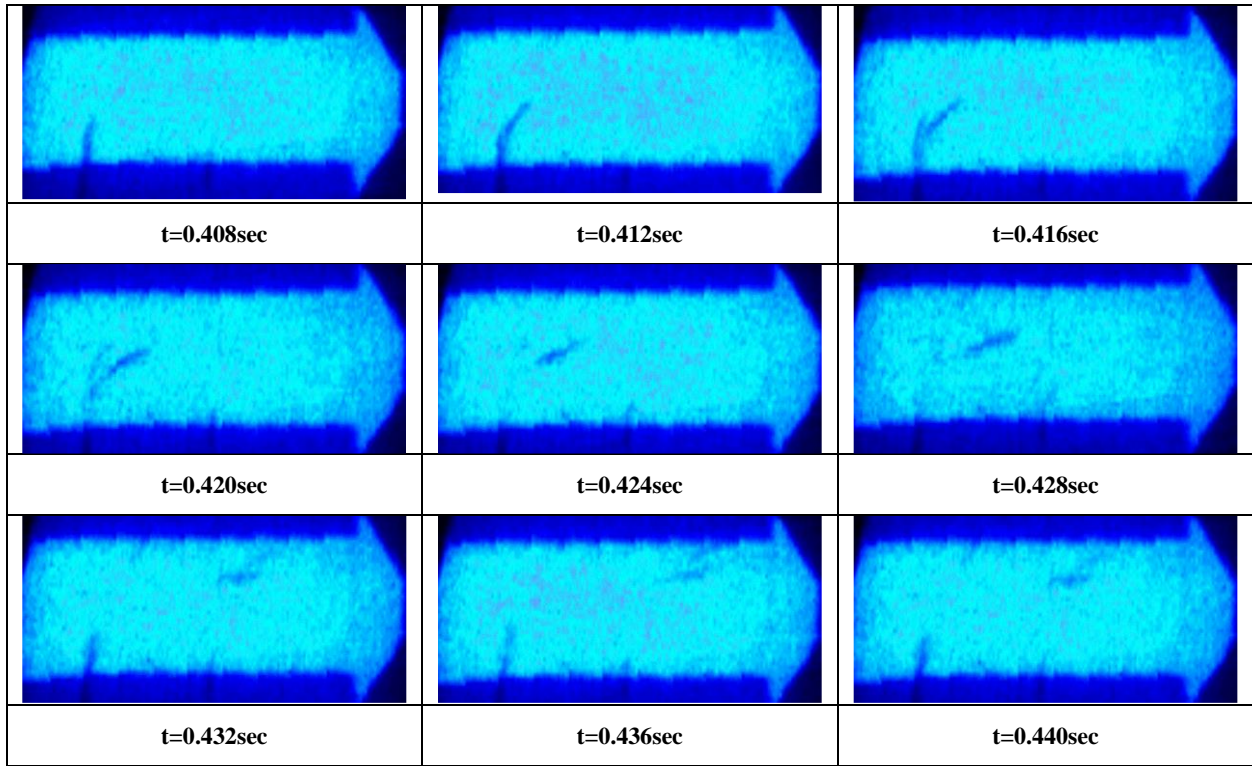
Figure 2-10 Combustion chamber RTR sequential image

In simulation work particle initial velocity should be defined, a variable α is used to describe the particle velocity as ratio of combustion gas velocity at solid fuel surface, α is defined as:

$$\alpha = \frac{V_P^0}{V_g|_{surface}}, \quad 0 \leq \alpha \leq 1 \tag{8}$$

Where $V_g|_{surface}$ is the gas velocity at solid fuel surface, V_P^0 is the particle initial velocity. Different α values from 0.0 to 1.0 with increment of 0.2 was simulated in order to compare with experiment, simulation trajectories result as shown in Figure 2-11 (a), as α increased a trajectory trend of leaving centerline was observed due to increasing particle Y directional momentum. In their work

the value of α=0.4 is suggested for particle initial velocity setup in simulation, a comparison of

trajectory from simulation with α=0.4 and experiment is shown in Figure 2-11(b)
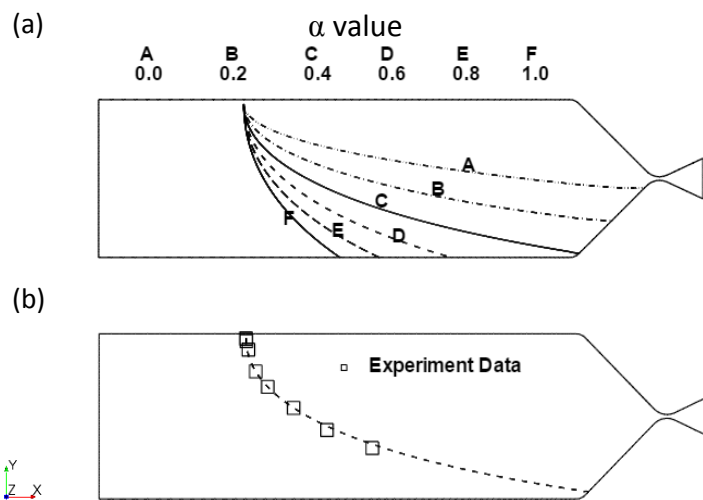
Figure 2-11 (a) simulation of 75µm tungsten particle trajectories with different α (b) comparison between simulation of α=0.4 and experiment

2.6   Solid Rocket Motor Nozzle Erosion

The de-Laval nozzle need to be able to withstand the severe environment of high pressure

difference, high temperature, high heat transfer and erosion. Nozzle are designed by segments as

shown in Figure 2-12 (a). Nozzle throat piece should be able to withstand tremendous heat and

erosion therefore a carbon fiber-reinforced carbon material is used in this section to provide

necessary performance due to its light weight and highly resistant to temperature up to 3400K

without losing structural integrity [49] [30]. Figure 2-12 (b) shows the operating temperature (° C)

and material lose by erosion (mm), the maximum material lose is 5.6mm in space shuttle solid

rocket booster. Compare to throat radius of 1879.6mm, the throat radius increase 0.29%. It is

proposed by increase the specific area of porous aluminum by 70% (10 to 18 m^2/g) the reduction of alumina slag agglomerated diameter decrease of approximately 65% [50] [51], however increase specific area of porous aluminum will increase the solid fuel burn rate and leads to propulsion control problems.
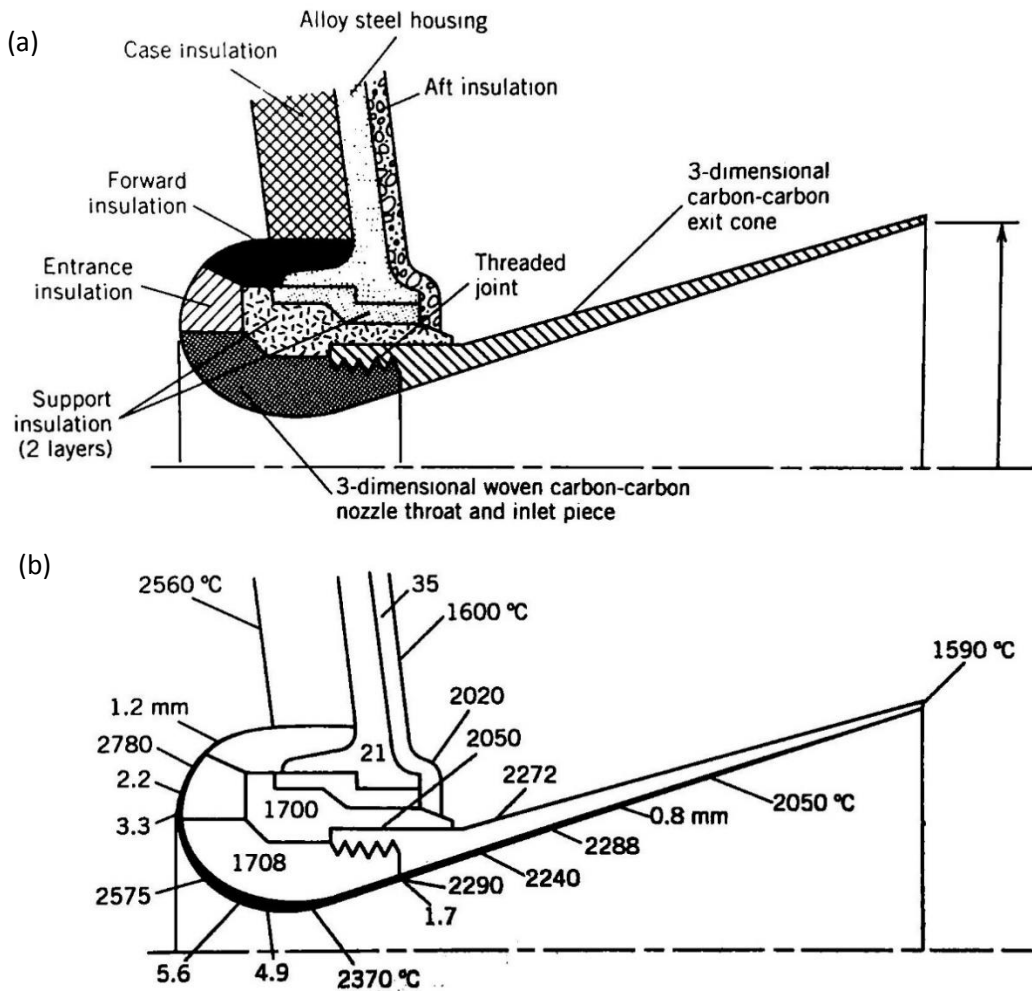
Figure 2-12 Components and temperature profile of a nozzle. The Shaded area in the lower picture indicate the amount of material lost by erosion. [30]

2.7 Liquid Breakup and Aluminum Surface Tension

The surface tension is an intrinsic property of all liquids which is due to an incomplete coordination of the liquid atoms or molecular at the liquid-gas free surface. Liquid breakup process is highly depend on the Weber number, the higher the Weber number is the higher chance for droplet to breakup, since surface tension is inverse proportional to Weber number, lower surface tension lead to higher Weber number and higher change for liquid breakup. Reducing liquid aluminum surface tension will enhance liquid alumina break up activity and reduce the solid rocket nozzle erosion phenomenon. The surface tension of pure liquid aluminum value raging between 1.05 to 1.09 N/m [52]. From the work of Anson et al. [53] they also compared the pure aluminum (99.9999%) surface tension with the aluminum alloy A356 (7.2% Si, 0.87% Mg) and modified A356 with strontium (st) added (7.5% Si, 0.79% Mg, 0.015% St), the surface tension result are 1.007, 0.889 and 0.844 N/m, respectively. this strontium and magnesium addition modified A356 aluminum alloy get significantly reduce the surface tension by 15 % under vacuum environment measurement, this is due to strontium itself has low surface tension of 0.29 N/m which is much lower value than other component in terms of surface tension. From Bainbridge et al [52] The reactive elements, magnesium, calcium, and strontium had the greatest eff ect in reducing the surface tension with the eff ects of other alloying elements being variable, ranging from negligible to substantial. Since magnesium are also solid fuel, it is highly possible use magnesium as a solid fuel additive to reduce the liquid alumina surface tension.

2.8 Computational Fluid Dynamics Approach

In fluid mechanics, the Navier-Stokes equation describe fluid motion by relating the density, velocity, pressure and temperature together and by balancing the equation we will be able to solve all fluid mechanics properties with associate location. Fully expand Navier-Stock equation are shown in equation (9) to (12).The equations were derived independently by French engineer Claude-Louis Navier and Ireland mathematician Sir George Stokes in the early 1800's. The Navier-Stokes equation could fully describe the fluid properties, however it is too complicated to get analytical solution. Nowadays the equation could only be solved in two dimensional case with many simplified assumption and the full analytical solution of Navier-Stoke equation is still unsolved yet.

In order to get solution from Navier-Stoke equation, numerical approach becomes a better option after the birth of computer technology. The numerical approach idea is by re-writing the governing equation of Navier-Stoke equation into numerical form, the complex numerical Navier-Stoke equation will become solvable by computer. The new fluid mechanics numerical approach study becomes a brand new field which is called Computational Fluid Dynamics (CFD). Since CFD fundamental was established in 1960s it caught attention for the researcher who work in fluid mechanics field and the concept of CFD proves the feasibility of utilizing computer and numerical method to help researchers solving one the most complex mathematical problem in the history numerically. The first CFD approach is Direct Numerical Solution (DNS) which solves the Navier-Stoke equation directly.

$$\frac{\partial \rho}{\partial t} + \frac{\partial(\rho u)}{\partial x} + \frac{\partial(\rho v)}{\partial y} + \frac{\partial(\rho w)}{\partial z} = 0 \tag{9}$$

$$\frac{\partial(\rho u)}{\partial t} + \frac{\partial(\rho uu)}{\partial x} + \frac{\partial(\rho uv)}{\partial y} + \frac{\partial(\rho uw)}{\partial z} = -\frac{\partial p}{\partial x} + \frac{1}{Re}\left[\frac{\partial \tau_{xx}}{\partial x} + \frac{\partial \tau_{xy}}{\partial y} + \frac{\partial \tau_{xz}}{\partial z}\right] \tag{10}$$

$$\frac{\partial(\rho v)}{\partial t} + \frac{\partial(\rho uv)}{\partial x} + \frac{\partial(\rho vv)}{\partial y} + \frac{\partial(\rho vw)}{\partial z} = -\frac{\partial p}{\partial y} + \frac{1}{Re}\left[\frac{\partial \tau_{xy}}{\partial x} + \frac{\partial \tau_{yy}}{\partial y} + \frac{\partial \tau_{yz}}{\partial z}\right] \tag{11}$$

$$\frac{\partial(\rho w)}{\partial t} + \frac{\partial(\rho uw)}{\partial x} + \frac{\partial(\rho vw)}{\partial y} + \frac{\partial(\rho ww)}{\partial z} = -\frac{\partial p}{\partial z} + \frac{1}{Re}\left[\frac{\partial \tau_{xz}}{\partial x} + \frac{\partial \tau_{yz}}{\partial y} + \frac{\partial \tau_{zz}}{\partial z}\right] \tag{12}$$

Although CFD provide a new approach for fluid mechanics researchers, it has the problem of computational intensive character. CFD is a numerical tool and the accuracy of numerical approach is depend on spatial and time resolution. The finer we could treat on the increment of spatial and time in the simulation the more accurate solution will be. The computational time required to a simulation is directly proportional to the number of cell and total time step in simulation which make accurate solution become computational expensive. Researcher start to think using different method other than DNS to reduce the amount computational cell required. Therefore Large Eddie Simulation (LES) and Reynolds Averaged Navier-Stoke (RANS) approach were introduced. In terms of computational expensive raking from high to low are DNS, LES and RANS respectively. RANS applies turbulence model to predict the flow instead of solving it and resulting in much faster time required to solve a simulation problem. About the accuracy, solutions of RANS approach is not always compatible with experiment data, but it could show some good trend which make sense to researchers. Due to this, RANS CFD approach

36

is still popular nowadays in most of industry research work. LES on the other hand, unlike DNS to solve all scale turbulence LES apply coarser mesh than DNS which is just enough to solve large scale turbulence or eddies and use subgrid scale (SGS) model to solve small eddies. This approach also make it a faster approach than DNS and since large scale eddies are solved instead of using turbulence model in RANS, LES could provide much accurate result compare to RANS. In terms of computational time, the mesh resolution requirement of LES is still higher than RANS, therefor LES is still a computational expensive approach today and only large research institute will consider using LES approach.

Since the computer technology is rapid growth in the last few decades. LES approach start to catch attention from year of 2000s. An extensive LES simulation research work of two-phase bluff body recirculating flows done by Riber, Eleonore, et al. [54]   All of their work are compared with bluff body experimental data done by Boree, et al. [55] From their LES research conclusion, the mesh type of tetrahedral and hexahedra does not affect the final result. From their recommendation, using high-order schemes built for LES provides better result compare to lower-order schemes. The most critical part of LES is the ability to predict two-phase flow, even though the accuracy of the LES is still high in most of the flow.

2.9 Summary

Aluminum is widely used metallic solid fuel with characters of high performance, economic and less toxic to organism and less environment impact. The combustion of aluminum with ammonium perchlorate (AP) produce alumina (Al_2O_3) which is liquid status with size ranging from 1 to 500 μm in combustion chamber and tend to agglomerate and from alumina slag, during those slag and alumina particles impinge on the nozzle throat wall lead to erosion and remove material on the inner wall of nozzle. The erosion process changes the geometry of nozzle especially the nozzle throat and the nozzle performance decreases due to increasing nozzle throat diameter or decrease the exit/throat area ratio. Once throat/exit area ratio decrease, the optimized nozzle geometry start to deform and the exhaust gas velocity decreased which affect rocket performance.

Smaller-sized particles are easier to follow flow stream of carrier gas due to higher projection area to mass ratio, smaller particle will have more chance to avoid impinging on the nozzle wall during rapid direction changing curvature of flow stream near the nozzle entrance, therefor reduce average alumina particle size will be a potential approach to reduce erosion problem of SRM and further improve the performance and burn time. The agglomerate particle size inside combustion chamber is highly dominate by combustion chamber pressure, it is confirmed that higher the pressure reduce the agglomerate particle size. However the means of increase the chamber pressure in order to reduce agglomerate particle size will be limited due fuel burn rate, thrust control. The rocket structure will need to take into concern at the same time for target operation chamber pressure modification. It is possible to reduce alumina surface tension by change the compound of solid fuel. From study, the modified aluminum alloy of A356 with strontium (st) added (7.5% Si, 0.79%

Mg, 0.015% St) has the surface tension value of are 0.844 N/m. This strontium and magnesium addition in the modified A356 aluminum alloy results in 15 % reduction on the surface tension.

About computational simulation tool, a variable α is used to describe the particle velocity as ratio of combustion gas velocity at solid fuel surface, from the research work done by Xiao and Amano, the α value is equal to 0.4 which is an important reference value for gas-particle rocket combustion chamber simulation setup. The CFD approach method plays an important role as well. Three major CFD approach group are available nowadays. They are RANS, LES and DNS respectively, the order of the list followed by the computational intensity from low to high. Detached Eddy Simulation (DES) is a new approach which is an inherent RANS model coupled with LES approach. Therefor DES approach sits between RANS and LES.

From literature, LES has better potential to predict the flow than different RANS turbulence models group and DES group. DNS is the best approach, however it is not an option for this study due to limited computational resource in campus.

3   Liquid Breakup Study Methodology

In this study, an unsteady two-phase air-water flow experiment and CFD simulation were carried out. Liquid breakup phenomenon is investigated by analyzing images from straight channel experiment and computational simulation with different gas-liquid flow conditions. Two flow variables are the main interest of this liquid breakup study which is the air velocity and the liquid surface tension setup. The study results provide a better understanding of the liquid breakup phenomenon. The results of this study will be able to propose and apply to Solid Rocket Motor (SRM) industry for better anti-erosion solutions.

3.1   Study Approach Limitation

Before jump into the liquid breakup study, we need to understand the challenges and research limitation of the study in order to complete this study with proper and efficient approach. Our plan of the study approaches are from both experiment and simulation. The challenges from experiment are time and space resolution. Breakup could happen in a short period of time, and also the liquid breakup droplet will be small in size. The performance of camera on space resolution limits the smallest droplet could be captured during breakup, any droplet smaller than a pixel of Charge-Coupled Device (CCD), a digital optical device with work as function of film, will not be able to capture to image. Time resolution or frame speed limits any behavior has frequency higher than camera capture speed as well.

Computational Fluid Dynamic (CFD) is a powerful alternative tool for researcher to study fluid behavior except experiment in fluid mechanics practices. Most CFD engineering software are

advance nowadays, however, some simulation challenges still need take into concern, they are CFD approaches and mesh size selection. The proper selection of CFD approach is required due to highly turbulent two phase flow characters, the right selection help ensure the accuracy of the simulation. In our study, Large Eddy Simulation (LES) will be chose as CFD approach due to high accuracy for complex flow field. The simulation mesh density setup direct affect the simulation accuracy, simulation time required, and the liquid breakup droplet display. Since the range of droplet scale ranges from mm to μm, the proper selection of mesh size should be studied in order to reach optimized CFD performance between accuracy of liquid breakup droplet prediction and the computational time required.

3.2 Error Analysis

One of the limitation of this study is from error in experiment and simulation. The error in experiment is depend on the camera resolution and the error in simulation is depend on the grid resolution. The high speed camera has 1280 pixel along horizontal direction in experiment and capturing 307 mm field which leads to the conversion of each pixel equal to 0.24mm. Therefor the value in experiment is ± 0.24mm.

In the simulation, our final mesh setup is 16 million cell mesh, the mesh is evenly distributed in the fluid domain of 1000mm (length) × 200mm (height) × 25mm (width). The mesh size is roughly equal to 0.67mm in simulation. Therefor the error in simulation is ±0.67mm.

The simulation has larger error while compare to the value from experiment. The resolution of simulation grid is limited by the computational power of HPC resource. It is worth to increase the

simulation grid resolution and share same error with images from experiment in the future when computation resources is enough to handle higher mesh resolution.

3.3   Two-Phase Flow Channel Geometric Configuration

Two-phase flow experiment was conducted in a rectangular channel in this study, as shown in Figure 3-1(a). The dimension of the channel has a 170 mm air inlet at upper side of entrance and a 30 mm of liquid inlet through the lower side of inlet section. A ramp with a height of 15 mm and an angle of 20 degrees is placed at a location 0.159 m from the inlet that is used to create a flow separation of liquid. The total length of the channel is 1 m. The inlet velocity of the liquid is maintained constant at 0.67m/s with air inlet velocity setting of 20m/s, 30m/s, and 40m/s respectively. The system schematic is shown in Figure 3-1(b), four major components compose the system are air pump, water pump, test channel and reservoir. The performance capability of air and water pumps is 45m/s and 3.5 m/s, respectively.

Table 3-1 Properties of Liquids [56] [57]

	Density (kg/m3)	Viscosity (Pa-s)	Surface Tension (N/m)	Meting Point (K)	Vaporization Point (K)
Alumina2,500K	3,950	4.60E-02	0.67	2,026	3,250
Water	998	8.90E-04	0.074	273	373
Air	1.225	1.80E-05	NA	NA	NA

(a)

1m

0.2m Air →

Water →

0.159m

0.8m

Ramp detail

0.015m

20°

(b)

Test Channel

Air Pump

Water Pump

Reservoir
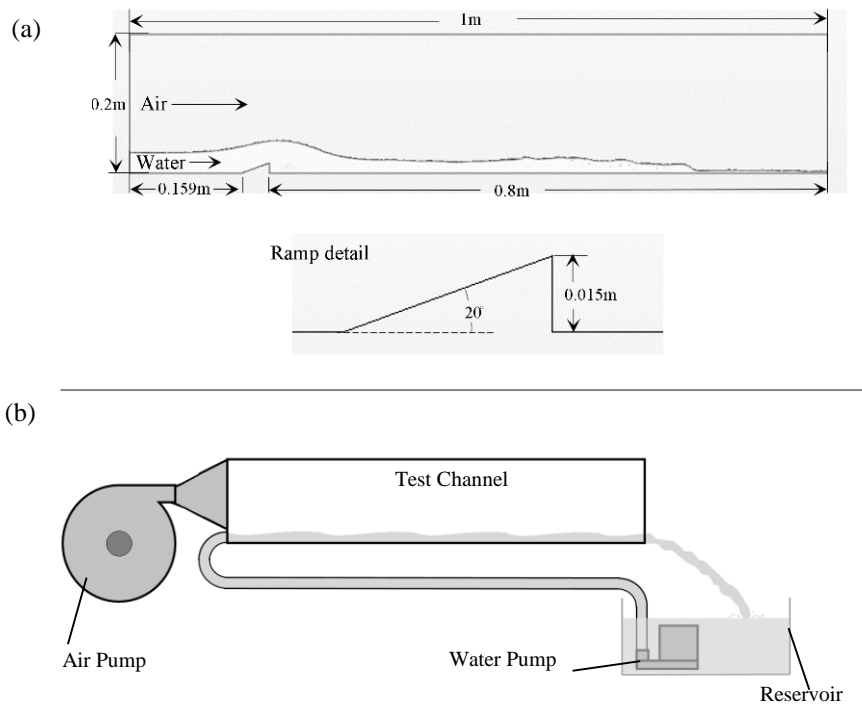
Figure 3-1 (a) Flow geometry of experiment two-phase flow channel (b) Experiment system schematic

3.4 Research Equipment and Facility

The study approaches are experiment and simulation; in this chapter we will discusses equipment and facility to accomplish the study. The high speed camera is necessary equipment for the research of liquid breakup study due to the micro second activation time of liquid breakup phenomenon; High Performance Computing (HPC) is also required for simulation since the two phase flow simulating is a computational intensive application. Detailed specification of the research equipment and facility will be discussed in this chapter.

3.4.1 High Speed Camera

The high speed camera we use is a Photron Fastcam Mini UX50. There are three major parameter, frame rate, resolution and record duration. Those parameter need to take into concern during filming. The frame rate of camera is expressed in frame per second (fps) which is an indicator of how fast the camera taking pictures. The maximum resolution of this camera is 1280×1024, however the resolution is varies with frame rate. Higher frame rate reduce the image resolution. The fastest frame rate for full resolution is 2,000 fps, for frame rate faster than 2,000 fps, image resolution will be sacrificed. Since there is significant amount of image information be capture during a short period of time, the record duration will be limited by the capacity of onboard memory for each trigger. In our experiment we will choose the frame rate of 1,000 fps for best resolution and longer record duration. The specification of this camera is listed in Table 3-2.

Table 3-2 Photron Fastcam Mini UX50 Specifications

Frame Rate (fps)	Horizontal	Vertical	Record Duration (sec)	Frames
1000	1280	1024	2.18	2180
2000	1280	1024	1.09	2180
4000	1280	512	1.09	4361
5000	1280	488	0.92	4575
8000	1280	296	0.94	7543
10000	640	240	1.86	18607
20000	1280	120	0.93	18607
40000	1280	56	1.00	39872
80000	1280	48	0.58	46518
100000	1280	24	0.93	93036
160000	1280	8	1.74	279108

3.4.2 High Performance Computing

The High Performance Computing (HPC) center of University of Wisconsin Milwaukee provide a powerful computing environment for numerical computing applications, there are three independent HPC system named Avi, Mortimer and Peregrine for researcher to run their jobs. Our liquid breakup studies are carried out in Avi and Mortimer system; the specifications of three UWM HPC systems are listed in Table 3-3.

Table 3-3 HPC system specification of Avi [58]

Specifications	Avi	Mortimer	Peregrine
Compute Nodes	142	104	8
Number of Cores	1136	1924	96
CPU	Xeon X5550	Xeon E5-2450 v2	Opteron 4180
Processor Frequency	2.67 GHz	2.5 GHz	2.6 GHz
Memory	24GB/Node	48GB/Node	16GB/Node
Constructing Cost ($)	850,000	800,000	N/A
Construction year	2009	2015	2010

3.5 Image Processing

The imagine process code in this study is achieved on the software platform of MatLab. All of the MatLab codes are developed in UW-Milwaukee wind tunnel lab. The imaging process codes are tools helping us to quantify the two-phase flow in this research. The image process code include particle size information extraction tool, Welch's frequency analyze tool and time average superimpose process tool. More detail of those image process tools will discuss in the following paragraph.

3.5.1 Imaging Processing for Particle Size Information

The original MatLab code for particle information is documented in chapter 0. A test image shown in Figure 3-2 is used to demonstrate the capability of image process code. There are 10 objects in this image, each object are round in shape with different size in diameter range from 10 to 100 pixels.

Figure 3-2 Test image with 10 different size from 10 to 100 pixels with increment of 10 pixel

Since pixel information in computer science is square in shape as demonstrated in Figure 3-3 (a)Figure 3-2, MatLab code use an approximation equation to describe the diameter of the object size expressed in pixel as defined in the following:

$$D\ (Pixel) = \sqrt{\frac{4\ A(Pixel)}{\pi}} \tag{13}$$
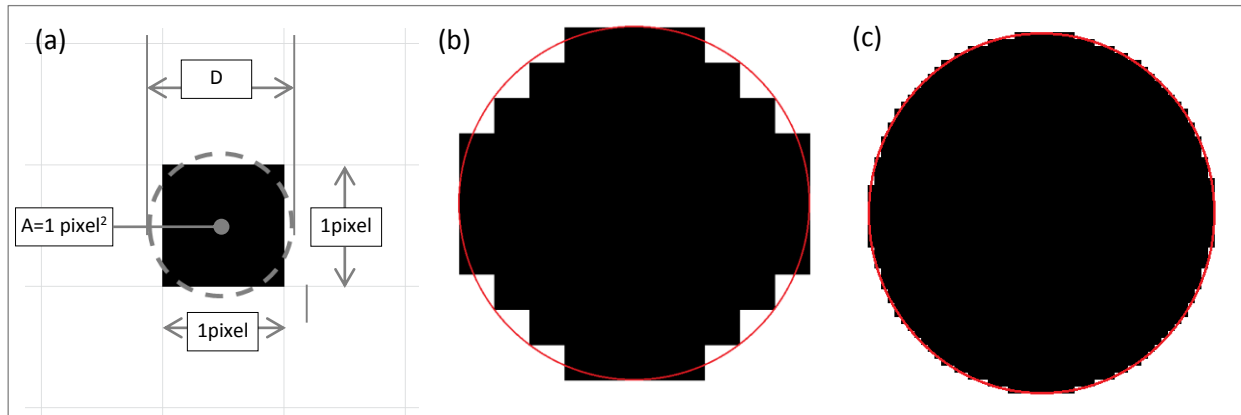
Figure 3-3 (a) Demonstration of pixel and round shape (b) 10 pixel round shape error (c) 50 pixel round shape error

The result of the image process analyses tool on the test image of Figure 3-2 is shown in Table 3-4. Due to the limitation of squared pixel to describe perfect round geometry, there will be error between image size and the extracted information. The error will start to decrease when the particle size becomes larger as shown in Figure 3-3 (b) and (c)

Table 3-4 Image process result of Figure 3-2

Image diameter (pxl)	10	20	30	40	50	60	70	80	90	100
Area (pxl)	76	308	692	1246	1942	2802	3822	4992	6328	7830
Diameter (pxl)	9.837	19.803	29.683	39.830	49.726	59.730	69.759	79.725	89.761	99.847
Error %	1.63	0.99	1.06	0.42	0.55	0.45	0.34	0.34	0.27	0.15

3.5.2 Imaging Processing for Particle Size Workflow

Since the study involve with lots of images from either experiment high speed camera or high performance cluster computing simulation output. An automation tool for image post processing become necessary. The MatLab image process workflow used in this study will be discussed in this paragraph. The image process code work flow is shown in Figure 3-4. The workflow section numbering is a reference on the section of code. It start from entry section and then section 20 of image input part which helps user to select target image folder from either experiment images or simulation output. Section 30 and 40 are retrieve the variable of total number of images (n) and define the eccentricity target filter. The purpose of eccentricity filter number is to filter out the particle information with eccentricity over the target value. The main program starts from section 50 which is the loop section, during the loop section, it will go through all of the subsection inside the loop section until the loop stops, loop start from i=1 to total image number (n) in the target folder. Section 60 read image number (i) in the folder. Section 70 is important section which find all particles inside image (i) and calculate the particle information of size, eccentricity and boundary. Section 80 is eccentricity filter for image (i), for any particle information has eccentricity larger then eccentricity filter will be erased. The reason is to remove the data with highly skews particles which might result of light intensity difference noise or deforming water bodies. Section 90 store the processed particle information for image (i), and section 100 checks if (i) < (n), if yes, assign i = i +1 and go to section 50. If no, the loop will be end and go to section 110 which save all final data and finish the workflow.

Section numbering

10	**Entry**
20	Input of image folder
30	Calculate total image number: n
40	Set eccentricity Target filter
50	Loop: For i =1 to n
60	Read image(i)
70	Process image droplet info (i): [size, eccentricity, boundary]
80	Check<Eccentricity
90	Save image droplet info (i): [size, eccentricity, boundary]
100	Check loop: i<n Yes No
110	Save all droplet info (1 to n): [size, eccentricity, boundary]

i= i +1
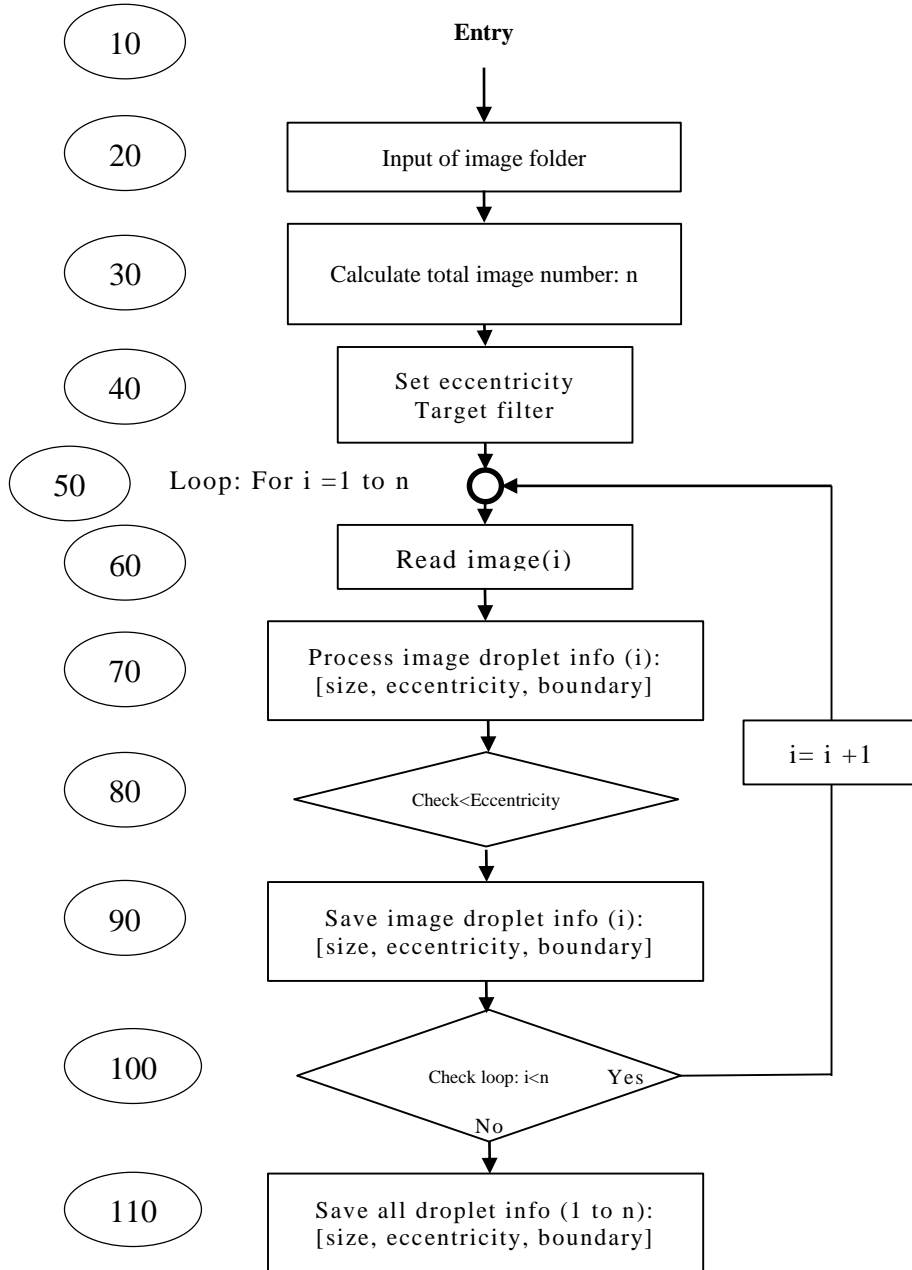
Figure 3-4 MatLab image process workflow

49

3.5.3 Fast Fourier Transform and Welch's Method

The Fast Fourier Transform (FFT) and Welch's method is another quantification method used for the air-water two phase free surface frequency analysis. This method convert the wave location history from time domain to frequency domain. The purpose of frequency analysis is used for major frequency comparison for different flow case. The frequency history from free water surface is extract by MatLab code documented in appendix.

3.5.4 Image Superimpose Process

Two-phase turbulent flows behave highly irregular and it is hard to capture a certain repeatable flow pattern. Figure 3-5 illustrates the simulation results with the same boundary condition and the numerical model setting over a period of different time step, the simulation condition detail as shown in Table 3-5. The breakup droplet size might be similar in their size, however the similarity character is difficult to determine from those three figures even though the operating conditions are the same. Therefore, a method of figure superposition is introduced in this paper in order to visualize time averaged contour through results of all time steps.
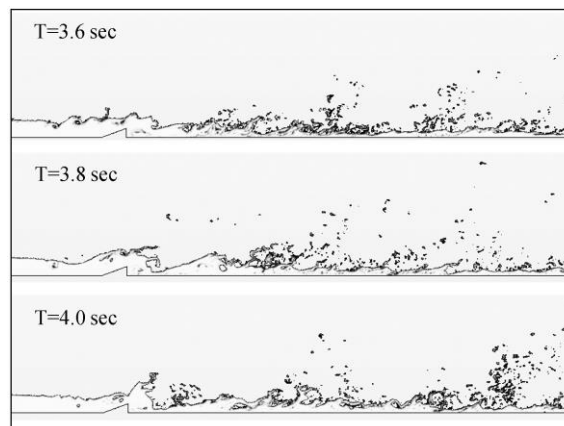
Figure 3-5 VF of fluid boundary at different time step

50

In this demo three pictures with black and white pixels with pixel lables of 0 and 1 are shown in

Figure 3-6, where pixel value 0 represent pure black and pixel value 1 represent pure white color,

the illustration of the gray scale map from coresponding pixel lable value are shown in Table 3-5.

The pixel supersotition is shown in Figure 3-6. After superimposition of Figure 3-6 from (a) to (c),

the pixels' averaged values are calculated and the results in a gray scale map is shown in Figure

3-6 (d).

Table 3-5 Gray scale color map

Pixel label value	Gray scale color map
0.00	
0.33	
0.50	
0.67	
1.00	

	0	1	0	1
(a) demo 1				
	1	0	1	0
	0	1	0	1
(b) demo 2				
	0	0	1	1
	0	1	1	1
(c) demo 3				
	1	0	1	1
	0	1	0.333	1
(d) superposition of all 3 demo figure				
	0.667	0	1	0.667

Figure 3-6 Demo of pixel superposition

51

Figure 3-7 is the demonstration of image after superimposes processing of 1,000 frames from one of the experiment case. After superimpose the gray scale map could be interpreted as free surface probability distribution. The super imposed image will be used for crest and trough position analyzing.
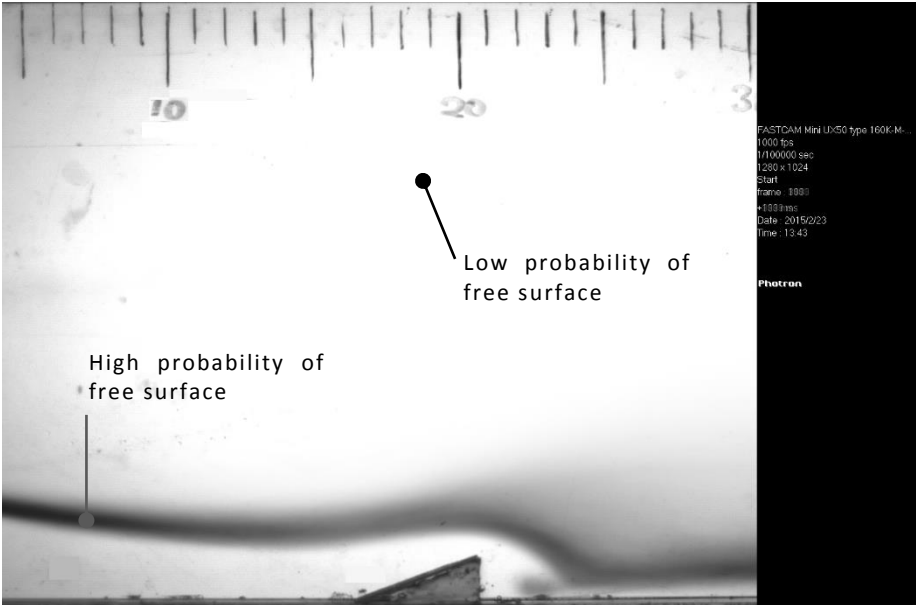
Figure 3-7 Image after super impose processing of 1,000 frames

4 Computational Methodology

Computational fluid dynamics (CFD) are developed in 1930s which applies numerical method to express the governing equation of fluid mechanics and run by computer code. Through decades of CFD development and progressive growth of information technology, CFD becomes a powerful but affordable research tool for academic and industry. The advantages of CFD is readiness for geometry setup and easiness to change variables or properties of working fluid in relative short period of time and also significant amount cost reduction compare to experiment. The disadvantages of CFD is the balance between the prediction accuracy and computational time. In order to reach accurate CFD result, finer mesh setup will be required. The required mesh size varies from case to case. In some cases CFD prediction accuracy could be achieved for the mesh size at the order of 100 thousand cell to 10 million cell. Some case will require the mesh with total cell number up to scale of 100 million to 10 billion. The computer process time required will proportional the total size of mesh. For complex CFD cases it will be computational intensive and expensive in order to get accurate result.

For this study all of the CFD simulation were carried out by CD-Adapco STAR-CCM+® which is a popular commercial software widely used in academic, aerospace, automobile, and energy industry. The CFD software work in this study is to perform a two-phase flow simulation and we would like to investigate to what extent CFD could predict in terms of flow behavior and breakup phenomenon while compared the CFD result with experiment work. In this chapter we will discuss mesh generation procedures, three different CFD approaches of Direct Numerical Simulation

(DNS), Large Eddie Simulation (LES) and Reynolds Average Navier-Stock (RANS), and also the multiphase simulation method of Volume of Fluid (VOF).

4.1 Computational Fluid Dynamics (CFD) Approaches Introduction

There are three particular approach of CFD, they are Direct Numerical Simulation (DNS), Large Eddy Simulation (LES) and Reynolds-Averaged Navier-Stokes (RANS). A detailed table are listed below.

- Direct Numerical Simulation (DNS)
    - It is technically possible to resolve every fluctuating motion in the flow.
    - The space resolution and time step increment must be very fine.
    - DNS approach is still restricted to supercomputer applications.
- Large Eddy Simulation (LES)
    - Computational demands of SRS sit between DNS and RANS
    - Only larger eddies are resolved
    - The time steps mesh space resolution are larger than DNS
- Reynolds-Averaged Navier-Stokes (RANS)
    - Still the main stream for academic and industry application
    - Equations are solved for time averaged flow and turbulent are modeled.

The CFD software used in this simulation study is CD-Adapco STAR-CCM+ which is widely used in academic and industry; this software was used to predict the flows and to solve the unsteady Reynolds-Averaged Navier-Stokes (URANS) equations and Large Eddie Simulation (LES). The

system of equations was solved in an Eulerian multi-phase state with an implicit unsteady solver applying the volume of fluid (VOF) approach for the interface between the liquid and gaseous phases which was published by Hirt and Nichols in 1981 and wildly applied in academic and industries nowadays [59]. The model detail are listed in the following sub-chapters.

4.2 Reynolds-Averaged Navier Stoke (RANS) Equation

The numerical simulations were carried out by integrating the unsteady Reynolds-averaged Navier-Stokes (RANS) equations. The averaged mass, momentum and the energy equations can be written in a conservative form as shown in the following equations.

Mass conservation equation

$$\frac{\partial \rho}{\partial t} + \frac{\partial \rho U_i}{\partial X_i} = 0 \tag{14}$$

Where ρ is the density of fluid and U_i is the velocity component in ith direction.

Momentum conservation equation

$$\frac{\partial \rho U_i}{\partial t} + \frac{\partial (\rho U_i U_j)}{\partial X_j} = -\frac{\partial P}{\partial X_i} + \frac{\partial (\tau_{ij} - \rho \overline{u_i u_j})}{\partial X_j} \tag{15}$$

$$\tau_{ij} = \mu \left(\frac{\partial U_i}{\partial X_j} + \frac{\partial U_j}{\partial X_i} - \frac{2}{3} \frac{\partial U_k}{\partial X_k} \delta_{ij} \right) \tag{16}$$

Where P is the pressure of fluid, τ_{ij} is the viscous stress with detailed expression next to momentum

conservation equation, u_i and u_j are the fluctuating velocity components in ith and jth directions

respectively and μ is the fluid dynamic viscosity. $-\rho \overline{u_i u_j}$ is the Reynolds stresses term which

represent the effect of turbulence. From Boussinesq approximation the Reynolds stresses could be

expressed as follows:

$$-\rho \overline{u_i u_j} = \mu_t \left(\frac{\partial U_i}{\partial X_j} + \frac{\partial U_j}{\partial X_i} \right) - \frac{2}{3} \left(\rho k + \mu_t \frac{\partial U_k}{\partial X_k} \right) \delta_{ij} \tag{17}$$

Energy conservation equation

$$\frac{\partial \rho E}{\partial t} + \frac{\partial (\rho E U_i + P U_i)}{\partial X_i} = -\frac{\partial}{\partial X_i} (q_i + C_p \rho \overline{u_i t'}) + \frac{\partial}{\partial X_i} (\tau_{ij} U_j - \rho \overline{u_i u_j} \, U_j) \tag{18}$$

Where E is the total energy, Cp is the specific heat at constant pressure, and t' is the fluctuating

component of temperature. Heat flux q_i is expressed as follows

$$q_i = K \frac{\partial T}{\partial X_i} \qquad (19)$$

Where K is the thermal conductivity of fluid, and turbulent heat flux $\rho \overline{u_i t'}$ is expressed as follows

$$\rho \overline{u_i t'} = \frac{\mu_t}{Pr_t} \frac{\partial T}{\partial X_i} \qquad (20)$$

Where Pr_t is the turbulent Prandtl number.

4.3 Reynolds Stress Model (RSM)

To close the Reynolds-averaged Navier-Stokes (RANS) equation the Reynolds stress model (RSM) was applied to part of the simulation. The Reynolds stresses $\rho \overline{u_i' u_j'}$, can be expressed as the following [60].

$$\frac{\partial}{\partial t} (\rho \overline{u_i' u_j'}) + \frac{\partial}{\partial x_k} (\rho \, u_k \overline{u_i' u_j'}) = -\frac{\partial}{\partial x_k} [\rho \overline{u_i' u_j' u_k'} + \overline{p(\delta_{kj} u_i' + \delta_{ik} u_j')}]$$

$$(21)$$

$$+ \frac{\partial}{\partial x_k} [\mu \frac{\partial}{\partial x_k} (\overline{u_i' u_j'})] - \rho (\overline{u_i' u_k'} \frac{\partial u_j}{\partial x_k} + \overline{u_j' u_k'} \frac{\partial u_i}{\partial x_k}) - \rho \, \beta (g_i \overline{u_j' \theta} + g_j \overline{u_i' \theta})$$

57

$$+P\overline{\left(\frac{\partial u_i'}{\partial x_j} + \frac{\partial u_j'}{\partial x_i}\right)} - 2\mu\overline{\frac{\partial u_i'}{\partial x_k}\frac{\partial u_j'}{\partial x_k}} - 2\,\rho\,\Omega_k(\overline{u_j'u_m'}\epsilon_{ikm} + \overline{u_i'u_m'}\epsilon_{jkm})$$

In equation (21) , the first term $\frac{\partial}{\partial t}(\rho\overline{u_i'u_j'})$ is the local time derivative term with ρ as the density

and $\bar{u}'$ as the time averaged fluctuating velocity component; the second term $\frac{\partial}{\partial x_k}(\,\rho\,\mathrm{u}_k\overline{u_i'u_j'})$ is the

convection term; the third term $\frac{\partial}{\partial x_k}[\rho\overline{u_i'u_j'u_k'} + \overline{p(\delta_{kj}u_i' + \delta_{ik}u_j')}]$ is the turbulent diffusion term;

the fourth term $\frac{\partial}{\partial x_k}[\mu\frac{\partial}{\partial x_k}(\overline{u_i'u_j'})]$ is the molecular diffusion term with μ as the viscosity of fluid;

the fifth term $\rho(\overline{u_i'u_k'}\frac{\partial u_j}{\partial x_k} + \overline{u_j'u_k'}\frac{\partial u_i}{\partial x_k})$ is the stress production term; the sixth term $\rho\,\beta\,(g_i\overline{u_j'\theta} + $

$g_j\overline{u_i'\theta})$ is the buoyancy term with β as the thermal expansion coefficient, g as the acceleration

direction and θ as the temperature; the seventh term $P\overline{\left(\frac{\partial u_i'}{\partial x_j} + \frac{\partial u_j'}{\partial x_i}\right)}$ is the pressure strain term; the

eighth term $2\mu\overline{\frac{\partial u_i'}{\partial x_k}\frac{\partial u_j'}{\partial x_k}}$ is the dissipation term; and the ninth term $2\,\rho\,\Omega_k(\overline{u_j'u_m'}\epsilon_{ikm} + \overline{u_i'u_m'}\epsilon_{jkm})$

is the production by system rotation term with Ω as angular velocity.

4.4   Detached Eddy Simulation (DES)

Detached eddy simulation (DES) is a modification of Reynolds-Averaged Navier-Stock (RANS)

model with judgment criteria to enable Large Eddy Simulation (LES) method where the mesh is

fine enough. The Unsteady RANS are capable to solve transient fluid motion like time dependent

flow pattern, vortex shedding and unsteady flow separation behavior. However the limitation of

the RANS turbulence model may not be able to fully simulate turbulence due to time average character. LES on the other hand use subgrid scale filter which filter out small eddy and simulate large eddy direct only. This approach provides a great balance between computational resource and turbulence resolution. However LES method has week point particularly in simulating near-wall boundary layer regions. DES method therefor combine advantages of both RANS and LES approach which solve boundary layers and irrational flow regions by applying RANSE closure model. If the mesh grid is fine enough, DES will apply a basic LES subgrid scale model in detached flow regions.

There are two options of DES, they are SST K-Omega DES and Spalart-Allmaras DES method, could choose from STAR-CCM+ physics model. Spalart-Allmaras DES method is suitable for moderate separation flow field case and more recommended for airfoil application. SST K-Omega DES has character of simulate highly separated flow, therefor SST K-Omega DES method is choose for our two phase liquid breakup application. All SST K-Omega DES are constructed based on SST K-Omega, a RANS, LES judgment workflow of transport equation and dissipation term from Menter and Kuntz are describe as follows:

$$D_k = \rho \beta^* f_{\beta^*} \omega k \varphi \tag{22}$$

$$\varphi = \{ \begin{matrix} 1 \; if \; l_t < C_{des}\Delta \rightarrow RANS \; mode \\ > 1 \; if \; l_t > C_{des}\Delta \rightarrow LES \; mode \end{matrix} \tag{23}$$

Where:

$$\varphi = max\left(\frac{l_t}{C_{des}\Delta}F, 1\right) \tag{24}$$

$$F = 1 - F_2 \tag{25}$$

$$l_t = \frac{\sqrt{k}}{\beta^*\omega} \tag{26}$$

Δ is the largest distance between the center of cells from neighboring and F_2 is the blending function is SST K-Omega model. C_{des} is model constant which blends the values obtained from independent calibration of K-Epsilon and SST K-Omega model as shown

$$C_{des} = C_{des,k-\omega}F_1 + C_{des,k-\varepsilon}(1 - F_1) \tag{27}$$

4.5 Large Eddy Simulation (LES)

Large eddy simulation (LES) is a transient technique in which the large scales of the turbulence are solved and the small-scale motions are modeled. The turbulence structure is shown in Figure 4-1, we could observe that there are large and small structure of turbulence. LES technique solves more turbulence behavior than modeling of it, therefore LES could better predict the turbulent

flow behavior. However compare to RANS solver LES required finer mesh in order to solve effective eddy sizes and this makes LES becomes more computational expensive to RANS solver. Due to the computer technology rapidly growth in last two decades. The computational power become available for LES approach and this makes LES catch more attention in the last few years especially in two phase flow, atomization and combustion research field.

The disadvantage of the approach is computational expense. The continuity and momentum equation of incompressible Navier-Stokes equations are

$$\frac{\partial u_i}{\partial x_i} = 0 \tag{28}$$

$$\frac{\partial u_i}{\partial t} = -\frac{\partial u_i u_j}{\partial x_j} + X_i - \frac{1}{\rho}\frac{\partial p}{\partial x_i} + v\frac{\partial^2 u_i}{\partial x_j{}^2} \tag{29}$$

Where u_i are ith component flow velocities, X_i are the ith component of body forces which is gravity in this study, ρ is the density of fluid, p is the pressure fluctuation, v is the kinematic viscosity of the fluid, t is time and x_i are the ith coordinate component. A numerical integration of equations (28) and (29) is called Direct Numerical Simulation (DNS). For LES the equations need to be spatially filtered into resolved-scale component and subgrid scale (SGS) component, the resolved-scale component is defined as

$$\widetilde{v_\iota}(x_i) = \iiint v_i(x_i')G(x_i - x_i')dx_i' \qquad (30)$$

Where $\widetilde{v_\iota}$ are ith component resolved-scale component variable as function of space. G is a three dimensional filter function, and subgrid scale component are marked with prime ($'$). After filtering procedure applied to N-S momentum equation produced the equation describe resolved-scale or large eddies

$$\frac{\partial \widetilde{u_\iota}}{\partial t} = -\frac{\partial \widetilde{u_\iota}\widetilde{u_j}}{\partial x_j} - \frac{\partial \tau_{ij}}{\partial x_j} + X_i - \frac{1}{\rho}\frac{\partial \widetilde{p}}{\partial x_i} + v\frac{\partial^2 \widetilde{u_\iota}}{\partial x_j{}^2} \qquad (31)$$

Where the SGS stress is defined as $\tau_{ij} = \widetilde{u_\iota u_j} - \widetilde{u_\iota}\widetilde{u_j}$.

LES require a subgrid scale model to simulate subgrid turbulence instead solving them directly. Smagorinsky Subgrid Scale model [61] is the earliest LES Subgrid Scale model which applies mixing length hypothesis to model the subgrid scale stresses. Over several decade of development the subgrid scale mode evolves better in predicting flow field. WALE (Wall-Adapting Local Eddy-viscosity) subgrid model [62] is the latest model which applied widely in academic and industry.

WALE model applies an algebraic formulation to model the subgrid scale stresses. The WALE subgrid model is the latest and least computationally expensive subgrid scale modeling approach.

$$\mu_t = \rho \Delta^2 S_w \tag{32}$$

$$\Delta = \begin{cases} C_w V^{1/3} & \textit{if length scale limit is not applied} \\ \min(\kappa d, C_w V^{1/3}) & \textit{if length scale limit is applied} \end{cases} \tag{33}$$

Where κ is the von Karman constant with value of 0.41. The deformation parameter S_w is defined as following

$$S_w = \rho \frac{S_d : S_d^{3/2}}{S_d : S_d^{5/4} + S : S^{5/2}} \tag{34}$$

$$S = \frac{1}{2}(\nabla v + \nabla v^T) \tag{35}$$

$$S_d = \frac{1}{2}(\nabla v \cdot \nabla v + (\nabla v \cdot \nabla v)^T) - \frac{1}{3}tr(\nabla v \cdot \nabla v)\mathbf{I} \tag{36}$$
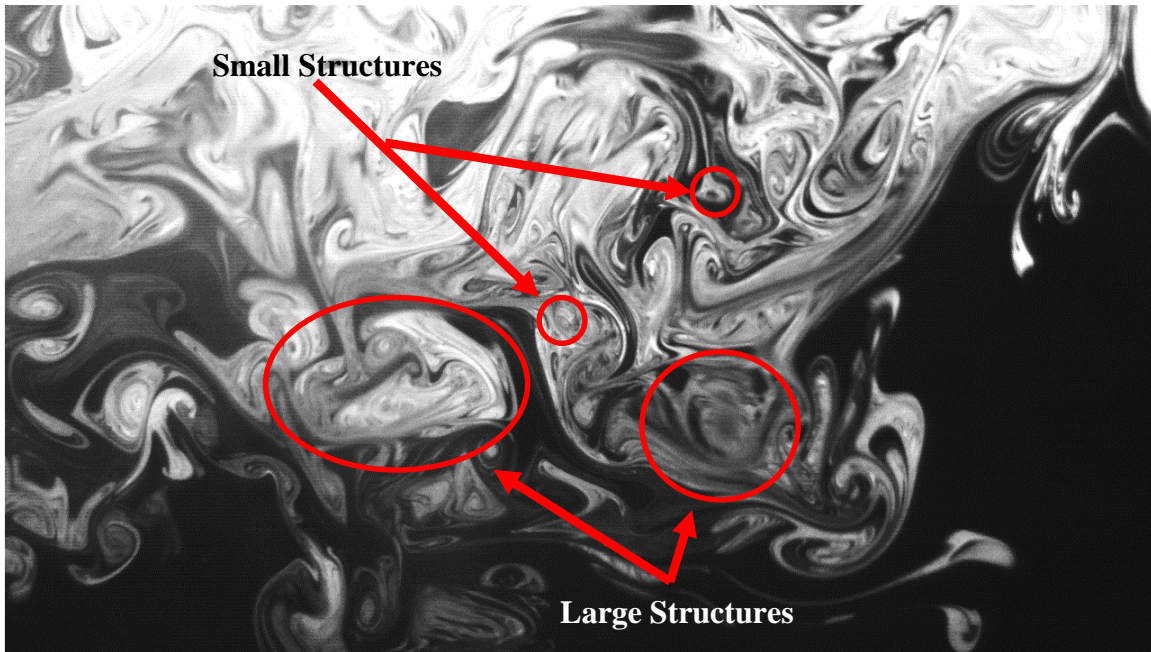
Figure 4-1 Large and small scale of flow eddies (Photography by UW-Milwaukee Wind Tunnel Lab)

4.6 Volume of Fluid (VOF)

The VOF model equations are shown in the following.

$$\rho = \underset{n}{\Sigma}\rho_n\alpha_n \tag{37}$$

$$\mu = \sum_n \mu_n \alpha_n \tag{38}$$

$$c_p = \sum_n \frac{(c_p)_n \rho_n}{\rho} \alpha_n \tag{39}$$

Where ρ_n, μ_n and $(c_p)_n$ are the density, molecular viscosity and specific heat of n-th phase, and volume fraction α_n is described as:

$$\alpha_n = \frac{V_n}{V} \tag{40}$$

The conservation equation that describes the transport of volume fraction α_n without source or sink term is described as:

$$\frac{d}{dt} \int_V \alpha_n \, dV + \int_S \alpha_n (v - v_g) \cdot da = \int_V (-\frac{\alpha_n}{\rho_n} \frac{D\rho_n}{Dt}) \, dV \tag{41}$$

Where v and v_g are fluid velocity and grid velocity respectively, and ($D\rho_n / Dt$) is the material derivative of the phase densities ρ_n.

5   Flow Channel Experiment Result and Discussion

The purpose of experiment part of this study is based on two major reason, first is to provide a good validation data for CFD to validate, the validation standards include Welch frequency analysis data and droplet particle volume to size distribution. Second part is provide valuable high speed image data for liquid breakup study. We will use the image data to analyses and figure out the correlation of droplet particle volume to size distribution by testing different setup of air velocity and surface tension. The experiment is conduct by the apparatus of two phase air-water flow channel controlled with the experiment variables include air velocity, water velocity and surface tension of water. All of the experiment data will be captured by a high speed camera operate with frame rate of 1,000 fps and 1280×1024 image resolution.

5.1   Flow Channel Experiment setup

The geometry setting of this experiment is outlined in chapter 3.2. The experiment setup variable include three different air velocity setting of 20m/s, 30m/s and 40m/s which provide different values of Reynolds number and Weber number. Water velocity is controlled and maintained at 0.67 m/s throughout all different experiment cases. The water surface tension is another variable input of regular water setting of 0.074 N/m and reduced water surface tension setting of 0.040N/m. The purpose of change is the surface tension of liquid is to observe the significance of surface tension to liquid breakup phenomenon. The surface tension reduction is achieved by adding 15ppm of commercial detergent into normal water.

5.2 Flow Channel Experiment Image comparison

The images are the result of experiments combined with three different air velocity and two different liquid surface tension setup. The air velocity setups are 20, 30 and 40m/s and liquid surface tension setup are 0.074 N/m and 0.040 N/m. All of the cases combination detail is listed in Table 5-1, and images of six cases from experiment result are shown from Figure 5-1 to Figure 5-6. A reference time step is set as initial time at this point (t=0 msec) when wave crest pass above ramp. Breakup evolution time interval in the figures in this chapter are 10 msec.

Overall, the liquid pattern is clear to distinguish from low to high air velocity setup, but less significant when compare cases form different surface tension setup when observe just by human eye without any support of post process tool. The breakup processes evolution of case 1 and 2 with Vair = 20 m/s are shown in Figure 5-1 and Figure 5-2, it could be observed that when wave crest pass above the ramp (t= 0 msec), the liquid on the crest start to deform and speed up by moving air and breakup into major separate water bodies (t= 40 msec). The water bodies keep evolve and breakup into smaller droplets (t= 60 msec). The water behavior results from case 1 and case 2 of different surface tension setting seems similar when observe without any support of post process tool.

Table 5-1 Experiment air velocity and liquid surface tension variable combination cases

	Liquid Surface Tension	
	Normal Water 0.074 N/m	Reduced Surface Tension 0.040 N/m
Vair = 20 m/s	Case 1 (Figure 5-1)	Case 2 (Figure 5-2)
Vair = 30 m/s	Case 3 (Figure 5-3)	Case 4 (Figure 5-4)
Vair = 40 m/s	Case 5 (Figure 5-5)	Case 6 (Figure 5-6)

The breakup evolution of case 3 and 4 with Vair = 30 m/s setup are shown in Figure 5-3 and Figure 5-4. The liquid breakup process start when liquid wave crest pass above the ramp (t=0 msec). The liquid in the crest region interact and been accelerated by faster moving air (t = 20msec). A separation of major separate water body starts at time of 30 msec after initial point. The water body contains finer detail boundary shape by compare to the cases from Vair = 20 m/s setup due to higher Reynolds number turbulent behavior. The major water body separated into smaller water body at time of 50 msec point and the smaller water body will breakup into droplets as demonstrate in t = 60 msec. In this setup of Vair = 30 m/s, little difference shows the behavior of the breakup pattern between normal and reduced surface tension setup.

The breakup evolution of case 5 and 6 with Vair = 40 m/s setup are shown in Figure 5-5and Figure 5-6. In this setup, water flow pattern are much more chaotic compare to two lower air velocity cases. Liquid breakup process are taking place every moment throughout the filming time period. There is major separate water body after water crest pass the ramp (t=30msec) this water body is keeping breakup into smaller droplet. In this setup of Vair = 40 m/s, the droplet breakup are more chaotic than cases of Vair = 30 m/s and the droplet count are more as well. Finally, the behavior of the breakup pattern of Vair = 40m/s cases between normal and reduced surface tension setup are similar as well without the support of post process analyze tool. The analyze result of all 6 cases will be further discussed in chapter 5.3 and 5.4.

T= 0 msec

T= 10 msec

T= 20 msec

T= 30 msec

T= 40 msec — Major separate breakup body

T= 50 msec

T= 60 msec — Breakup droplets
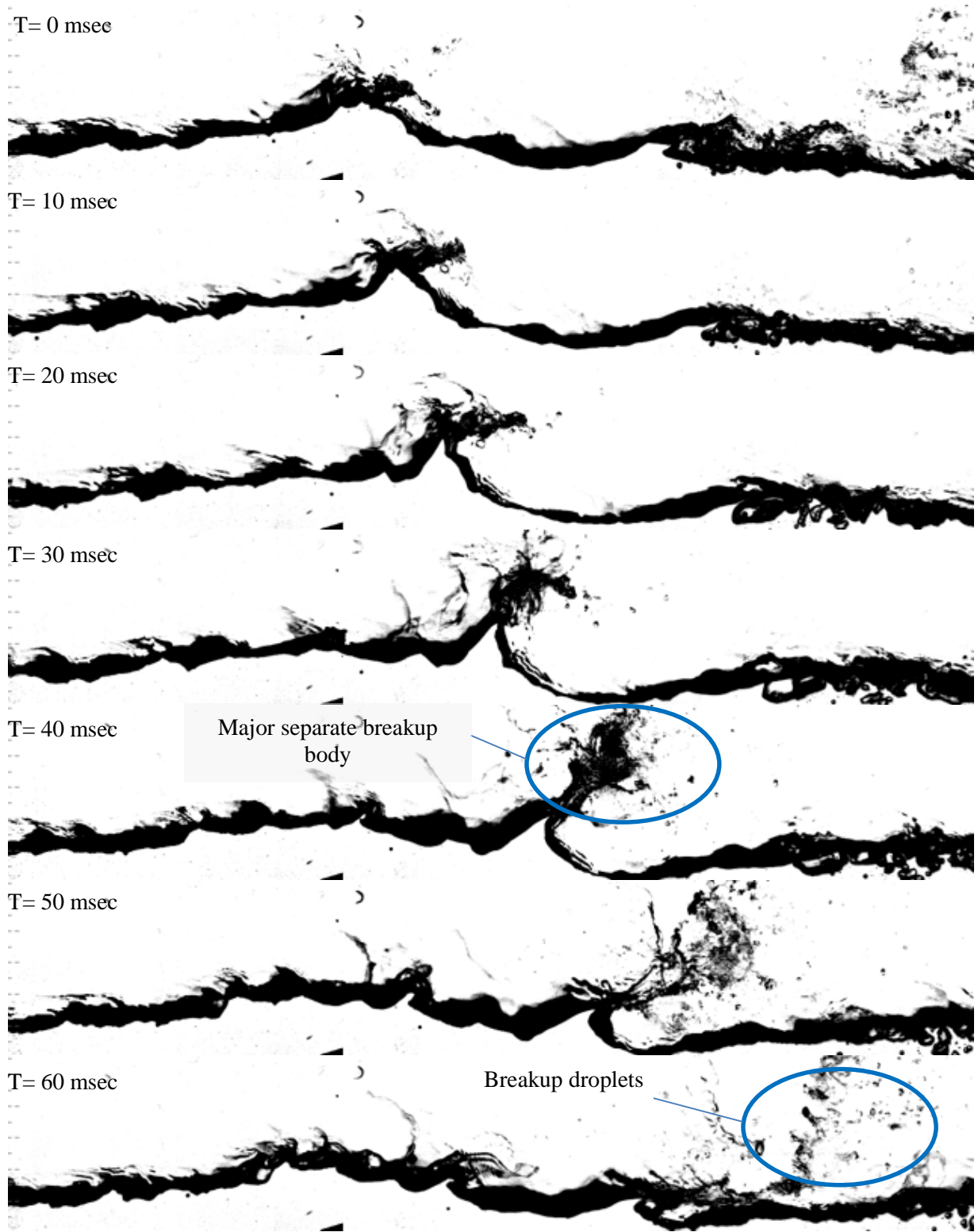
Figure 5-1 Normal water surface tension (0.074N/m) with V$_{air}$=20m/s (Time interval = 10 msec)

T= 0 msec

T= 10 msec

T= 20 msec

T= 30 msec

T= 40 msec

T= 50 msec   Major separate breakup
                                      body

T= 60 msec   Breakup droplets
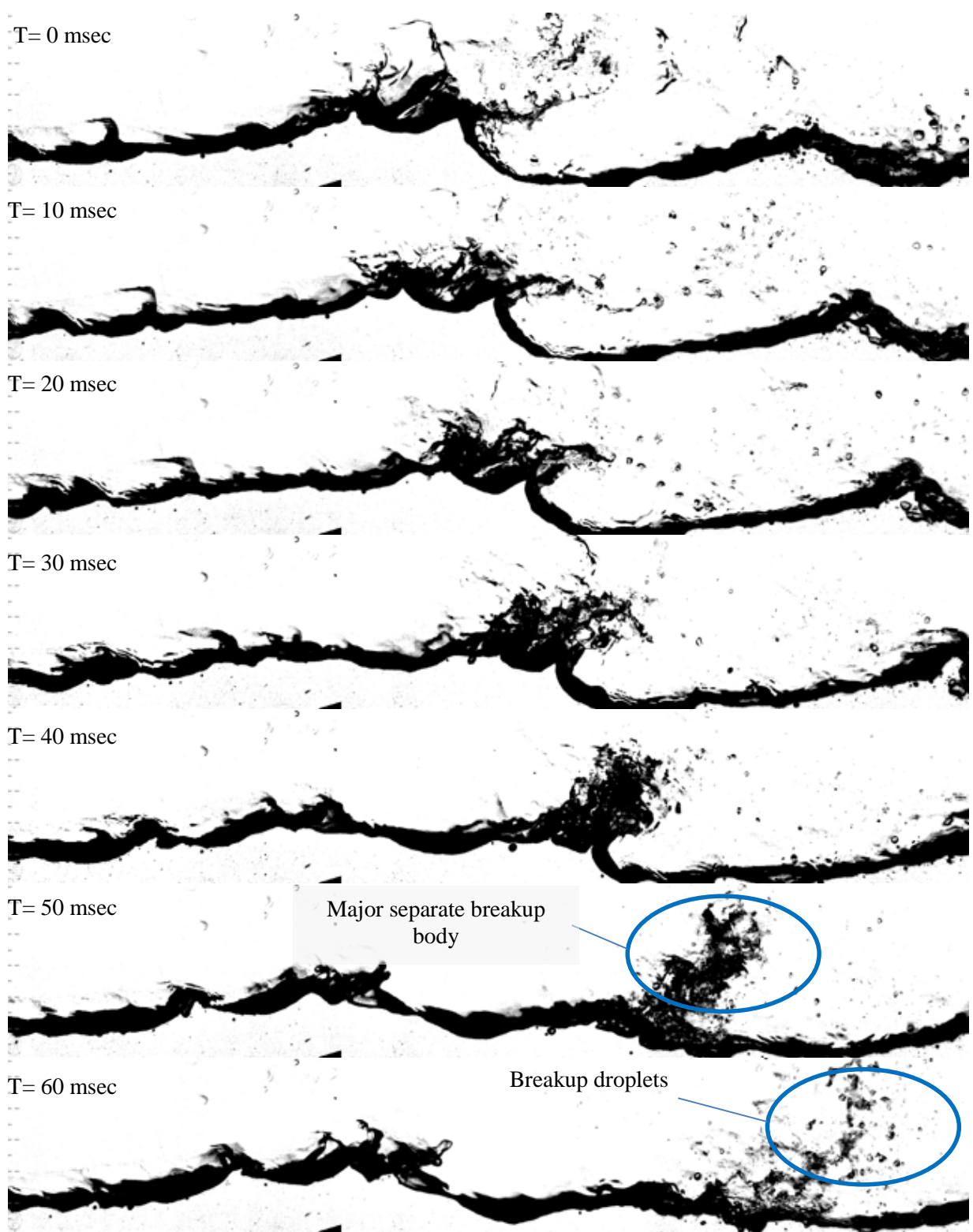
Figure 5-2 Reduced water surface tension (0.040N/m) with V_{air}=20m/s(Time interval = 10 msec)

T= 0 msec

T= 10 msec

T= 20 msec

T= 30 msec Major separate breakup
                 body

T= 40 msec

T= 50 msec Smaller water body
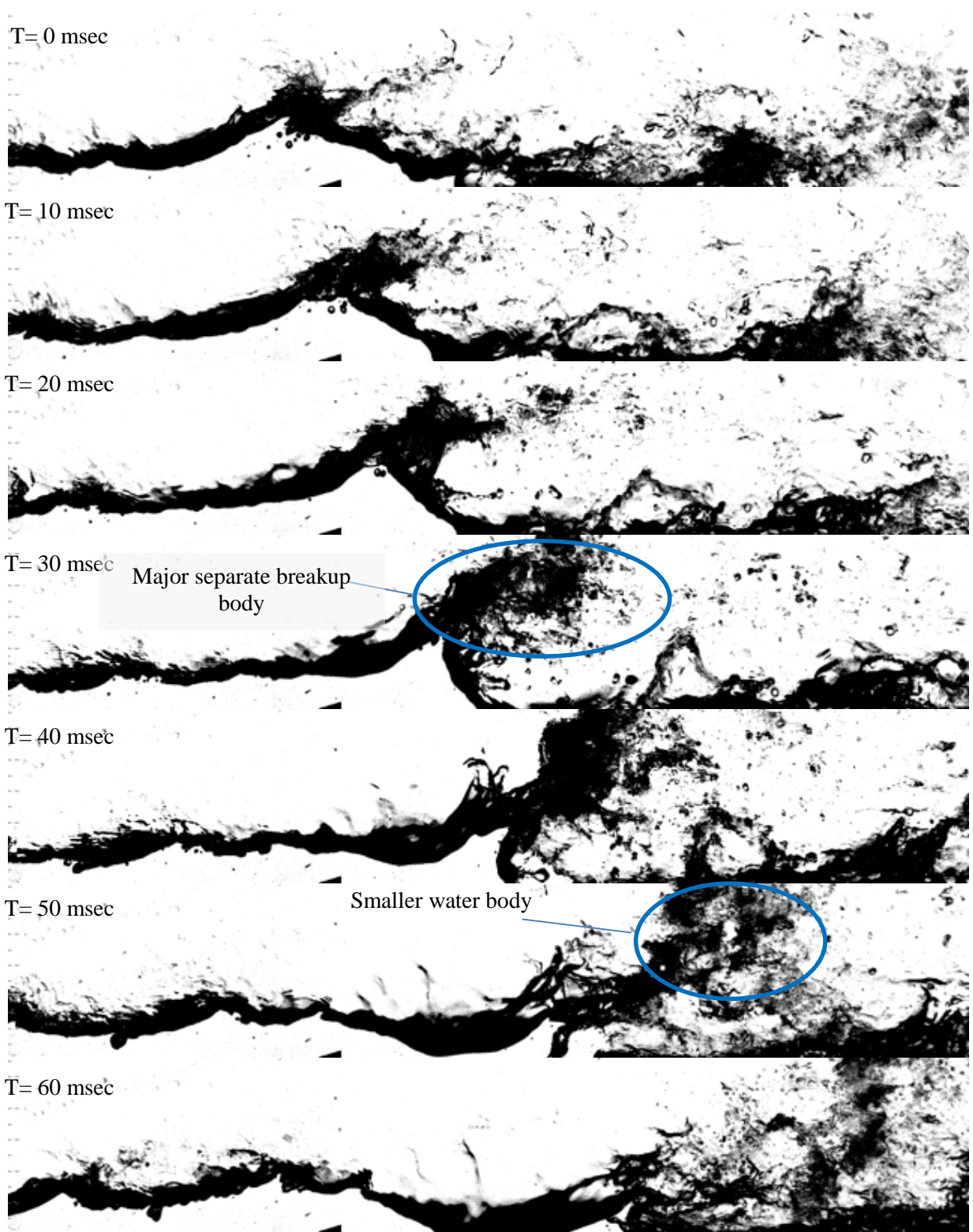
T= 60 msec

Figure 5-3 Normal water surface tension (0.074N/m) with V_{air}=30m/s (Time interval = 10 msec)

T= 0 msec

T= 10 msec

T= 20 msec

T= 30 msec   Major separate breakup body

T= 40 msec

T= 50 msec   Small water body
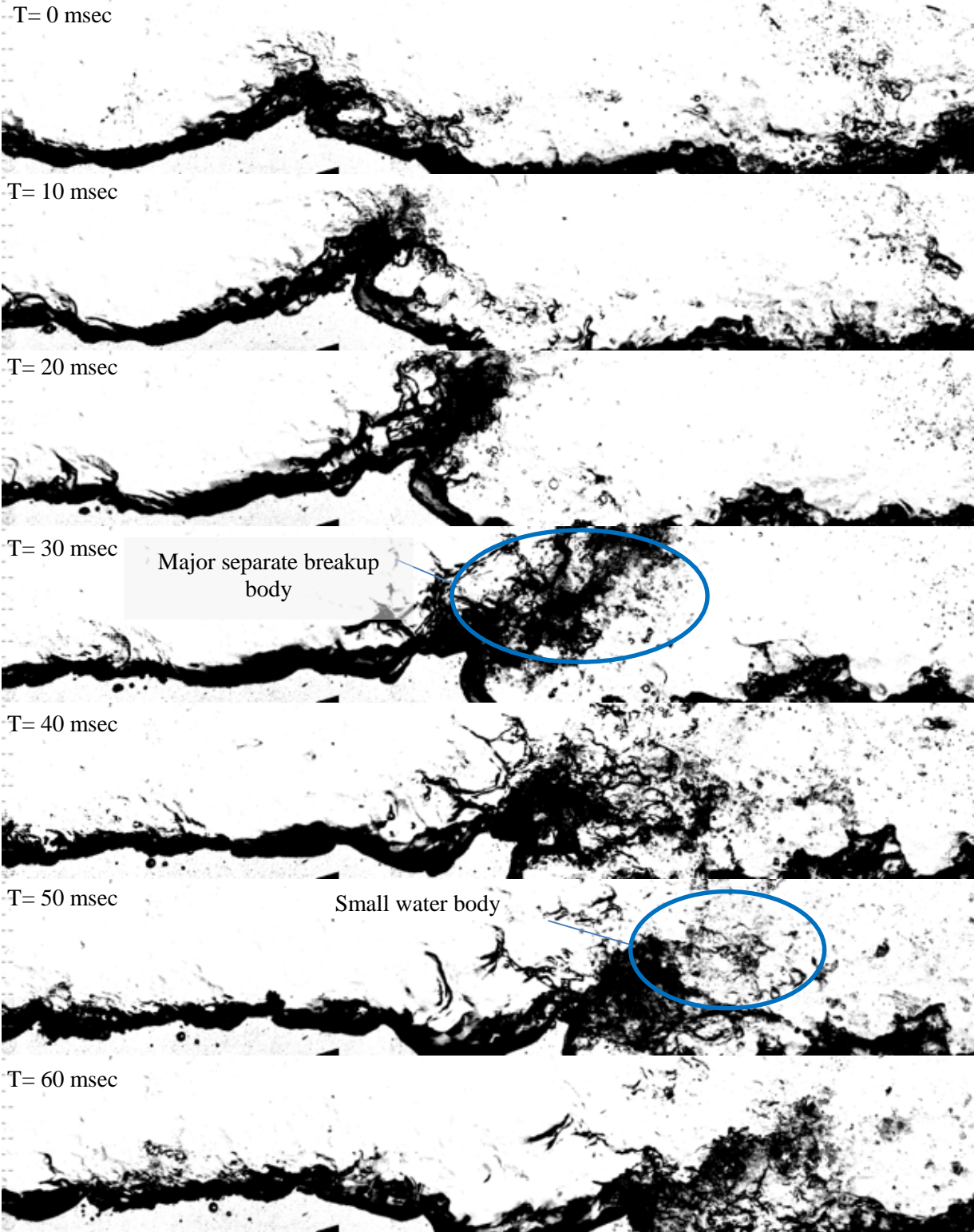
T= 60 msec

Figure 5-4 Reduced water surface tension (0.040N/m) with V$_{air}$=30m/s (Time interval = 10 msec)

T= 0 msec

T= 10 msec

T= 20 msec

T= 30 msec

Major separate breakup body

T= 40 msec

Droplets
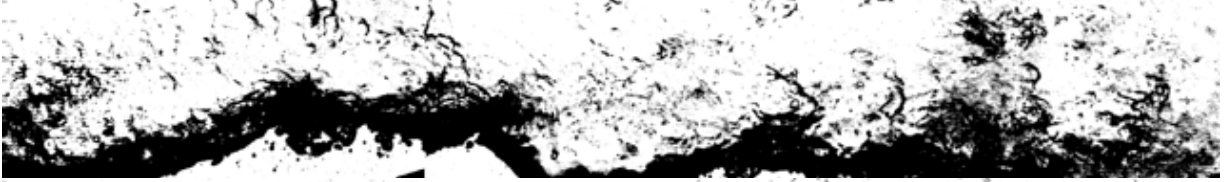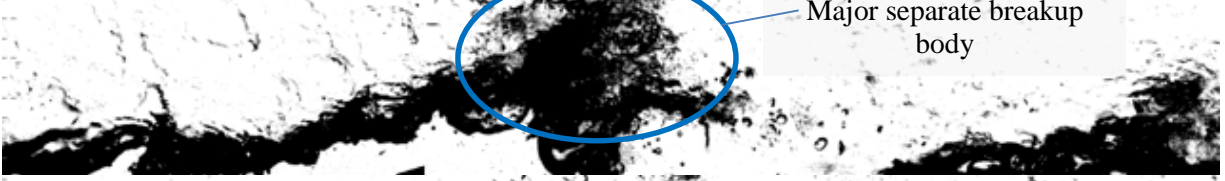
T= 50 msec

T= 60 msec

Figure 5-5 Normal water surface tension (0.074N/m) with V_{air}=40m/s (Time interval = 10 msec)

T= 0 msec

T= 10 msec

T= 20 msec

T= 30 msec

Major separate breakup body

T= 40 msec

Droplets

T= 50 msec

T= 60 msec
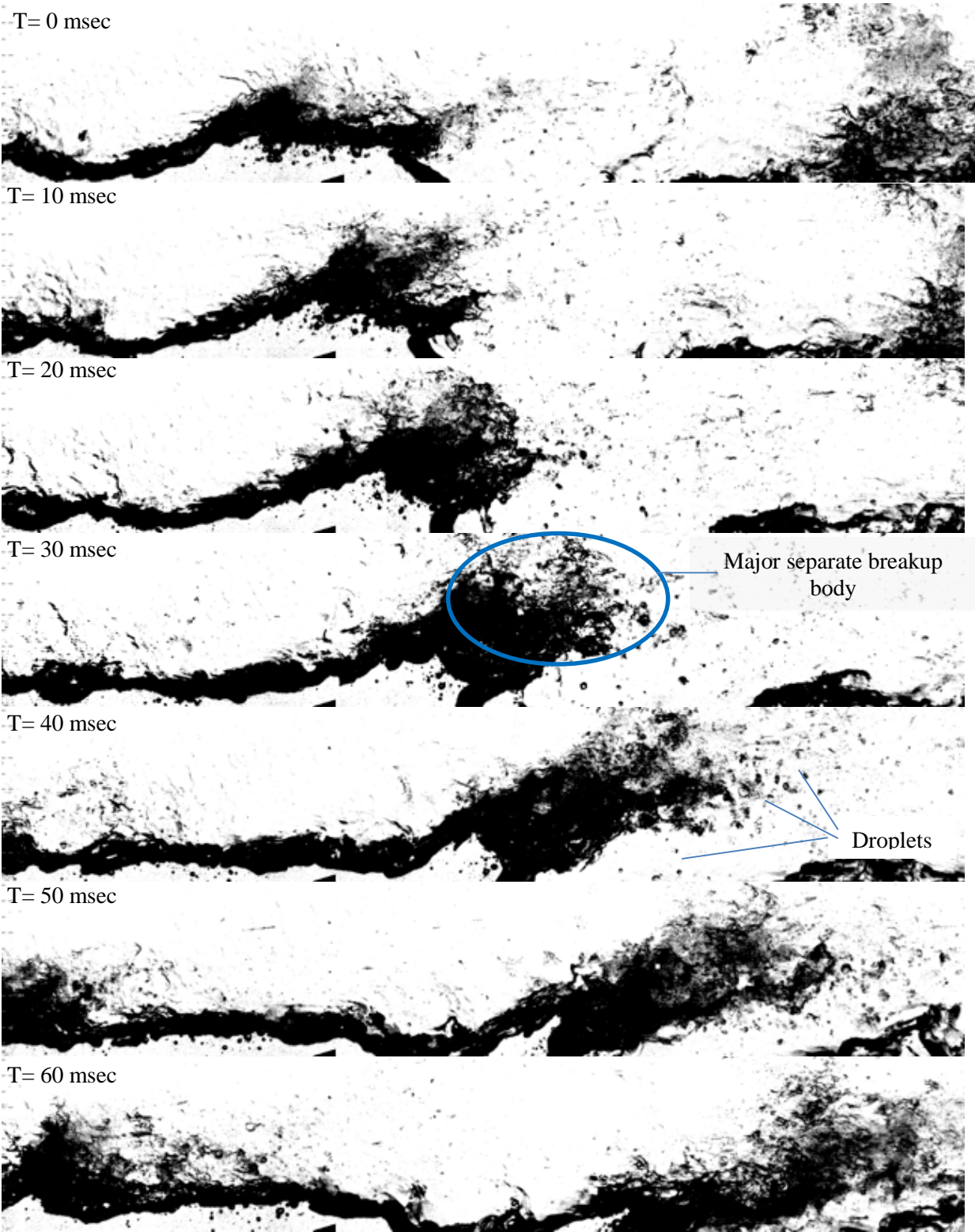
Figure 5-6 Reduced water surface tension (0.040N/m) with V$_{air}$=40m/s (Time interval = 10 msec)

74

5.3 Flow Channel Experiment Welch Frequency Analysis

The Welch's frequency analysis method is developed by P.D. Welch [63] as a modification of Fast Fourier Transform (FFT) tool. Generally FFT is widely used for frequency analysis, but the result of FFT frequency spectrum is noisy and not easy to apply and compare especially for some cases with subtle difference. Welch's method use time average method and the result of spectrum act as a better tool for case to case comparison.

5.3.1 Flow Channel Experiment Free Water Surface Location

Free water surface location at ramp raw data is used as input for Welch's method. The data extraction is done by analyze the free water surface location above ramp in each image. As shown in Figure 5-7, Matlab image recognize code created in our lab could help us to target the location of water surface and export the position data for each frame. After the location data is calculated in each image, a red dot will be placed in the location. We will be able to spot if our MatLab code make mistake during recognition process.
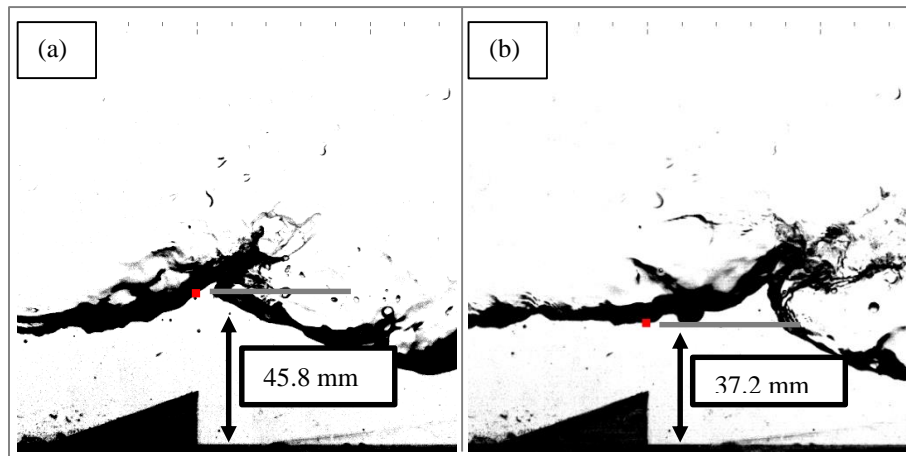
Figure 5-7 Wave location demonstration in case of water with Vair=20m/s in (a) frame number 1 (b) frame number 20

The total image number of flow channel experiment in each case is 6,540. Time interval between images to images is 1 msec and total length of time from high speed camera is 6.54 sec. All 6 cases from controlled variable of air velocity and surface tension (shown in Table 5-1) are processed and raw wave location history data are exported and will be used for Welch's frequency analysis part. The flow channel experiment raw wave location data are shown from Figure 5-8 to Figure 5-10 for cases of Vair = 20m/s to 40m/s. Data of normal water and reduced surface tension water are arranged in same figure from top to bottom. By observing the wave location history for each case we could find that higher air velocity will result in lower the wave location, and this is make sense due to higher air velocity increase the breakup activity when wave crest reaches above ramp, when more volume of liquid breakup from main body. When more liquid breakup activity takes place more water turn into droplet from main water body and the result is lower wave location. It is not clear to observe the difference between cases of normal water to reduced surface tension water from the raw image. The averaged wave location value for each case are listed in Figure 5-11. The average location of Vair 20, 30 and 40m/s are 39.6 mm, 35.1 mm and 31.2 mm respectively. It is clear that this figure shows higher the air velocity result in lower the average wave location. Which means more water breakup into droplet from main water body and result in lower averaged wave location. The average location of water with reduced surface tension setting is also lower than normal water for all three air velocity setting. The reduced surface tension has averaged lower wave location value of 1.8%, 1.0% and 1.7% for the case of Vair 20m/s, Vair 30m/s and Vair 40m/s, respectively. The lower average wave location result also support that lower liquid surface tension could enhance liquid breakup activity.
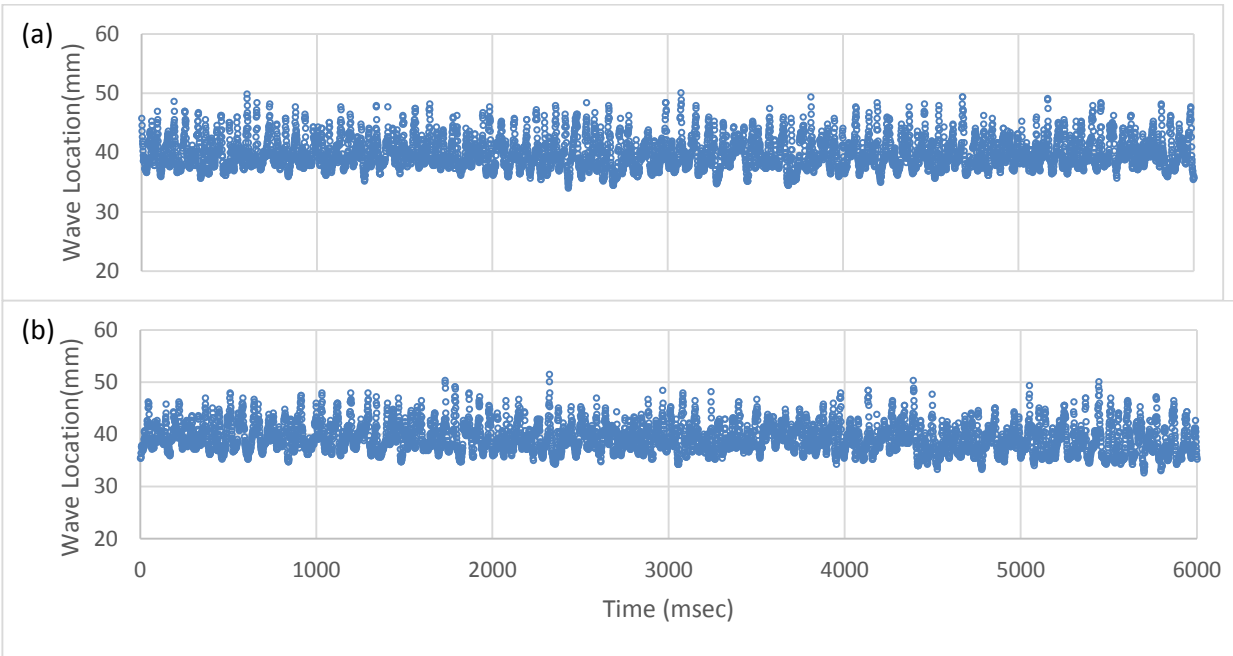
Figure 5-8 Free water surface location at ramp with V_{air}=20m/s for (a) Normal water (b) Water of reduced surface tension
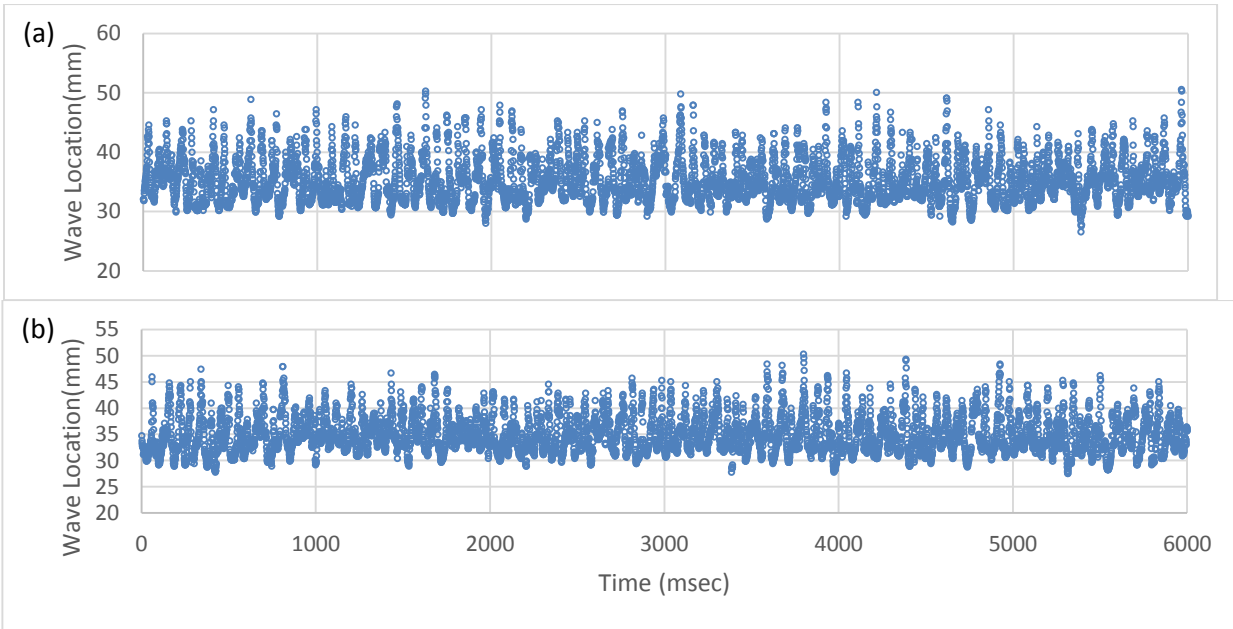
Figure 5-9 Free water surface location at ramp with V_{air}=30m/s for (a) Normal water (b) Water of reduced surface tension
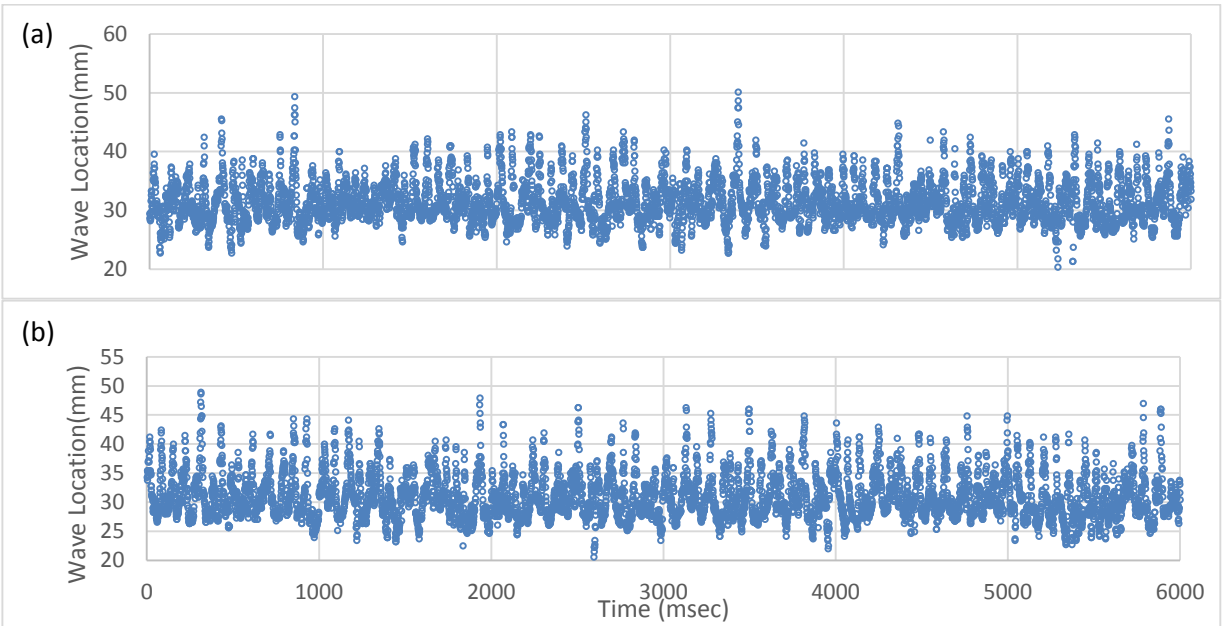
Figure 5-10 Free water surface location at ramp with V_{air}=40m/s for (a) Normal water (b) Water of reduced surface tension
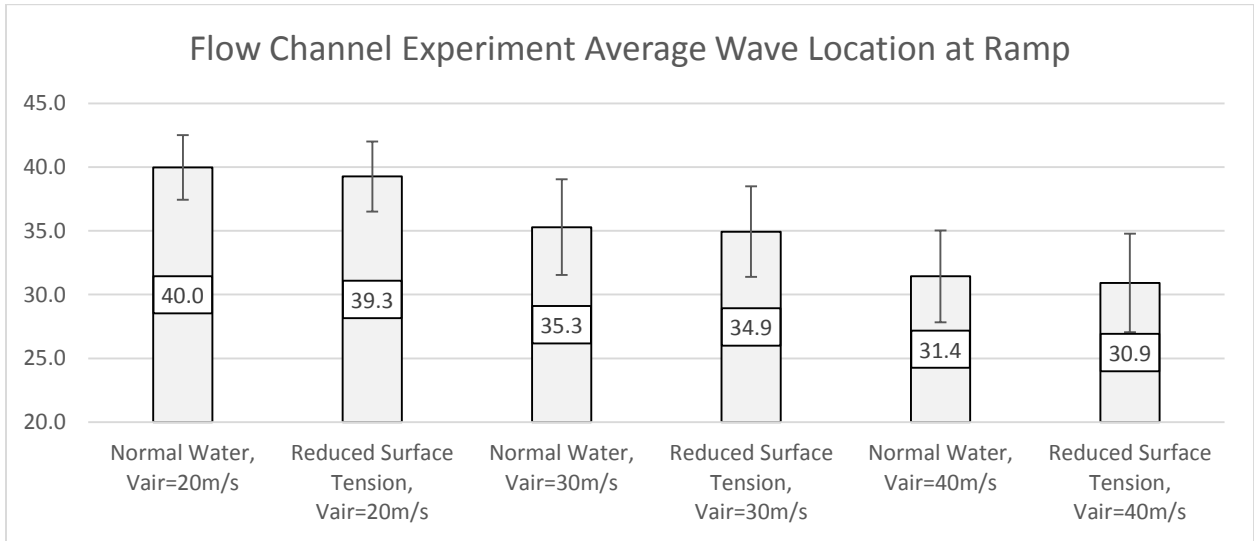
Figure 5-11 Flow channel experiment average wave location at ramp for all 6 cases in flow channel experiment

5.3.2　Flow Channel Experiment Welch Frequency Analysis

The overview Welch frequency analysis of two-phase free surface wave location from flow channel experiment are shown in Figure 5-12. It is clear that for frequency region higher than 250 Hz, higher air velocity result in higher magnitude in this region for both normal water and reduced surface tension case, for instance the magnitude of Vair = 40 m/s has value about one order higher than that from Vair=20m/s. The peak frequency for normal water cases are 16.5Hz, 13.1Hz and 14.1Hz for Vair = 20m/s, 30 m/s and 40m/s, respectively. The peak frequency for reduced water surface tension cases are 15.1Hz, 16.6Hz and 16.1Hz for Vair = 20m/s, 30 m/s and 40m/s, respectively. The peak frequency for all experiment cases are listed in Table 5-2. There is no significant difference between cases from low air velocity to high air velocity, as well as normal surface tension to reduced surface tension. This could be explained by Froude number (Fr) which is defined as fluid velocity over square root of multiplication of gravitational constant and liquid depth as shown in equation (42).

$$Fr = \frac{v_{liquid}}{\sqrt{gl}} \tag{42}$$

Where v_{liquid} is the liquid velocity, g is the gravity constant and l is the liquid height. Since the liquid velocity and height setting are constant throughout the experiment cases, Froude number is constant throughout cases and result in no significance in terms of peak frequency. Full Welch frequency analysis comparison for both experiment and simulation will discussed in chapter 7.2.
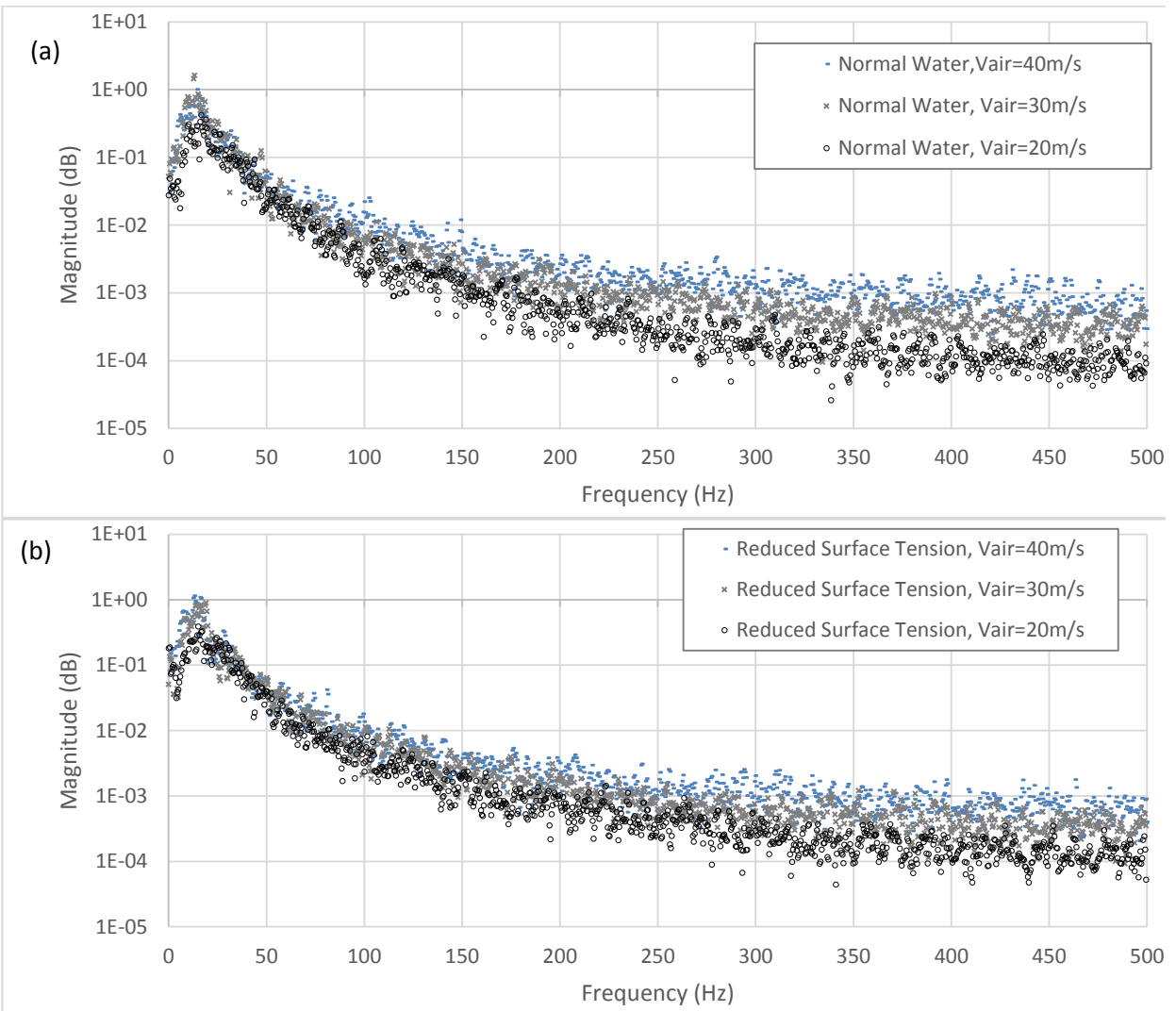
Figure 5-12 Flow channel experiment Welch frequency analysis comparison between Vair = 40 m/s, 30 m/s and 20 m/s of (a) Normal Water (b) Reduced surface tension

Table 5-2 Peak frequency for all experiment cases (Hz)

	Vair=20m/s	Vair=30m/s	Vair=40m/s
Normal Water	16.5	13.1	14.1
Reduced Surface Tension	15.1	16.6	16.1

5.4 Flow Channel Experiment Droplet Volume to Size Distribution

The flow channel experiment droplet volume to size distribution comparison between normal water and reduced surface tension water are shown in Figure 5-13. The data was extract by MatLab image process code developed in UW-Milwaukee wind tunnel lab. The detailed code process work flow is discussed in chapter 3.5.2. The minimum size of droplet could be recognize by high speed camera resolution is 0.24mm per pixel. In terms of data accuracy, for any droplet equivalent diameter smaller than 0.6mm are filter out. In this figure, volume to size distribution per frame is the averaged values from 6,540 frames for each cases. The volume unit is marked in mm^3. It could be observed that cases from different velocity setting is clear to distinguish, as shown in the figure, group (a) of Vair = 40m/s setup has most volume to size distribution curve throughout all range of droplet diameter. Group (b) of Vair = 30m/s data distribution set in the middle and group (c) of Vair = 20m/s has least volume to size distribution for all range of droplet sizes. The reason is cases with high air velocity has more breakup behavior, therefore more water are carried by droplet beside carried by main water body. The phenomenon could also be observed in chapter 5.2.

It could be observed that for cases with different surface tension, the cases with reduced surface tension water has more volume to size distribution than the cases of normal water cases. The reason could also be explained by less surface tension reduces the surface energy. Surface energy of liquid provide bounding force for liquid stay together. When surface tension reduces, less bounding force acting on liquid result more breakup when external disturbance like moving acting on the surface of liquid. The volume to size distribution difference between normal water and surface tension is clear when air velocity = 20ms, however it becomes less significant when air velocity increases to

30m/s and when air velocity reaches to 40m/s, the difference becomes not so clear to observe expect in small droplet diameter region of 0.6~0.8 mm. This phenomenon could be explained through experiment quality as shown in Figure 5-14. When air velocity = 20m/s, the droplet breakup activity is gentle and droplet from liquid breakup is clear to distinguish. When air velocity reaches to 30m/s, the liquid breakup activity behave differently, liquid breakup begins from wave crest reaches to the top of the ramp where water start to deform and breakup into major separate breakup body from main water body. The major separate breakup body keep breakup into smaller liquid droplet. The major separate breakup body is not easy for MatLab droplet coding to distinguish. The situation get worse when air velocity reaches to 40m/s, when air velocity increases, more volume of water is belong to the major separate breakup body and the fuzzy region make the difference between normal water and reduced surface tension water becomes not so clear.

Although it is not easy to distinguish the difference between normal water and reduced surface tension water in the cases of air velocity =40m/s, but in the case of air velocity of 20m/s and 30m/s, it could be confirm that liquid with reduced surface tension will increase liquid breakup activity. In order to further confirm the correlation between liquid breakup and liquid surface tension, a precise controlled single droplet breakup experiment was conduct and documented in chapter 8 which provide more aspect to liquid breakup study.
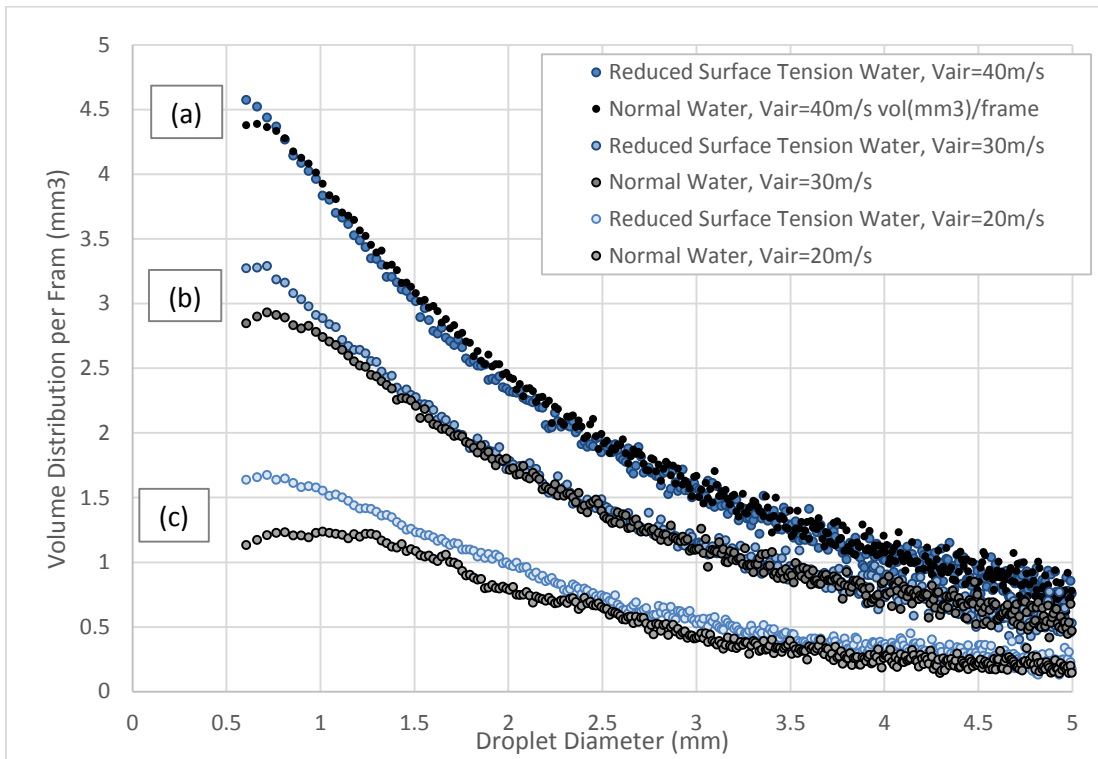
Figure 5-13 Flow channel experiment droplet volume to size distribution comparison between normal water and reduced surface tension water for cases (a) Vair=40m/s, (b) Vair=30m/s and (c) Vair=20m/s.
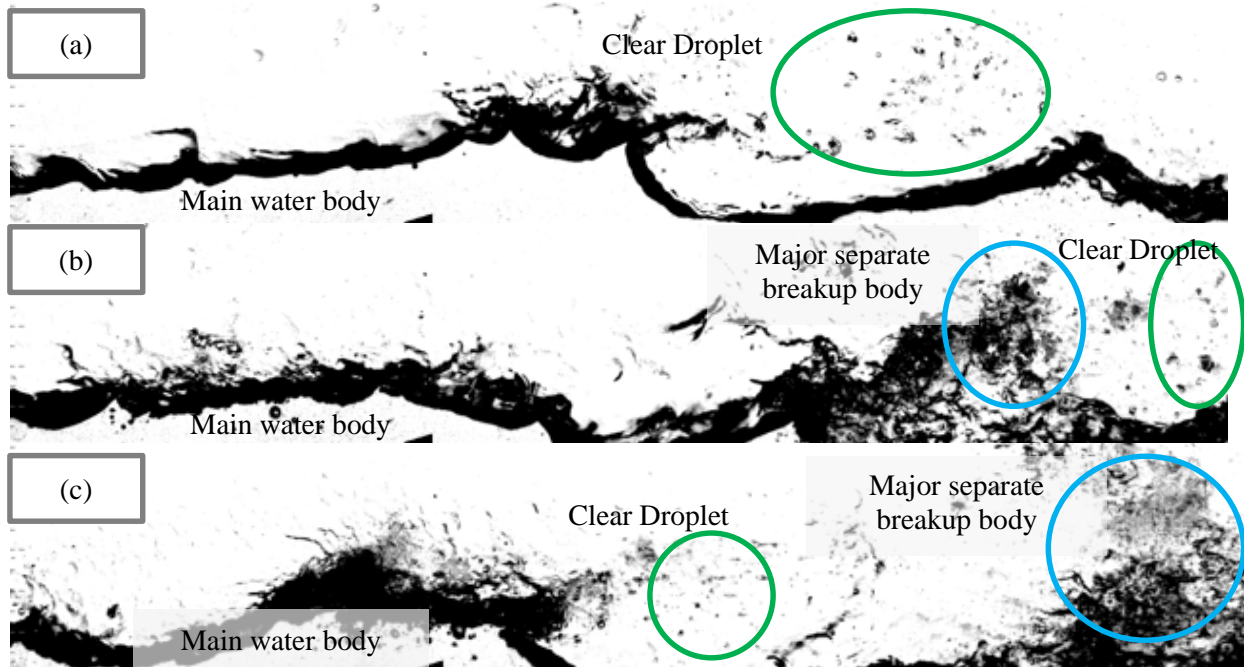
Figure 5-14 Droplet distinguish demonstration for cases form (a) Vair = 20m/s, (b) Vair = 30m/s and (a) Vair = 40m/s

6 Flow Channel Computational Results and Discussion

The purpose of flow channel computational approach is to test the two phase flow prediction ability of Computational Fluid Dynamic (CFD) tool. All of the CFD result will be compared with the result from flow channel experiment data. the simulation work also include six different cases from the combination of Vair = 20m/s , 30m/s and 40m/s and surface tension of normal water (0.074 N/m) and reduced surface tension water (0.040 N/m). The computational work is 3 dimensional LES transient simulation with same dimension compare with experiment flow channel. The cases combination are listed in Table 6-4. The CFD work include first part of CFD grid independent study which help us to apply the simulation with appropriate number of cell. Second part is extracting raw wave history data from simulation images and apply Welch frequency analysis to figure out the frequency spectrum distribution. Third part is use MatLab image process tool developed in UW-Milwaukee wind tunnel lab to extract the droplet volume to size distribution about the code detail are discussed in chapter 5.4.

6.1 Grid Independent Study

The grid independent study for numerical method is carried out before the two-phase flow study begins in order to target a proper grid resolution which will apply to this liquid breakup study. To evaluate the grid resolution, we use two parameters, the total computational time and droplet mass distribution data to help us to judge to what grid resolution level is required. Three different grid setup of 8 million (8 M), 16 million (16M) and 33 million (33M) cell simulation are compared. The simulation comparison is based on the flow channel experiment setup of V_{air}=20m/s and

V_{water}=0.67m/s. In order to reach same numerical stability criteria, the time step of higher resolution grid should be smaller, therefor increase the total computational time for the higher grid resolution simulation. The simulation time step is 2.5 µsec, 5.0 µsec and 10.0 µsec for 33M, 16M and 8M mesh, respectively. Experiment and simulation setup detailed value are listed in Table 6-1 and Table 6-2. All of the simulation in chapter 6.1 are carry out by Large Eddy Simulation (LES) for all different mesh size simulation.

The liquid droplet mass distribution is calculated through the MatLab post data process code. The code is customized to this study with relevant information input include pixel to mm conversion, image size and contrast adjust function. The first stage of the code is starting to crop and zoom all images into exactly same dimensions and scale for comparison. Each image has different contrast due to experiment florescent light source which has about 60Hz light intensity cycles. The second step of the code is to normalize the contract to time averaged value from all 1,200 frames. Once the pre-process is done, the image process code will start to calculate the status of the droplet distribution in each frame for assigned image geographical range. The final step of the code is to output the statistical data of droplet size distribution analyzed from image, the droplet size distribution data will be calculate and convert to the mass distribution data from all 1,200 frames of experiment and simulation images for each case.

Image comparison of mesh independent study of experiment, 8M simulation, 16 M simulation and 33 M simulation are demonstrated in Figure 6-1. It is clear that the breakup droplet is 8M simulation is the coarsest case of all. 16M simulation could show more detail on liquid droplets

and 33M simulation is best case of all in terms of demonstrate the detail of water boundary and

droplet. Overall, more simulation cell result in finer liquid breakup detail.

Table 6-1 Grid independent study simulation setup

	33M Simulation	16M Simulation	8M Simulation
Total simulation cell number	33,267,744	15,979,800	8,124,960
Number of HPC cores applied	192	192	192
Simulated physical time (sec)	1.2	1.2	1.2
Simulation time step (µsec)	2.5	5.0	10.0
Simulation inner iteration	5	5	5
Total iteration	2.4E+6	1.2E+6	6.0E+5
Simulation time (Day)	117	28	7

Table 6-2 Basic image analyze input for both experiment and simulation case for mesh independent study

	Experiment and Simulation image process data input
Data input physical time (sec)	1.200
Time step resolution (sec)	0.001
Total analyzed time steps	1,200
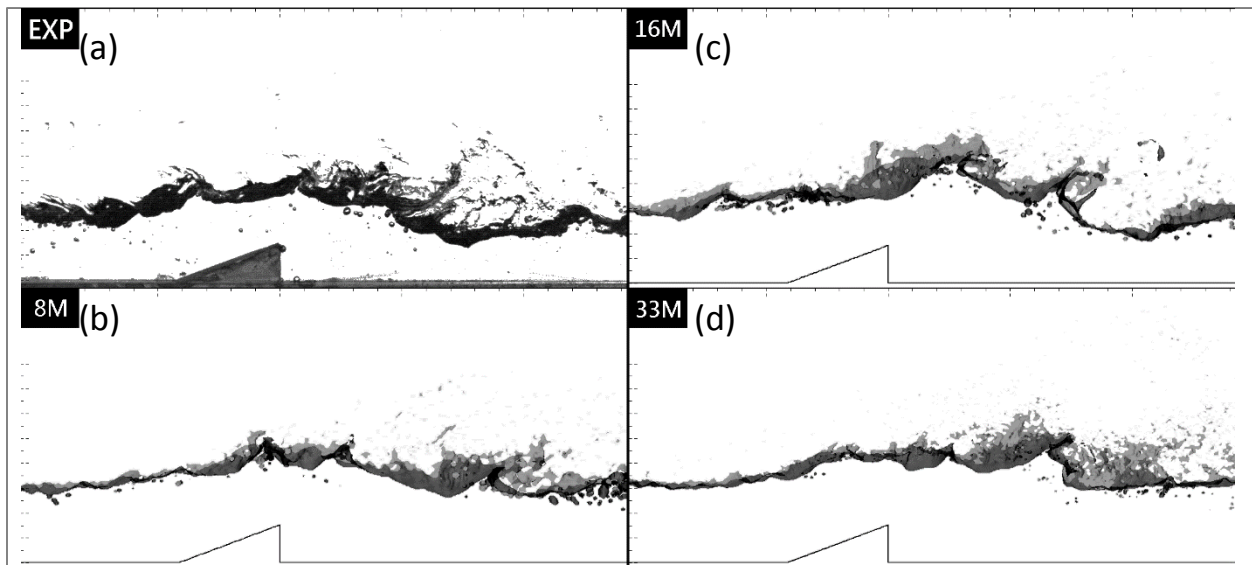
Figure 6-1 Image comparison of mesh independent study carried out under Vair=20m/s with normal water (σ = 0.074N/m). Figure list (a) Experiment, (b) 8M Simulation, (c) 16M Simulation, (d) 33M Simulation

Table 6-3 Experiment and simulation mesh independent study comparison data.

	Experiment	8M Simulation	16M Simulation	33M Simulation
Peak volume distribution size (mm)	1.04	2.60	1.86	1.21
Peak volume distribution size off from Experiment data (mm)	N/A	1.56	0.82	0.17
Peak value of volume per Frame value (mm^3)	1.23	1.09	1.41	1.30
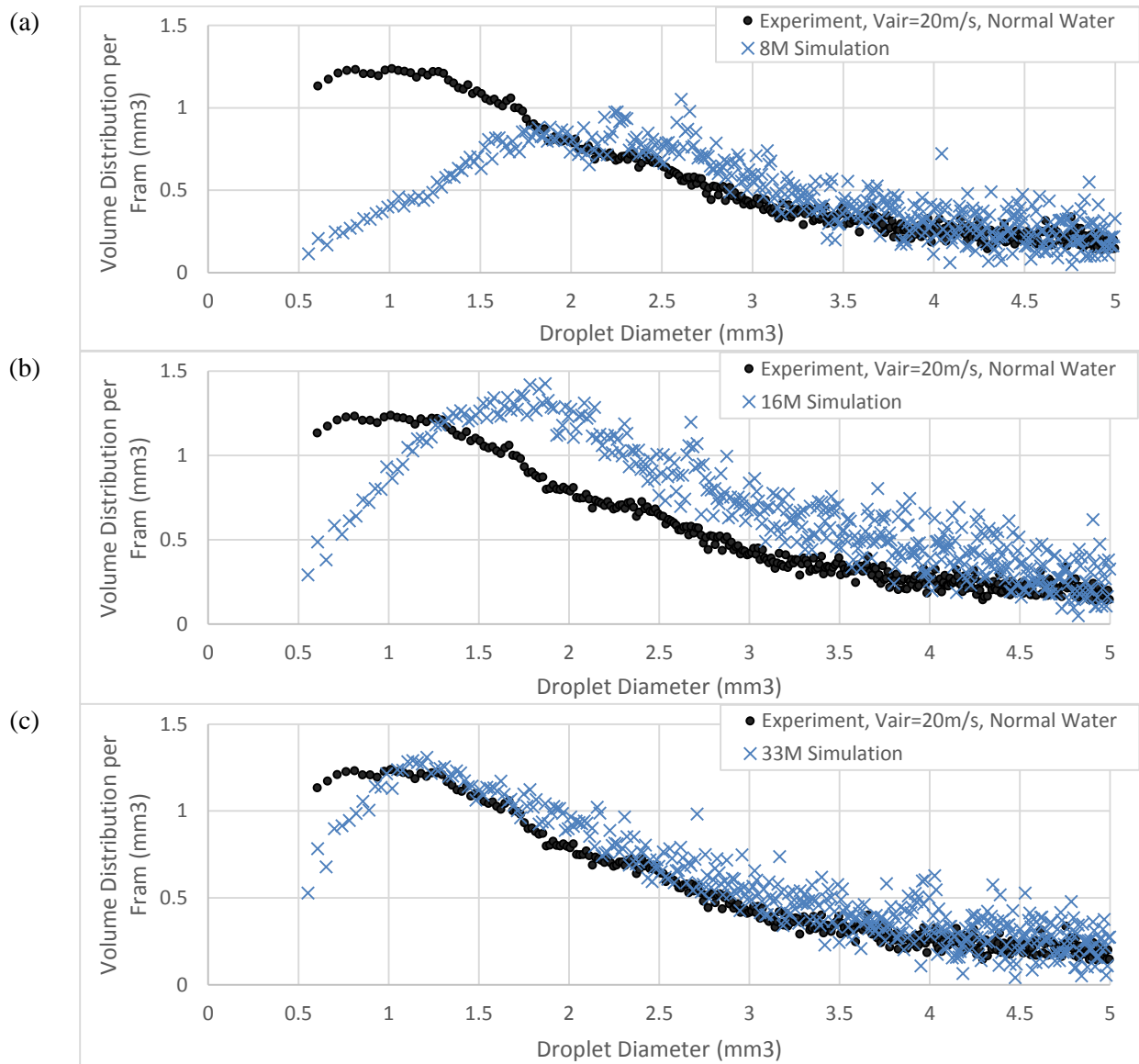
Figure 6-2 Mesh independent study of liquid droplet volume to size distribution (mm³) per frame to equivalent diameter (mm) comparison of Experiment to (a) 8 million grid simulation, (b) 16 million grid simulation, (c) 33 million grid simulation

The liquid volume to droplet size distribution per frame to equivalent diameter result comparison of experiment, 8M simulation, 16 M simulation and 33 M simulation is shown in Figure 6-2. From this figure we could tell that the droplet mass distribution is different from case to case. In Figure 6-2 (a) we could observe that the volume to size distribution trend for droplet diameter larger than 4mm is match with experiment, 8M simulation prediction for droplet diameter range between 2mm to 4mm are slightly over predict. The peak volume to size distribution droplet size for 8M simulation is 2.60 mm compare to that of 1.04 mm in experiment, the 8M simulation is not ideal setup compare to 16M simulation and 33M simulation for this study. The result of 16M simulation is demonstrated in Figure 6-2 (b), the volume to size distribution curve is slight over predict for droplet size range from 1.5mm to 5mm, although the prediction curve is not exact match with experiment the peak volume to size distribution droplet size for 16M simulation is 1.86 mm which is more closer to that from experiment when compare to 8M simulation. The best match case is 33M simulation as shown in Figure 6-2 (c), the volume to size distribution curve matches well from droplet size range from 1.3 mm to 5 mm, and the peak volume to size distribution droplet size is 1.21 mm which is the closest case to that value from experiment of 1.04 mm. All of the peak value of volume to size distribution, corresponding droplet size are listed in Table 6-3. Overall, 33M simulation is the best candidate to carry out CFD work for this study, however, the simulation time for each 33M simulation will require around 120 days under 192 physical computational core with the support of UW-Milwaukee High Performance Computing (HPC) center. Due to the practical concern of this research, our simulation mesh setup will be carried out by 16 million cell mesh.

6.2 CDF Approach Study

This chapter presents a study of air and water two-phase straight channel experiment and the comparison of different Computational Fluid Dynamic (CFD) method based Reynolds-averaged Navier–Stokes (URANS) Reynolds Stress Model (RSM), URANS k-ε model, the Large Eddy Simulation (LES) and Detached Eddy Simulation coupled with URANS k-w (DES k-w). All of the mesh number setup in this section are 16M cell. The experimental work provides validation information for the different CFD approach comparison. The droplet volume to size distribution curve and frequency analysis was carried out to quantify all cases come from CFD. MatLab image process code will be used again in this chapter. All of the image process work flow are documented in chapter 3.5. By comparing the droplet volume to size distribution and Welch analysis from experiment and different CFD method could help us to understand the character and capability of different CFD approach in liquid breakup study. The setup of all CFD case are air velocity =20 m/s, water velocity = 0.67 m/s and normal water surface tension setup (σ = 0.074N/m).

6.2.1 Two-Phase Interaction Analysis of CDF Approach Selection

The results of two-phase flow liquid breakup cycle of the experiment, LES and DES-kw are compared, as shown in Figure 6-3.For cases of Experiment, LES and DES k-w, the cycle initial point is picked when liquid crest propagate to the top point of the ramp and the time interval is 10 milliseconds (ms) between frames to frames. A blue arrow in each frame indicates the location of wave crest under observing. In the experiment series we could observe that some liquid breakup arise on the top to wave crest at 10msec, the liquid breakup activity reaches peak at 40ms, after 40ms the water droplets from breakup are carried away from wave crest by faster moving air,

finally a new liquid breakup cycle begins roughly after 70ms. By comparing the result of an experiment with LES and DES-kw image series, the result of LES method show more similarity with experiment than DES-kw method regarding wave amplitude and liquid breakup behavior. To understand the similarity between experiment and different CFD method, frequency analysis is applied and discussed in section 6.2.3.
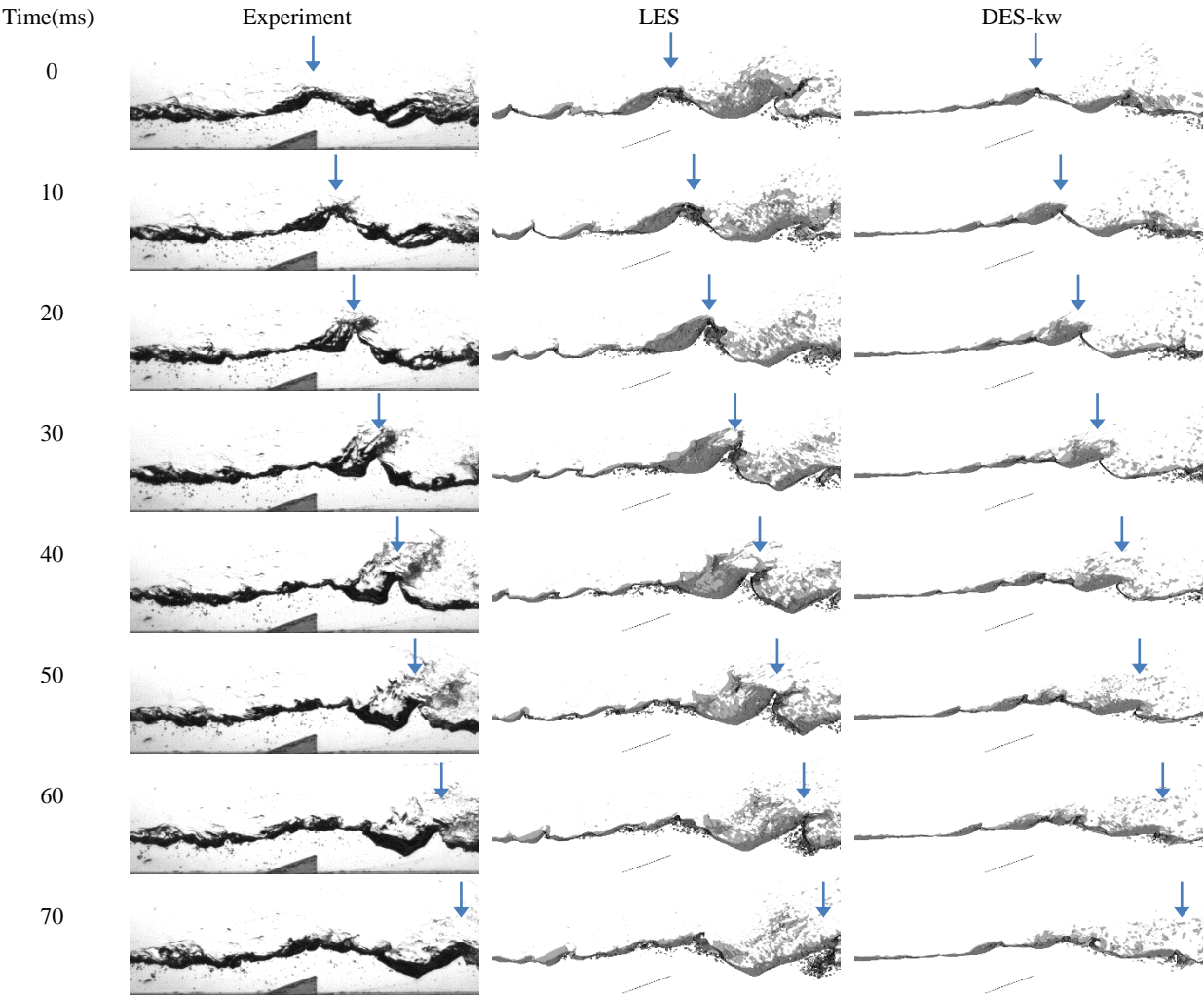
Figure 6-3 Liquid breakup comparison of experiment and CFD method of LES and DES-kw

The comparison of experiment, URANS-RSM and URANS k-ε are shown in Figure 6-4, we could observe that for both URANS-RSM and k-ε approach shows little breakup activity for two-phase flow and it is clear that the performance of liquid breakup of URANS simulation is under estimate when air velocity = 20m/s. it is obvious that LES and DES are better choice for this study than URANS approach.
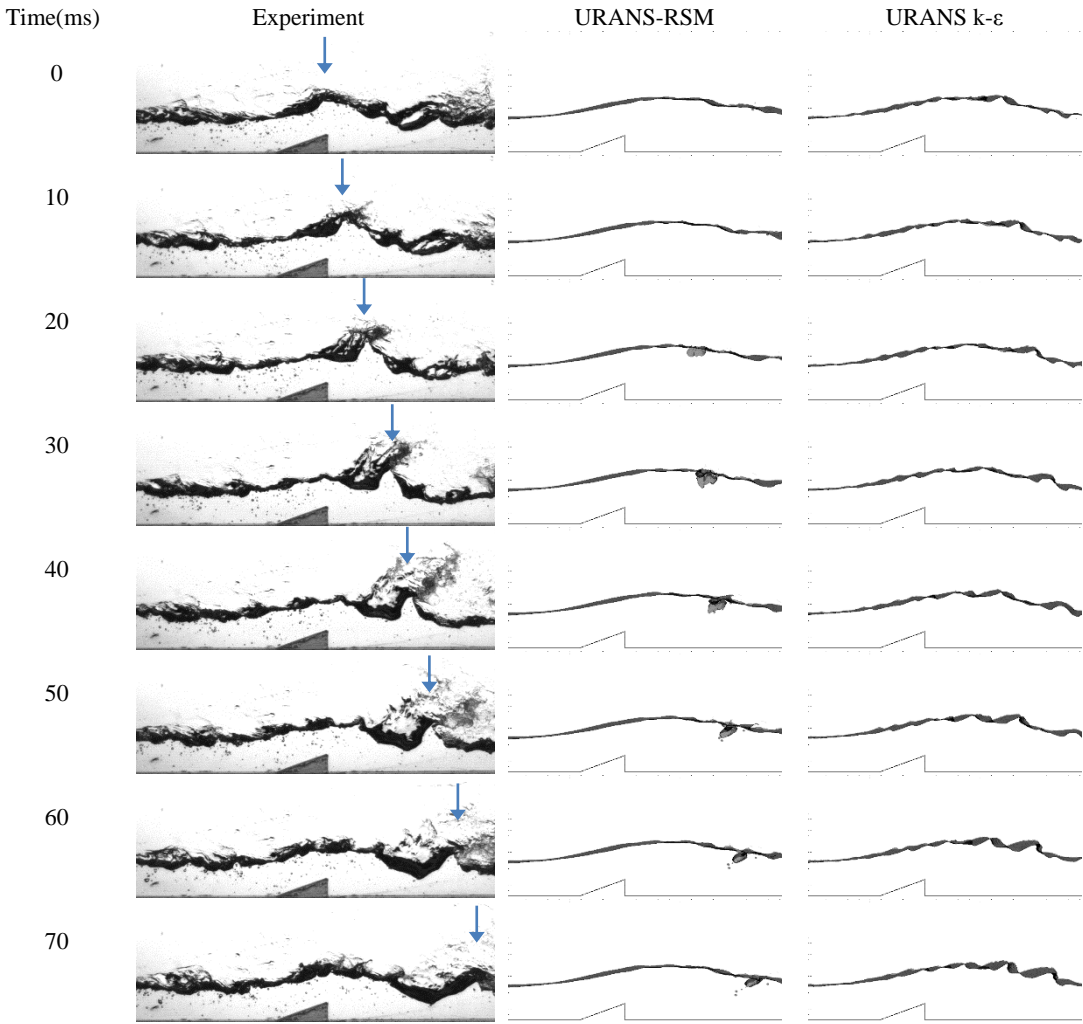
Figure 6-4 Liquid breakup comparison of experiment and CFD method of URANS-RSM and URANS k-ε

6.2.2 Droplet Volume to Size Distribution of CFD Approach Selection

The liquid droplet volume to size distribution per frame comparison of experiment, URANS-RSM, LES and DES k-w is shown in Figure 6-5. From this figure we could tell that the droplet volume to size distribution is different from case to case. Case experiment to URANS-RSM comparison is shown in Figure 6-5 (a), since the two phase liquid breakup performance of URANS is not ideal, little droplet volume to size distribution value is observed. The result of experiment to Large Eddy Simulation (LES) comparison is demonstrated in Figure 6-5 (b), the volume to size distribution curve is slight over predict for droplet size range from 1.5mm to 5mm, although the prediction curve is not exact match with experiment, but the peak volume to size distribution droplet size for LES is 1.86 mm which is more close to that from experiment of 1.04mm in diameter. The comparison result of experiment to Dethatched Eddy Simulation with RANS k-w (DES k-w) is demonstrated in Figure 6-5 (c), the volume to size distribution curve is also slightly over predict for droplet size range from 2mm to 5mm. the peak volume to size distribution droplet size for DES k-w is 2.53 mm when compare that value from experiment of 1.04mm and ability the prediction of peak volume size for DES k-w is less accurate than LES.

Since Detached eddy simulation (DES) is a modification of Reynolds-Averaged Navier-Stock (RANS) model with judgment criteria to enable Large Eddy Simulation (LES). The behavior of DES will range between LES and URANS and this phenomenon could be observed in both chapter 6.2.1 and chapter 6.2.2.The CFD approach comparison for Welch's frequency analysis will only focus on LES and DES.

(a)

(b)

(c)
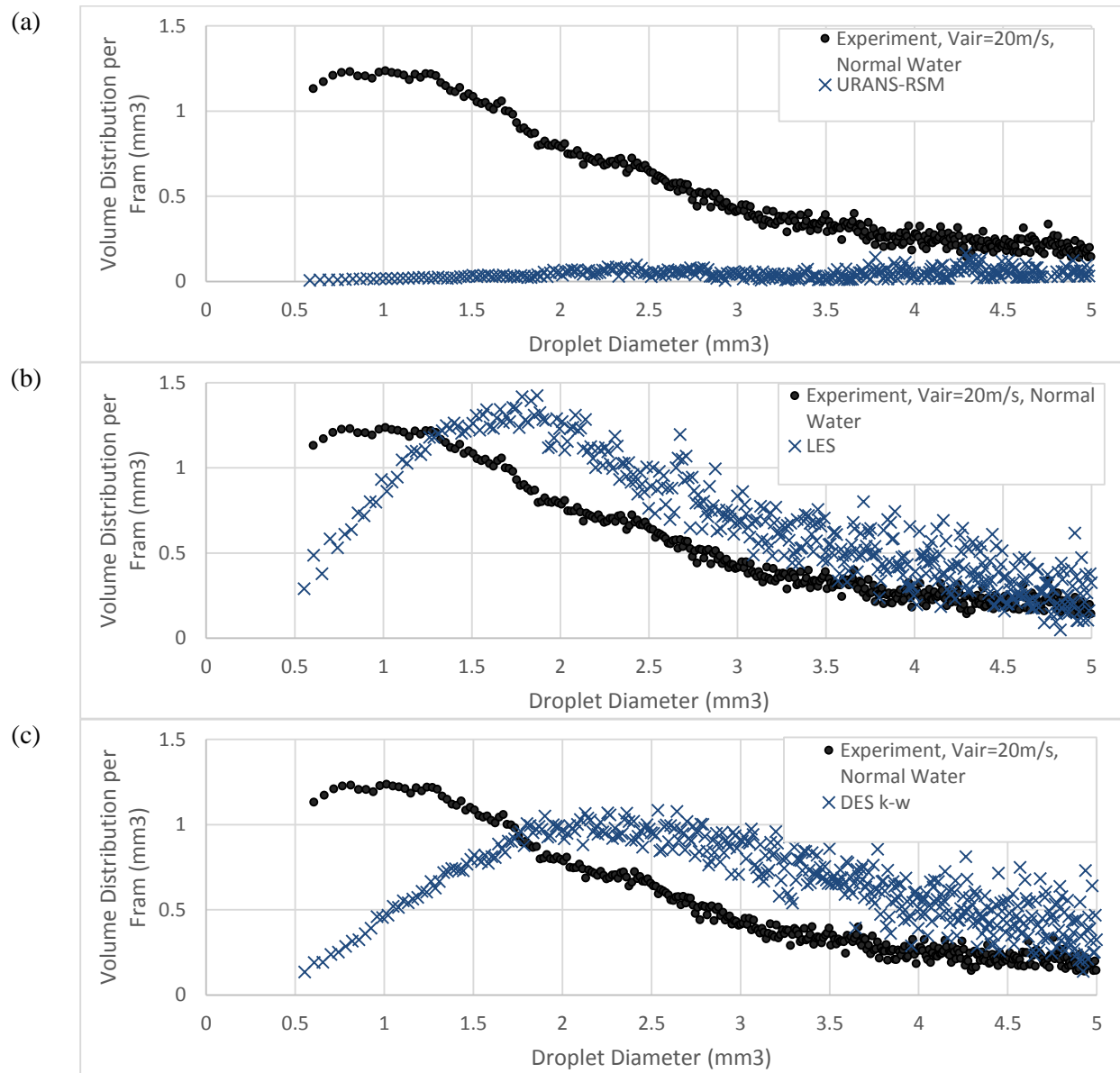
Figure 6-5 Liquid droplet volume to size distribution (mm³) per frame to equivalent diameter (mm) comparison of Experiment to (aURANS-RSM, (b) LES, (c) DES-k-w

6.2.3 Welch Analysis of CDF Approach Selection

The two-phase free surface vertical position history data is used for the Welch frequency analysis that is a variant of Fast Fourier Transform (FFT) with better noise reduction performance. The frequency data extraction location is above the ramp, and the wave position is fluctuating with time as shown in Figure 6-6. The wave location history of experiment, CFD method of LES and DES-kw is extracted from 2000 frames with a time interval of 1ms or a total time duration of 2 seconds as demonstrated in Figure 6-7.

The Welch analysis from experiment and CFD method of LES and DES-kw are shown in Figure 6-8. From the Welch analysis results the peak frequency from the experiment, LES and DES-kw are 15Hz, 14Hz and 21Hz, respectively. The magnitude of LES method is close to the experiment result throughout the frequency spectrum with an overall magnitude of 10.0% less than the experiment. However, the magnitude of DES-kw method is lower with an overall magnitude of 53.9% less than the experiment. In the summary of Welch method frequency analysis, LES has similar peak frequency and magnitude when to compare with experiment and simulation result from DES-kw method behaves higher fluctuating frequency and less amplitude when to compare to experiment result.
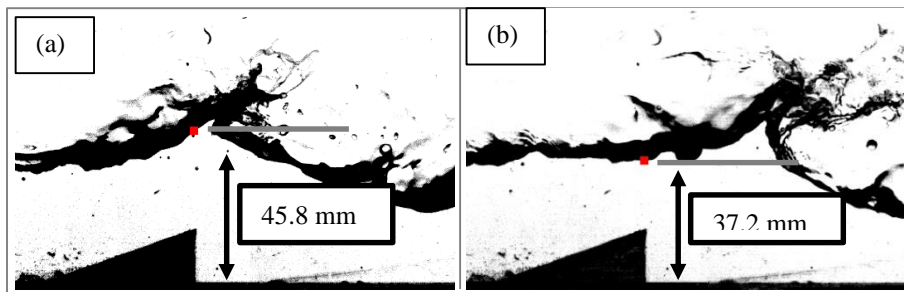
Figure 6-6 frequency history data extraction location from experiment.
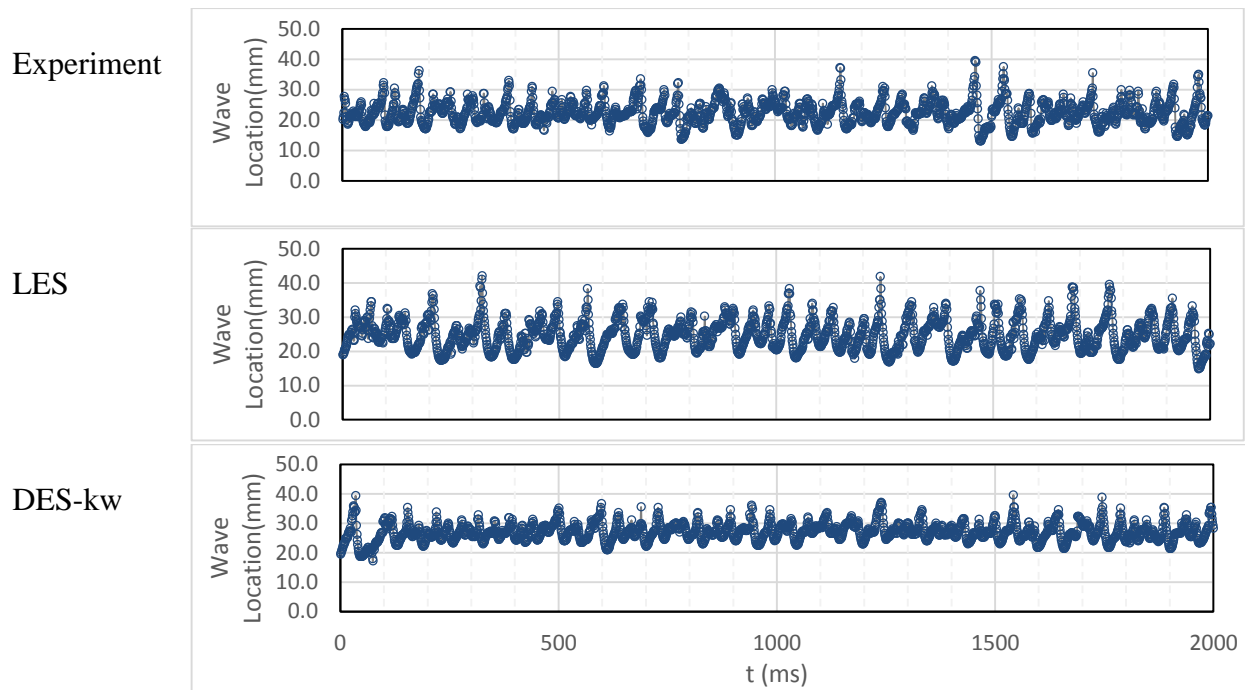
Figure 6-7 Wave location history of experiment, LES and DES-kw
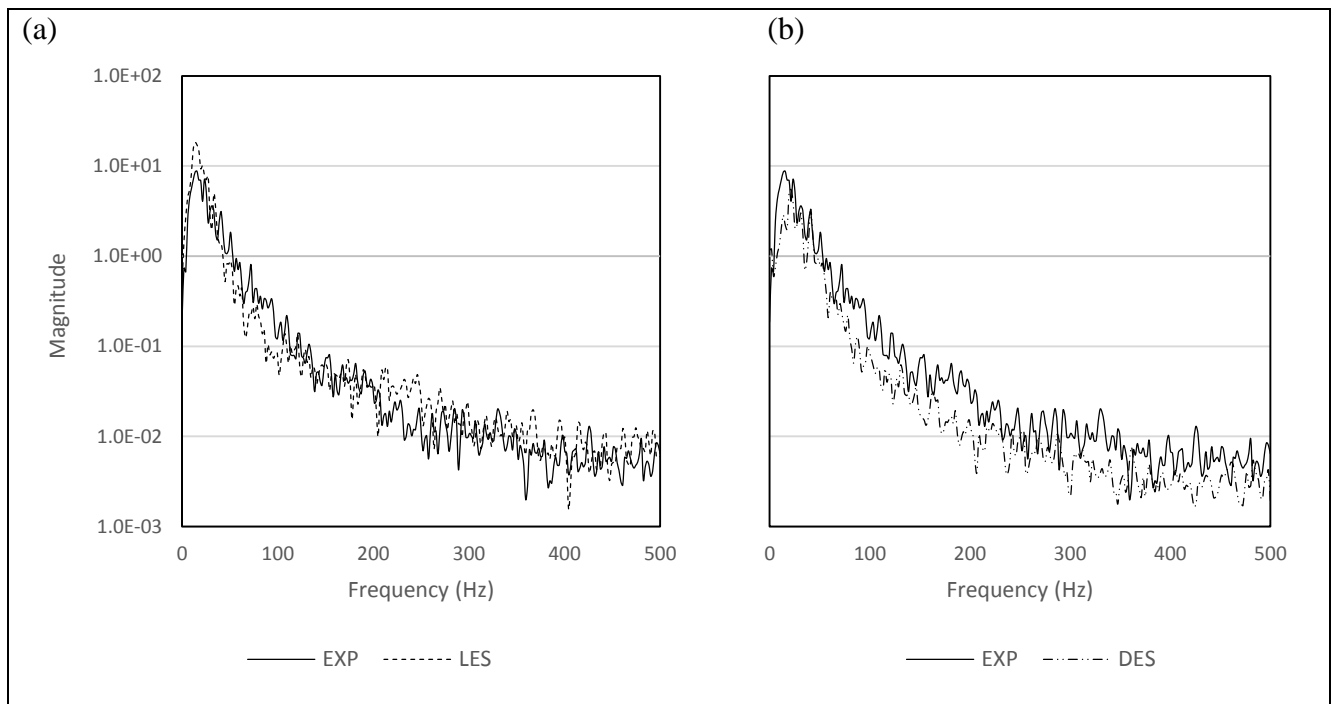
Figure 6-8 Welch frequency analysis of Experiment to LES and Experiment to DES-kw

Based on the performance of two-phase interaction (chapter 6.2.1), droplet volume to size distribution analysis (chapter 6.2.2) and Welch's frequency analysis (chapter 6.2.3), the result of LES approach stands out in two-phase flow simulation. LES will be select for this two phase liquid breakup study throughout the paper.

6.3   All CFD Case Image Comparison

The CFD simulation work cases setup are exactly the same as experiment discussed in chapter 5.2. All CFD simulation are carried out by Large Eddy Simulation (LES) approach and mesh setup are done by 16M cell mesh. The images cases are composed by the combination of three different air velocity and two different liquid surface tension setup. The air velocity setups are 20, 30 and 40m/s with water velocity setting is a constant of 0.67m/s. Liquid surface tension setup are 0.074 N/m and 0.040 N/s. All of the cases combination are listed in Table 6-4. The images from simulation cases are demonstrated from Figure 6-9 to Figure 6-14. A reference time step is set as initial time at this point (t=0 msec) when wave crest pass above ramp at the begging of each case. Breakup evolution time interval in the figures in this chapter are 10 msec.

Table 6-4 Simulation air velocity and liquid surface tension variable combination cases

	Liquid Surface Tension	
	Normal Water 0.074 N/m	Reduced Surface Tension 0.040 N/m
Vair = 20 m/s	Case 1 (Figure 6-9)	Case 2 (Figure 6-10)
Vair = 30 m/s	Case 3 (Figure 6-11)	Case 4 (Figure 6-12)
Vair = 40 m/s	Case 5 (Figure 6-13)	Case 6 (Figure 6-14)

The simulation cases are similar to cases from experiment work that the liquid behavior pattern is clear to distinguish from low to high air velocity setup, but less significant when compare cases

form different surface tension setup under same air velocity setting. The breakup processes evolution of simulation case 1 and 2 with Vair = 20 m/s are shown in Figure 6-9 and Figure 6-10. Compare with the other two higher air velocity setting, the liquid breakup activity of case 1 and case 2 are lowest, so does the droplet distribution the each frame. The difference between case 1 and case 2 is surface tension setup, however it is not easy to tell the difference from the figures without the support of image post processed tool.

The breakup processes evolution of simulation case 3 and 4 with Vair = 30 m/s are shown in Figure 6-11 and Figure 6-12, it could be observed that the free water surface is more fluctuate than case from Vair=20m/s. It is also clear that the liquid breakup activity is more active than cases from Vair=20m/s therefor more droplet could be observe in each frame. However, it is also hard to distinguish the liquid behavior difference between normal water and reduced surface tension.

The breakup processes evolution of simulation case 5 and 6 with Vair = 40 m/s are shown in Figure 6-13 and Figure 6-14. In this air velocity setup, the two-phase activity behaves as the most chaotic and active from those three air velocity setup. Due to more active liquid breakup activity, more droplets could be observed in the Vair=40m/s setup. Difference between normal water and reduced surface tension is still hard to determine as well.

Over all the liquid breakup activity is enhance with higher air velocity setup due to more kinetic energy in air. From theory, the liquid breakup will enhanced by reducing surface tension of liquid due to less liquid bounding force. However it is not easy to observe just from the figures. More analysis tool should apply to figure out the significance of the role of liquid surface tension.

T= 0 msec

T= 10 msec

T= 20 msec

T= 30 msec

T= 40 msec

T= 50 msec

T= 60 msec

Figure 6-9 Normal water surface tension simulation (0.074N/m) with V_{air}=20m/s (Time interval = 10 msec)

98

T= 0 msec

T= 10 msec

T= 20 msec

T= 30 msec

T= 40 msec
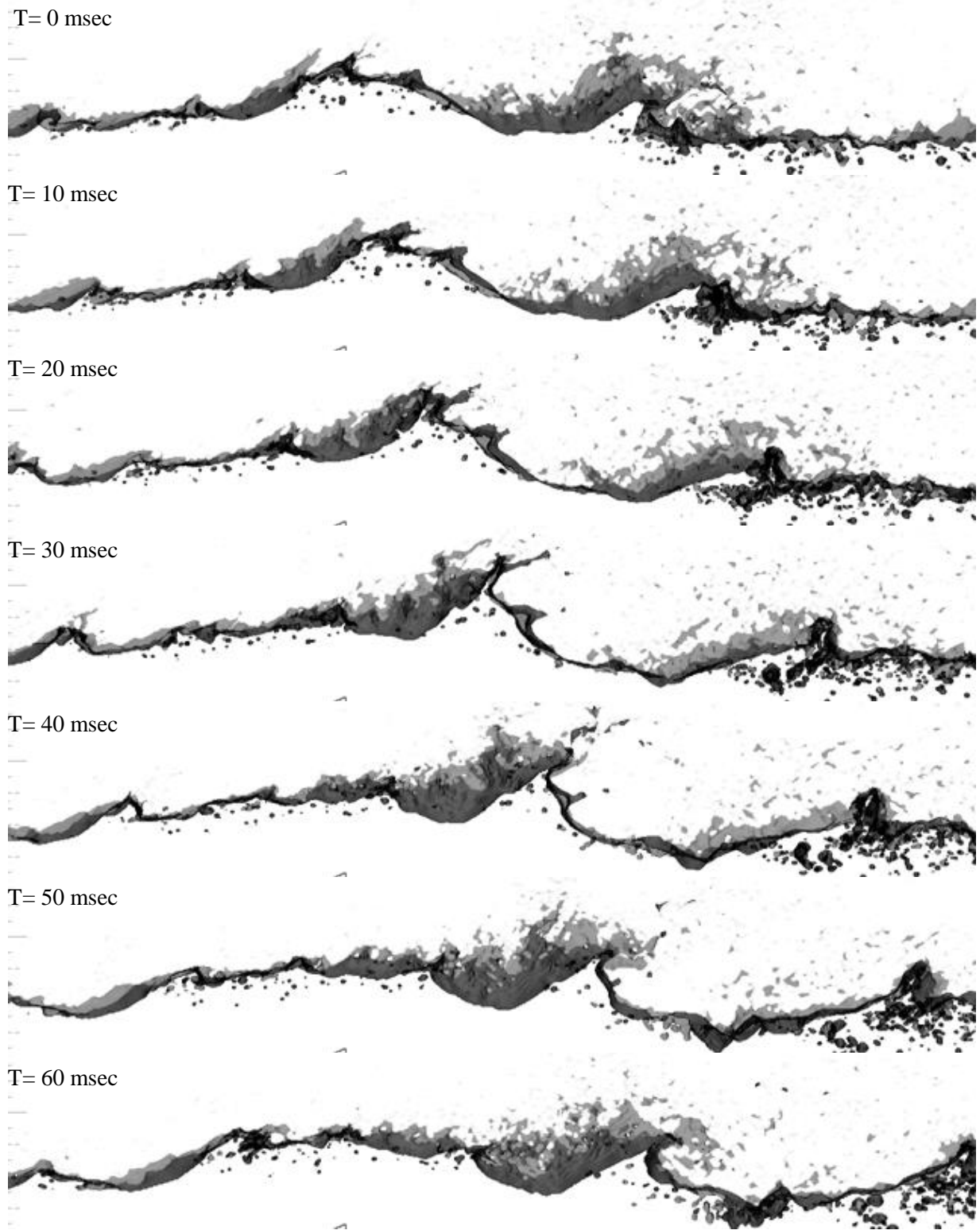
T= 50 msec

T= 60 msec

Figure 6-10 Reduced water surface tension Simulation (0.040N/m) with V_{air}=20m/s (Time interval = 10 msec)

99

T= 0 msec

T= 10 msec

T= 20 msec

T= 30 msec

T= 40 msec

T= 50 msec

T= 60 msec

Figure 6-11 Normal water surface tension simulation (0.074N/m) with V$_{air}$=30m/s (Time interval = 10 msec)

100

T= 0 msec

T= 10 msec

T= 20 msec
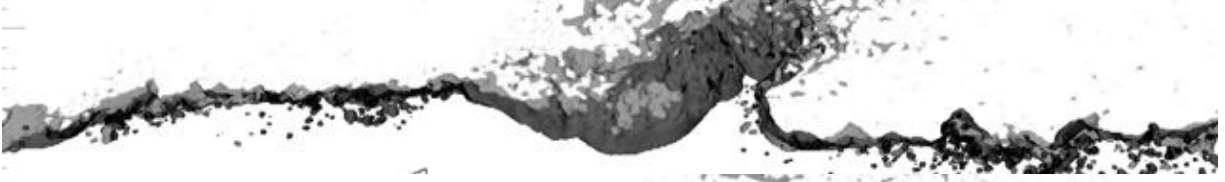
T= 30 msec

T= 40 msec

T= 50 msec

T= 60 msec

Figure 6-12 Reduced water surface tension Simulation (0.040N/m) with V$_{air}$=30m/s (Time interval = 10 msec)

101

T= 0 msec
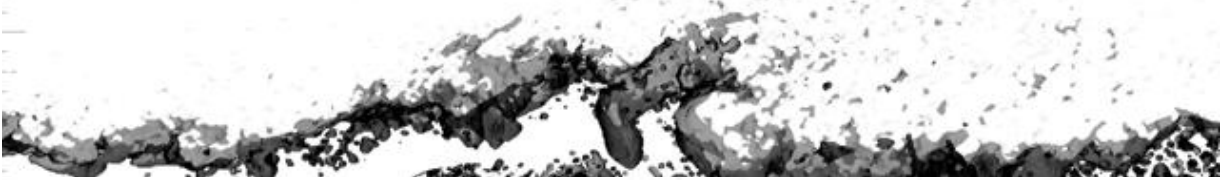
T= 10 msec

T= 20 msec

T= 30 msec

T= 40 msec

T= 50 msec

T= 60 msec

Figure 6-13 Normal water surface tension simulation (0.074N/m) with V$_{air}$=40m/s (Time interval = 10 msec)

102

T= 0 msec

T= 10 msec

T= 20 msec
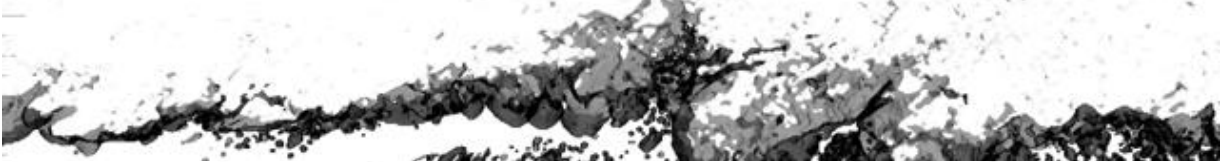
T= 30 msec

T= 40 msec

T= 50 msec

T= 60 msec

Figure 6-14 Reduced water surface tension Simulation (0.040N/m) with V$_{air}$=40m/s (Time interval = 10 msec)

103

6.4 All CFD Case Welch Frequency Analysis

The Welch's frequency analysis is a standardized comparison for flow channel experiment and simulation. Raw wave location history should be extract from simulation images, then the wave location history will serve as input of Welch frequency analysis and frequency spectrum as the output data for us to compare. More detail of Welch frequency analysis are discussed in chapter 3.5.3 and chapter 5.3.2.

6.4.1 Flow Channel Simulation Free Water Surface Location

The total image number of flow channel simulation in each case is 2,050 frames. Time interval between images to images is 1 msec and total length of time from simulation is 2.02 sec. Total Computational time for 6 cases is around 6 month based on 192 physical CPU core simulation jobs carried out in UW-Milwaukee High Performance Computing (UWM HPC) center.

The flow channel simulation raw wave location data are shown from Figure 6-15 to Figure 6-17 for cases of Vair = 20m/s to 40m/s. Data of normal water and reduced surface tension water are arranged in same figure from top to bottom. It could be observed that higher air velocity will result in lower the wave location and the reason result to this phenomenon is due to higher air velocity increase the breakup activity, more water breakup into droplet from main water body and resulting in decreasing water level. It could also be observed that for case of air velocity =20m/s, the location history data is not as chaotic as case from air velocity =40 m/s. the chaotic level from case of air velocity = 30m/s is between air velocity =20m/s and 40m/s.

The average location data of both normal water and reduce surface tension water are listed in Figure 6-18. This figure demonstrate that the location history data average of both normal water and reduced surface tension water for cases from Vair 20, 30 and 40m/s are 40.3 mm, 34.5 mm and 28.8 mm respectively. The reduced surface tension has averaged lower wave location value of 1.0%, 4.0% and 0.7% for the case of Vair 20m/s, Vair 30m/s and Vair 40m/s, respectively. Although it is not obvious to distinguish the difference between normal water and reduce surface tension water just from figures, but from the averaged value shown in Figure 6-18, we could observe that the reduced surface tension water shows the potential of active more liquid breakup. The result of wave location history from simulation show consistency with the result from flow channel experiment.
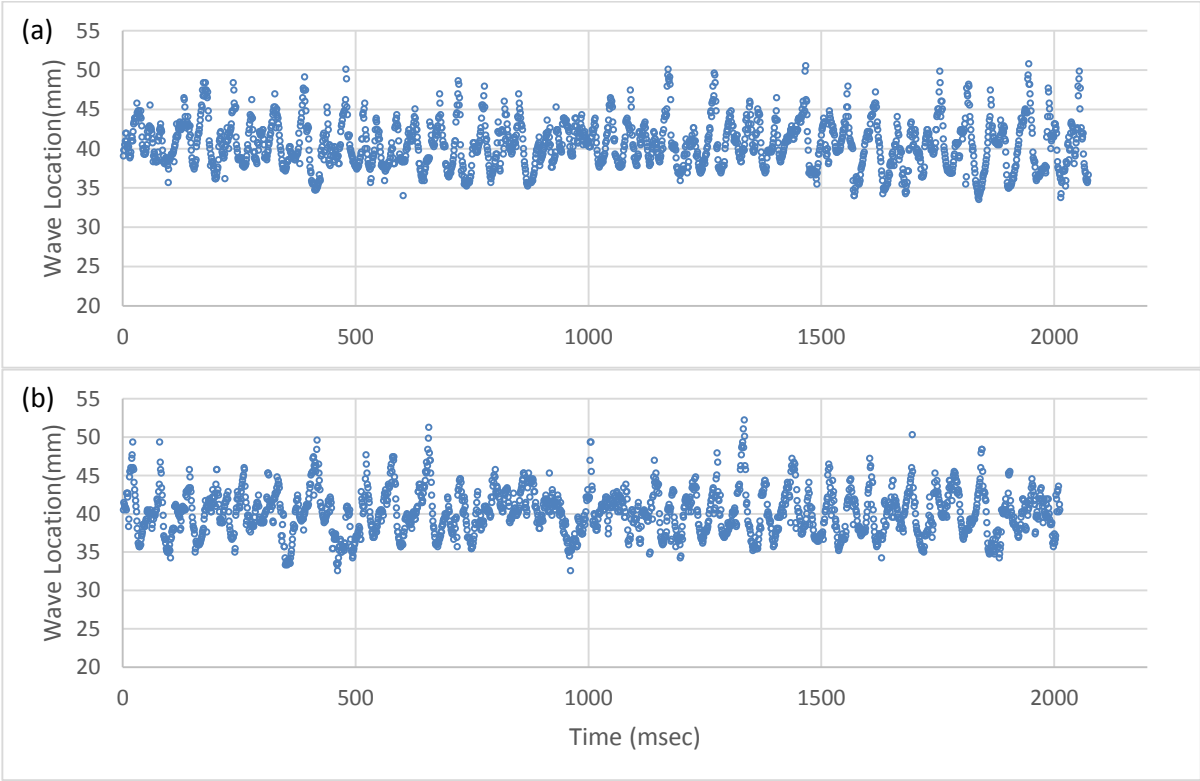
Figure 6-15 Simulation free water surface location at ramp with Vair=20m/s for (a) Normal water (b) Water of reduced surface tension

105
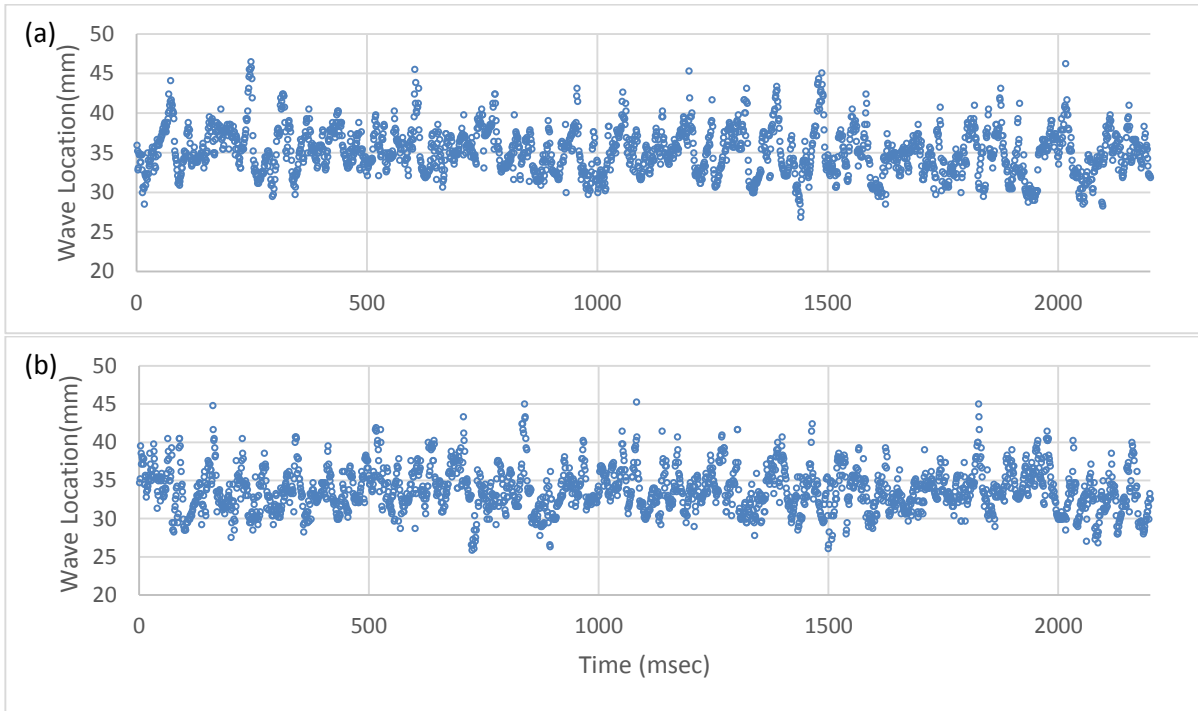
Figure 6-16 Simulation free water surface location at ramp with Vair=30m/s for (a) Normal water (b) Water of reduced surface tension
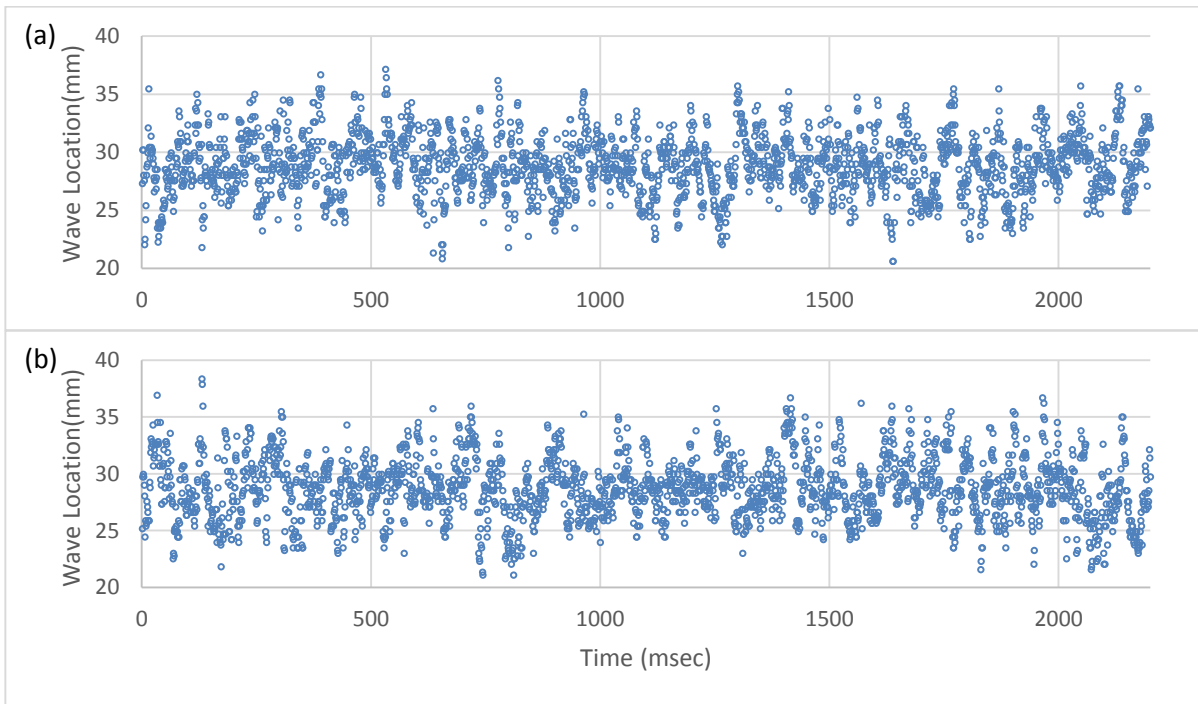
Figure 6-17 Simulation free water surface location at ramp with Vair=40m/s for (a) Normal water (b) Water of reduced surface tension

106
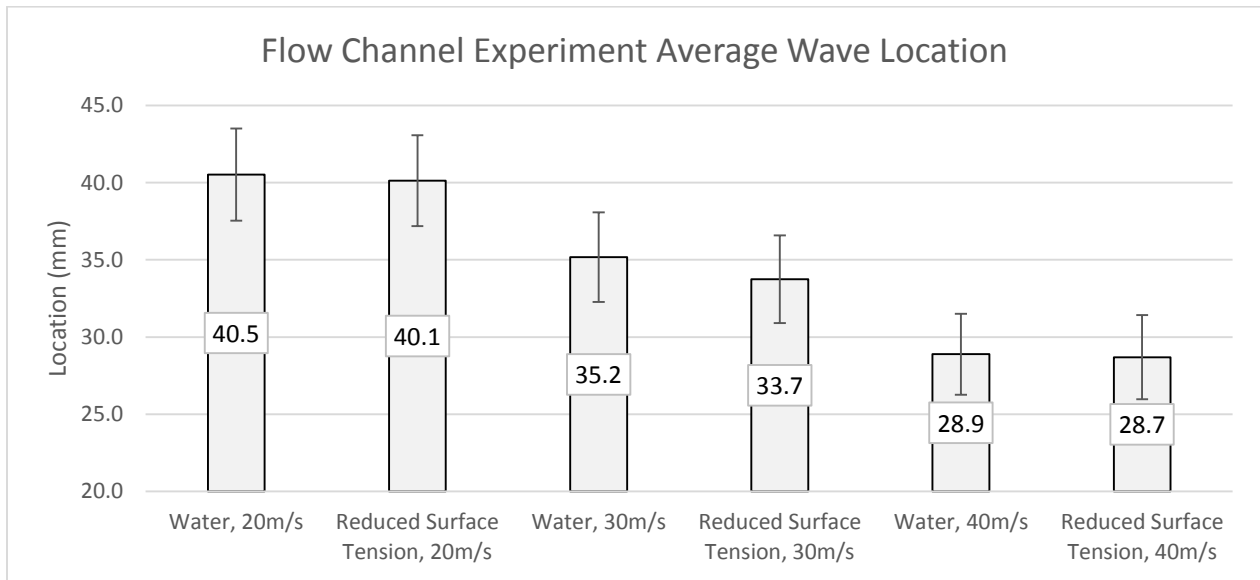
Figure 6-18 Flow channel CFD simulation average wave location at ramp for all 6 cases in flow channel experiment

6.4.2 Flow Channel Simulation Welch Frequency Analysis

The overview Welch frequency analysis of two-phase free surface wave location from flow channel CFD simulation are shown in Figure 6-19. It is clear that for frequency region higher than 250 Hz, higher air velocity result in higher magnitude in this region for both normal water and reduced surface tension case, for instance the magnitude of Vair = 40 m/s has value about one order higher than that from Vair=20m/s. The peak frequency for normal water cases are 19.5Hz, 13.6Hz and 21.4Hz for Vair = 20m/s, 30 m/s and 40m/s, respectively. The peak frequency for reduced water surface tension cases are 15.5Hz, 12.7Hz and 17.5Hz for Vair = 20m/s, 30 m/s and 40m/s, respectively. Similar to cases from flow channel experiment, there is no significant difference between cases from normal surface tension to reduced surface tension, the peak frequency for all cases are listed in Table 6-5. The phenomenon could be explained by Froude number (Fr) which is inverse proportional to square root of gravitational constant and the depth of

liquid, since the depth of the liquid in the simulation is a constant value of 30 mm, the Froude

number should be same from cases to cases. More Froude number discussion also documented in

chapter 5.3.2. Full Welch frequency analysis comparison for both experiment and simulation will

discussed in chapter 7.2.
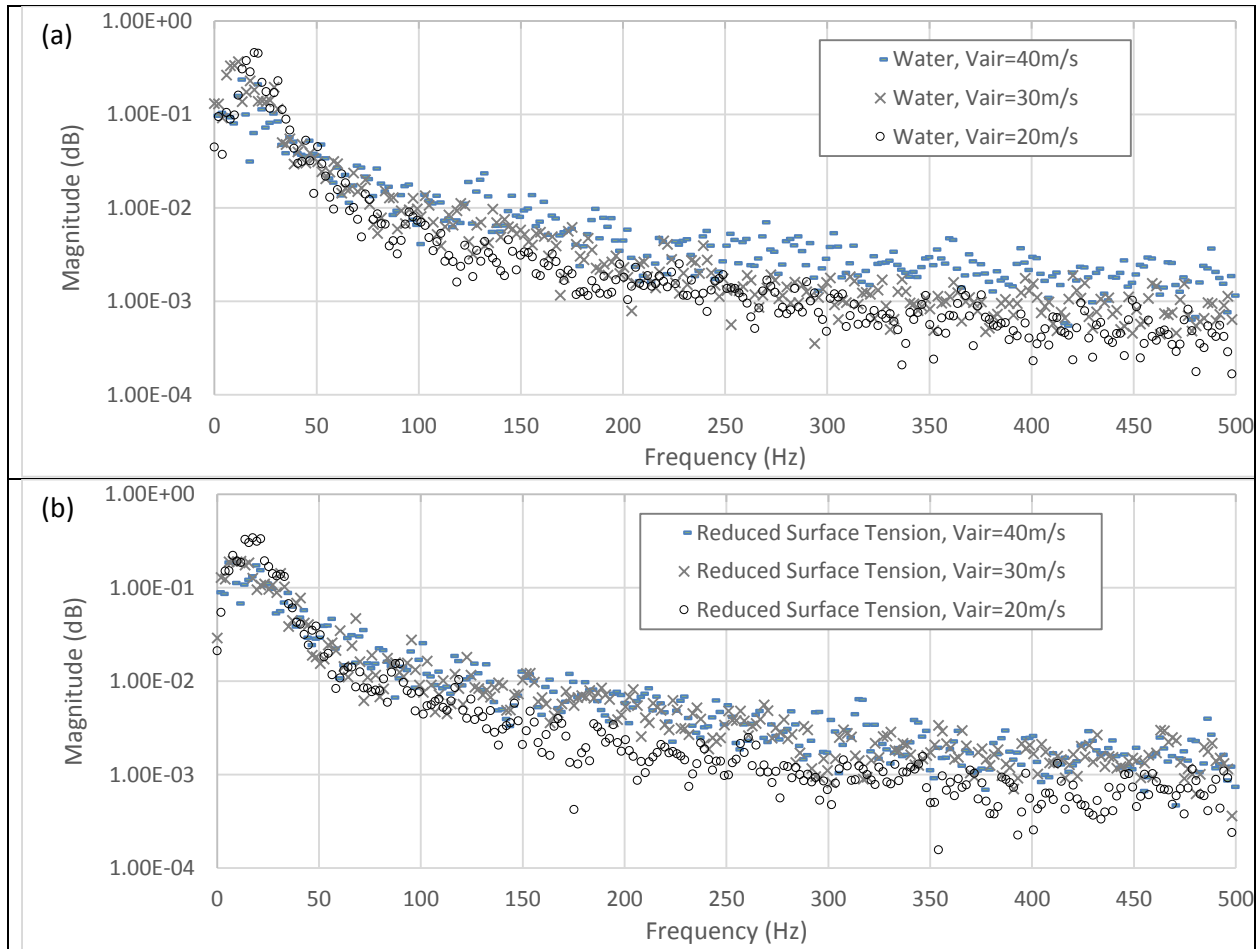
Figure 6-19 Flow channel simulation Welch frequency analysis comparison between Vair = 40 m/s, 30 m/s and 20 m/s of (a) Normal Water (b) Reduced surface tension

Table 6-5 Peak frequency for all simulation cases (Hz)

	Vair=20m/s	Vair=30m/s	Vair=40m/s
Normal Water	19.5	13.6	21.4
Reduced Surface Tension	15.5	12.7	17.5

6.5 CFD Simulation Droplet Volume to Size Distribution

The flow channel simulation droplet volume to size distribution comparison between normal water and reduced surface tension water are shown in Figure 6-20. The data was extract by MatLab image process code developed in UW-Milwaukee wind tunnel lab. The detailed code process work flow is discussed in chapter 3.5.2. The range of the particle size are starting from 0.6mm to 5.0mm. Same as experiment droplet size process procedure, the minimum size of droplet could be recognize by simulation images resolution is 0.24mm per pixel. In terms of data accuracy, for any droplet equivalent diameter smaller than 0.6mm are filter out. In this figure, volume to size distribution per frame from six cases are the averaged values from 2,050 frames of LES simulation output images with time interval of 1 msec. The volume unit is marked in mm^3. Based on the air velocity setting, the 6 cases are separated into three velocity groups of group (a) air velocity = 40m/s, group (b) air velocity = 30m/s and group (c) air velocity = 20m/s as demonstrated in the figure. It could be observed that cases from three different velocity group setting is clear to distinguish, the value of droplet volume to size distribution curve is higher from higher air velocity setting, and the distribution value is becomes lower when air velocity reduces. However the difference between different surface tension settings are not easy to distinguish for all cases. Overall, the LES simulation result demonstrate the clear trend of droplet distribution with air velocity which is similar to the result from experiment, but the difference between normal water and reduced surface tension is not clear to observed. The reason of unclear result from different surface tension setup might due to insufficient mesh density. Since the simulation setup of this study is already pushing the campus High Performance Computation (HPC) resource of University

of Wisconsin-Milwaukee to the limit, more study could be carried out in the future when computing resource improve to sufficient level to handle finer mesh setup.
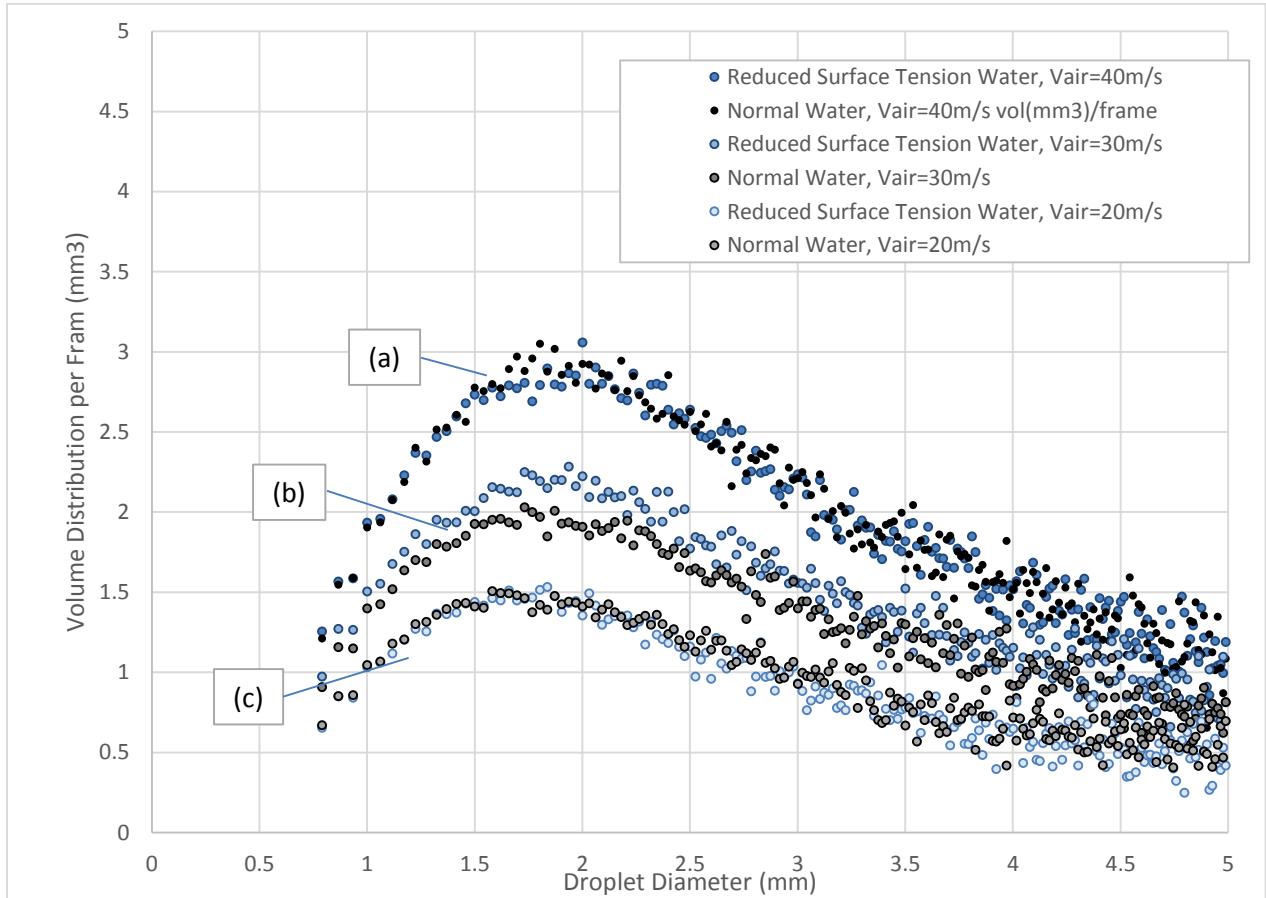
Figure 6-20 Flow channel simulation droplet volume to size distribution comparison between normal water and reduced surface tension water for cases (a) Vair=40m/s, (b) Vair=30m/s and (c) Vair=20m/s.

6.6   CFD Approach Conclusions

From mesh independent study, 16M cell setup is selected due to balance of accuracy and computational time. A comparison of two-phase flow liquid breakup phenomenon between experiment, LES, DES-kw, URANS-RSM and URANS-k-w method are carried out in this study. From image comparison, the result of LES approach provides similarity to the result of experiment

regarding wave amplitude and liquid breakup level, while the DES-kw shows less amplitude of wave and less active liquid breakup phenomenon when compared to the experiment. While URANS predict no liquid breakup phenomenon. LES is selected due to best pridiction performance of two-phase flow.

From averaged wave location history data we could conclude that the difference between different air velocity is clear, higher the air velocity will lower the averaged wave location. This is due to the water has more volume turn into liquid droplet carrying by moving air for higher air velocity case. However it is not clear to observe the difference bwteen normal water and reduced surface tension water.

From the result of Welch's frequency analysis, we also observe the difference from air velocity setting in higher frequency region. When talk about the peak frequency, all cases has similar value ranging between 15Hz to 20Hz. The result could be explained by Froude number (Fr) which is inverse proportional to square root of gravitational constant and the depth of liquid, since the depth of the liquid in the simulation is a constant. Fr number is same for all cases and lead to similar peak frequency

From the result of droplet volume to size distribution we could conclude that the distribution curve is clear to distinguish for cases from different air velocity, however it is hard to distinguish for cases from normal water to reduced surface tension water.

Overall, the 16M LES simulation could predict cases from different air velocity, however the mesh is not fine enough to capture subtle difference between different surface tension setup.

7 Flow Channel Experiment and Simulation Comparison and Discussion

The comparison work of flow channel experiment and simulation will be discussed in this chapter. The performance of two-phase flow prediction from CFD could studied by compare the result from experiment and CFD simulation. The comparison work include three parts, the first part of comparison is superimpose image comparison which provide a time averaged flow pattern for all cases and we will be able to compare the difference between cases to cases from time averaged flow contour. The second part of comparison work is Welch's analysis comparison, in this section wave frequency performance of CFD could be studied. The third part is droplet volume to size distribution comparison, in this part the droplet volume and size distribution could be directly compared with the result form experiment.

7.1 Superimpose Image Comparison

In this sub-chapter of 7.1, we will discuss the superimpose image comparison in three parts. The first part will cover overview of superimpose image comparison for all cases of experiment, simulation, normal water and reduced surface tension water. The second part discuss the comparison work between experiment and simulation. The third part discussion will be focus on the comparison of normal water to reduced surface tension water.

7.1.1   Superimpose Image Comparison Overview

The superimpose image comparison of flow channel experiment and simulation are discussed in this chapter, the image superimpose process work are documented in chapter 3.5.4. The total overlapping images from experiment and simulation are 6,540 and 2,000 frames respectively. A featured superimpose image illustration are shown in Figure 7-1. A bubble recirculation region are point out in part (a) in Figure 7-1, it could be observed when air velocity increases more bubble will be engulf into the recalculation region after the ramp as demonstrated. The smooth transition region in part (b) of the figure could be considered as the droplet distribution region, the darker the color is means the higher chance of liquid droplet could be observed. The contour map of superimposed image of Figure 7-1 is demonstrated in Figure 7-2. In this figure we could observe the outer boundary of contour lines and exam the difference between cases. The recirculation region could also be observed if there is one in the case.

The superimposed image of normal water and contour map are demonstrated in Figure 7-3 and Figure 7-4. For the case of air velocity = 20m/s cases, both experiment and simulation shows similar superimpose result, no bubble recirculation was observed and has similar liquid droplet distribution region and the outline of contour map. For the case of air velocity = 30 m/s, no bubble recirculation was observed in both experiment and simulation, however the droplet distribution region are larger for experiment case than simulation, the droplet distribution has smother transition from water surface to air and has wider distribution range after ramp in experiment. It could also be observed from contour map that the outline of experiment is larger than simulation. This means the droplet is carried by air and stays in the air further compare to result of simulation.

In the case of air velocity = 40 m/s, bubble recirculation region could be observed in both experiment and simulation, however the result from simulation shows much more bubble recirculation compare to experiment. The droplet distribution region in experiment shows more smooth transition from water to air and also has wider range compare to the result from simulation. It could also been observed from contour map that experiment has wider range of droplet distribution region from outline. From contour map the overestimate recirculation region is also been observed.
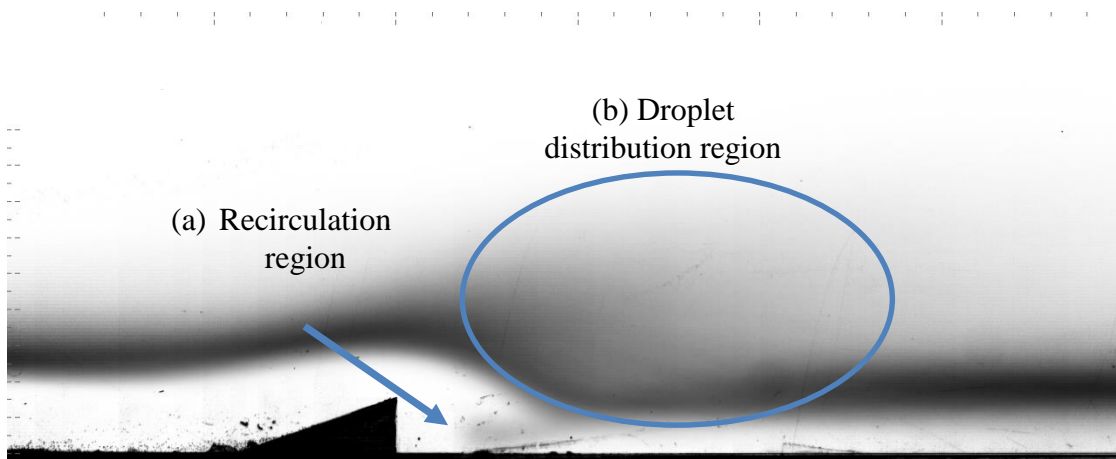
Figure 7-1 Featured location of superimpose image.
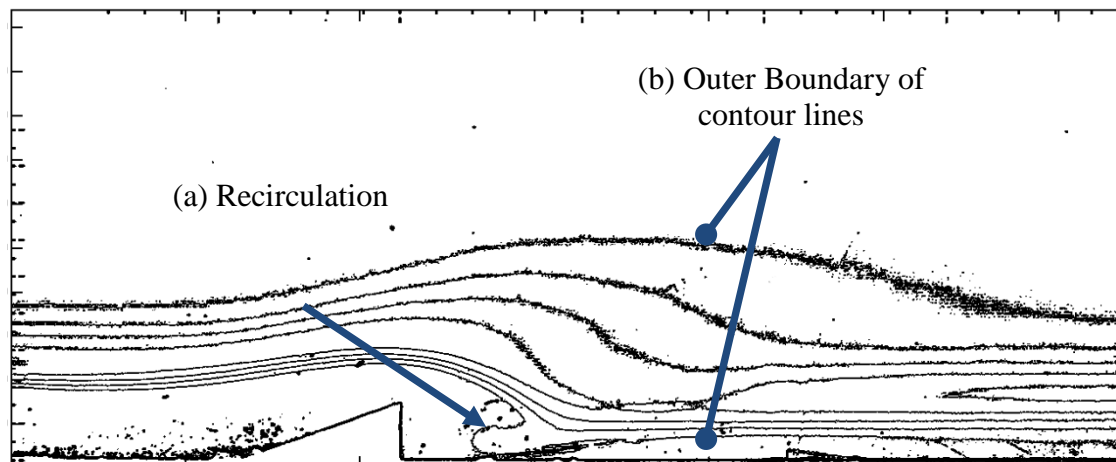
Figure 7-2 Contour map of superimposed image of Figure 7-1.

Normal Water	Experiment	Simulation
Vair=20m/s		
Vair=30m/s		
Vair=40m/s		
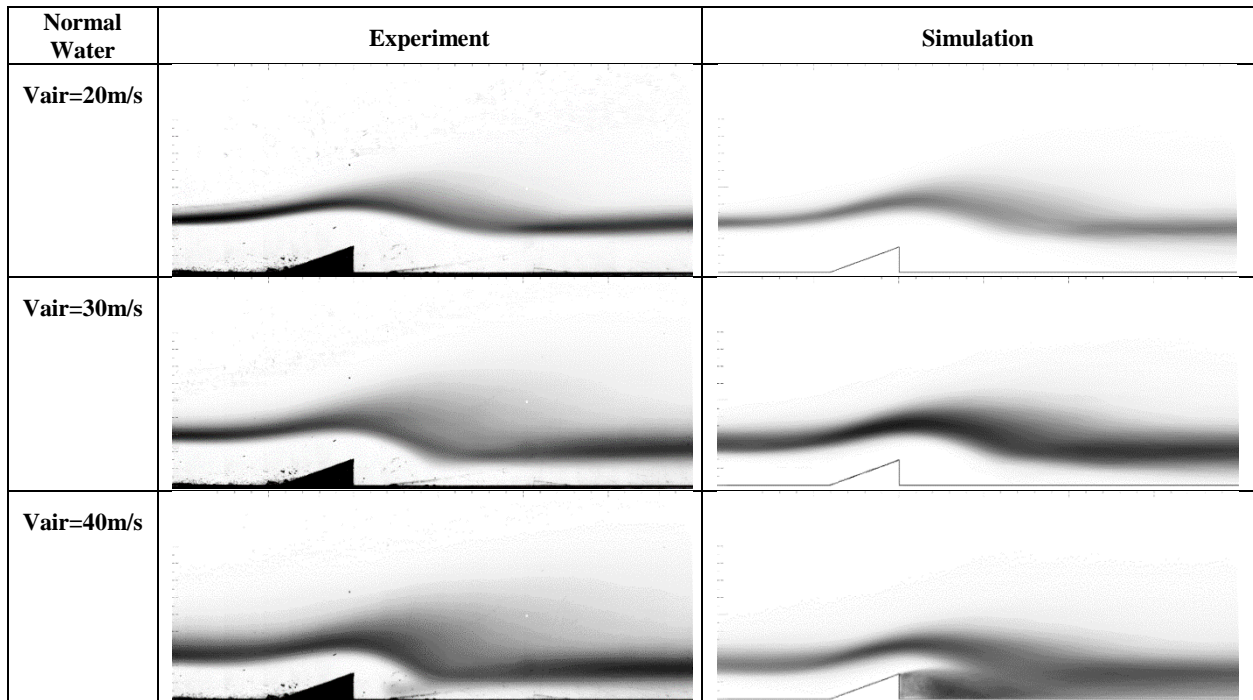
Figure 7-3 Superimpose images of normal water (σ = 0.074 N/m) cases for experiment (left) and Simulation (right) for air velocity Vair = 20m/s, Vair = 30m/s and Vair = 40m/s

Normal Water	Experiment	Simulation
Vair=20m/s		
Vair=30m/s		
Vair=40m/s		
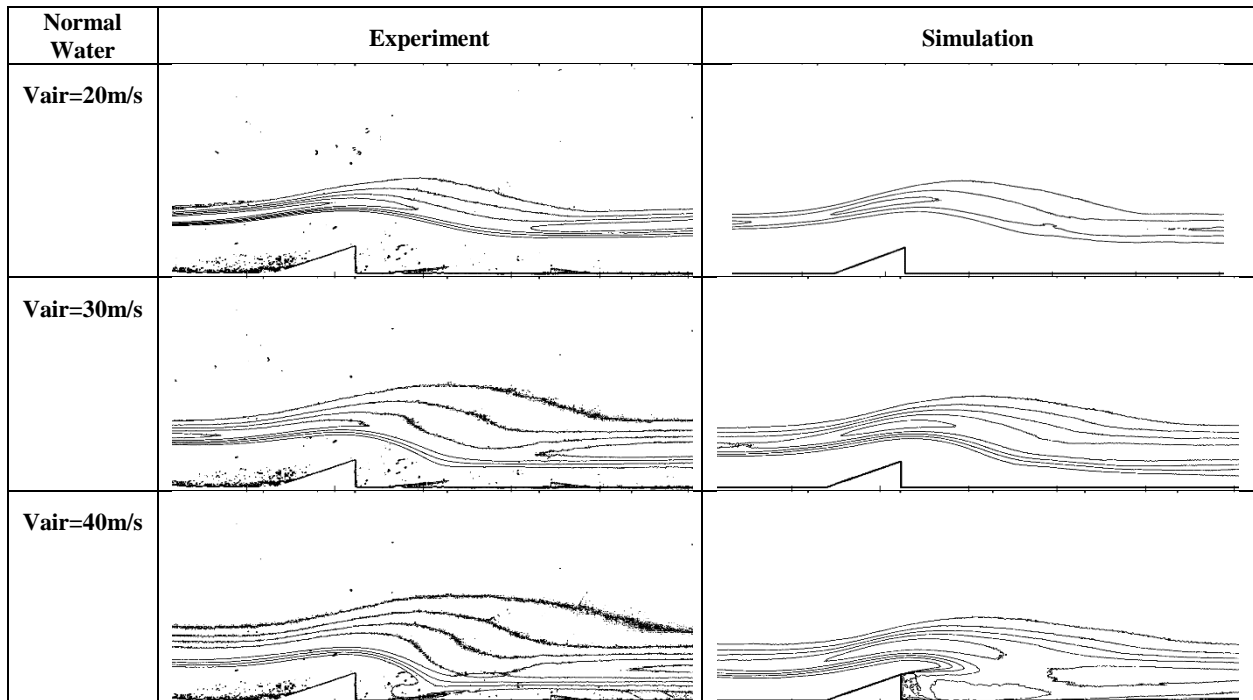
Figure 7-4 Contour map of normal water (σ = 0.074 N/m) cases from Figure 7-3

The superimposed image of reduced surface tension water and contour map are demonstrated in Figure 7-5 and Figure 7-6. For the case of air velocity = 20m/s cases, both experiment and simulation shows similar result in superimpose image, no bubble recirculation was observed and both case show similar liquid droplet distribution region and so does the outline of contour map. In the case of air velocity = 30 m/s, no bubble recirculation was observed in both experiment and simulation as well, however the droplet distribution region are larger from experiment case than simulation, it is also clear that in experiment case the droplet distribution has smother transition from water surface to air and has wider distribution range after ramp. The result could also be observed from contour map that the outline of experiment is larger than simulation. Same as the normal water group case that the droplet is carried by air and move further after the ramp compare to result from simulation. For the case of air velocity = 40 m/s, bubble recirculation region could be observed in both experiment and simulation, however the result from simulation shows over prediction of bubble recirculation compare to experiment. The droplet distribution region in experiment shows more smooth transition from water to air and also occupy wider range compare to the result from simulation. It could also been observed in contour map that the droplet distribution region in experiment has wider range from outline. From contour map the over predict recirculation region is also been observed.

Reduced Surface Tension	Experiment	Simulaiton
Vair=20m/s		
wVair=30m/s		
Vair=40m/s		
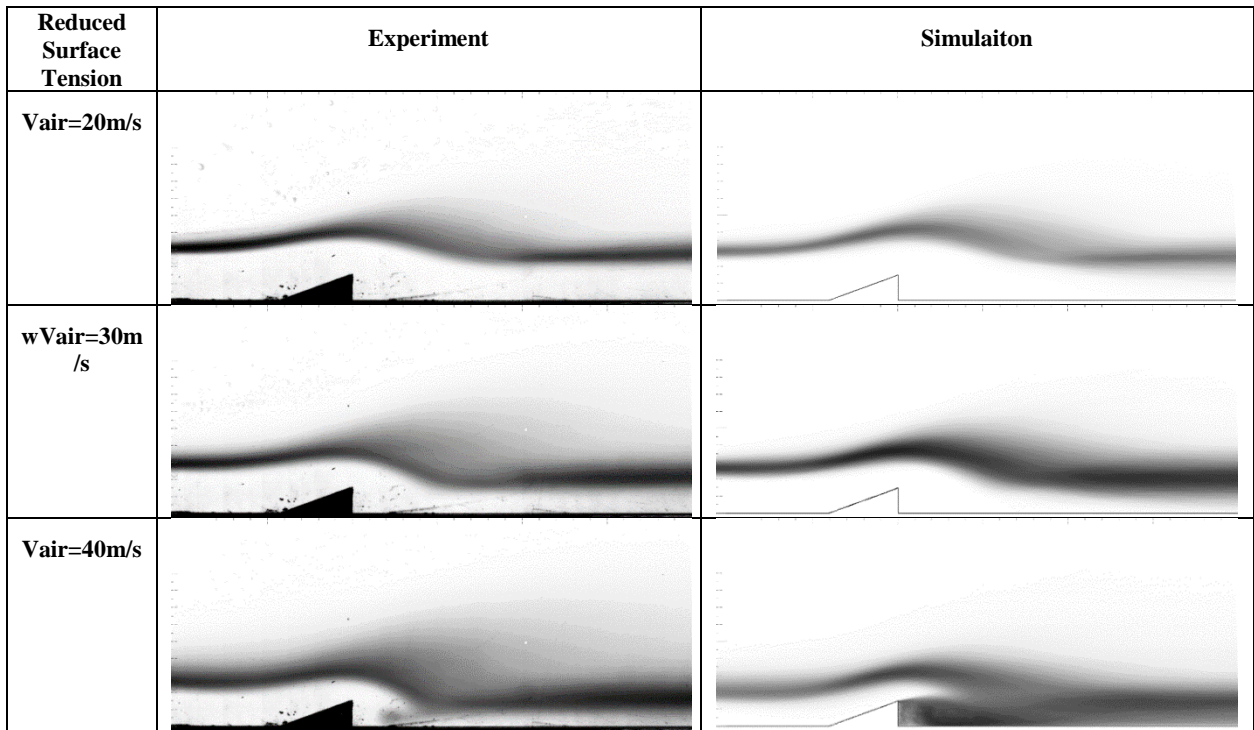
Figure 7-5 Superimpose images of reduced surface tension water (σ = 0.040 N/m) cases for experiment (left) and Simulation (right) for air velocity Vair = 20m/s, Vair = 30m/s and Vair = 40m/s

Reduced Surface Tension	Experiment	Simulation
Vair=20m/s		
Vair=30m/s		
Vair=40m/s		
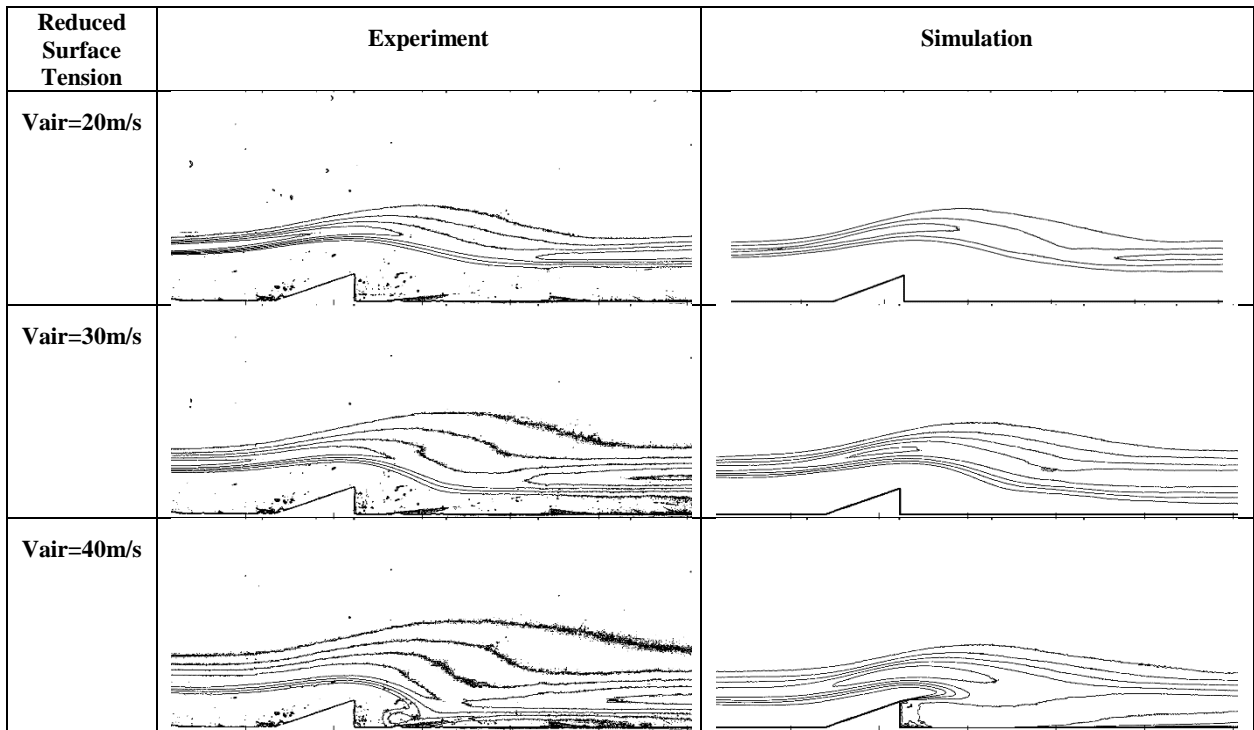
Figure 7-6 Contour map of reduced surface tension water (σ = 0.040 N/m) cases from Figure 7-5

117

7.1.2 Superimpose Image of Experiment and Simulation Overlap Comparison

The contour map outline comparison of experiment and simulation are shown in Figure 7-7. The contour map outline of experiment and simulation are overlap for the purpose of readiness comparison. The results of experiment are marked in black and the results of simulation are marked in green. For the air velocity = 20m/s setup, it is clear that the result from simulation (green) and experiment (black) are similar for both normal water and reduced surface tension water setup. In the cases of air velocity = 30m/s, the outline of experiment (black) are larger than simulation (green), but the overall outline are similar for both normal water and reduced surface tension water cases. When air velocity increased to 40m/s, the outline shows difference between experiment (black) and simulation (green), the upper outline cover wider range of area from experiment result (black) than simulation (green) for both normal water and reduced surface tension water cases.
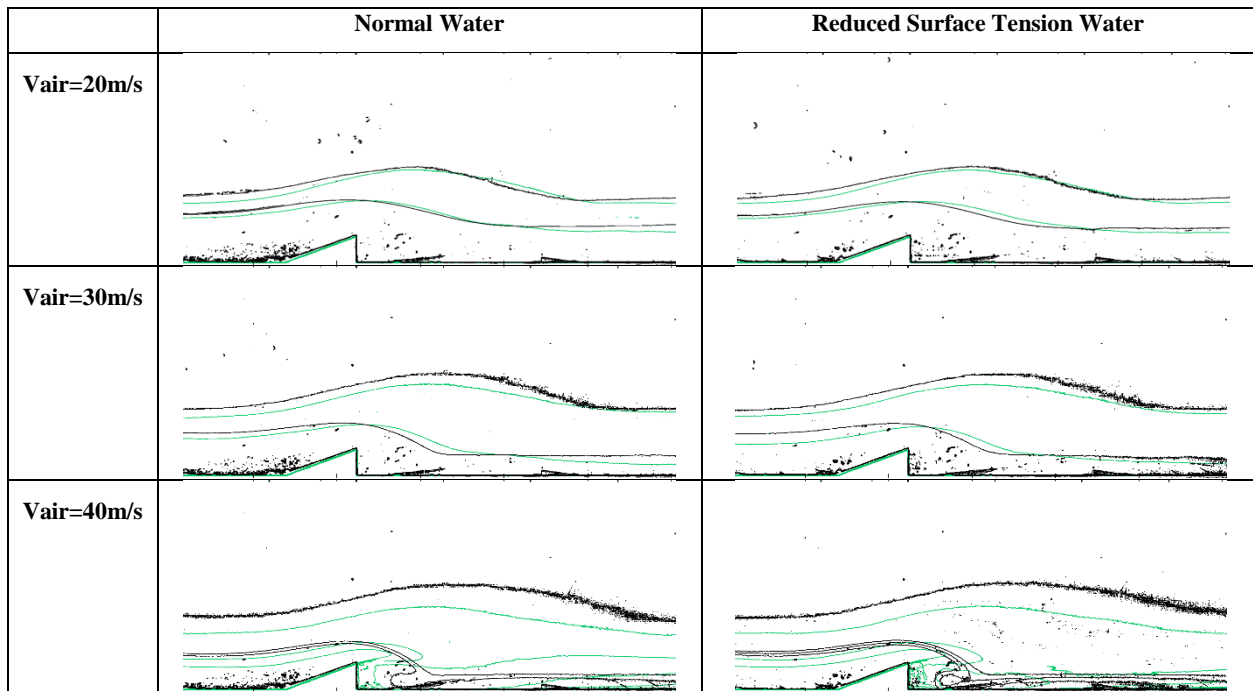
Figure 7-7 Contour map outline comparison of Experiment (marked with black line) and Simulation (marked with green line)

7.1.3 Superimpose Image of Normal Water to Reduced Surface Tension Water Overlap Comparison

The contour map outline comparison of normal water and reduced surface tension water are listed in Figure 7-8. The contour map outline of normal water and reduced surface tension water are overlap for the purpose of readiness comparison. The result of normal water are marked in black and reduced surface tension water are marked in green. In the group of experiment cases, it is clear that the reduced surface tension cases (green) has greater outline area compare to normal water cases (black) for all air velocity setup. In the Vair=40m/s case, the bubble recirculation region of reduced surface tension water (green) are also greater than normal water (black). In the group of simulation cases, the difference between normal water and reduced surface tension water is not clear. The prediction ability of simulation for different surface tension is not significant in our case.

	Experiment	CFD Simulation
Vair=20m/s		
Vair=30m/s		
Vair=40m/s		
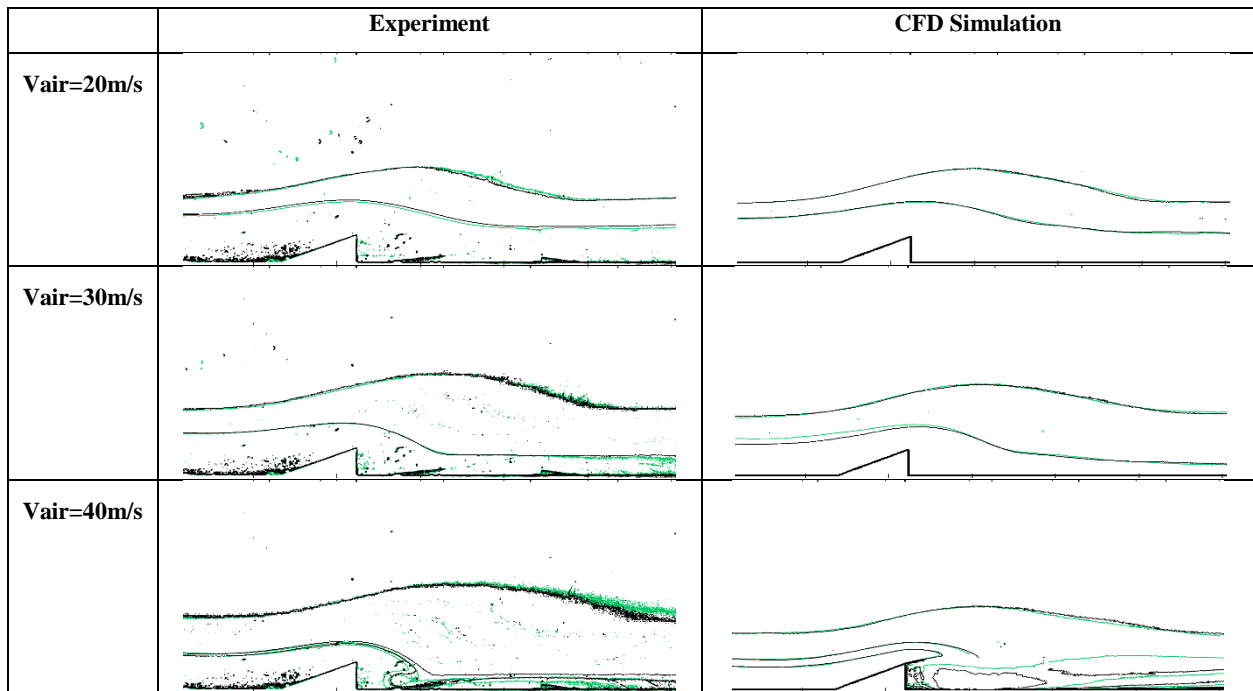
Figure 7-8 Contour map outline comparison of normal water (marked with black line) and reduced surface tension water (marked with green line)

7.2   Flow Channel Welch Analysis Comparison

The data input of Welch's analysis has frequency of 1,000 Hz which is record at the water surface location above of the ramp position. Data length of experiment and simulation are 6,540 msec and 2,000 msec respectively. The Welch's frequency analysis result comparison for all flow channel experiment and simulation cases are demonstrated in Figure 7-9 and Figure 7-10. Each figure contains result of normal water group at top and reduced surface tension water group at bottom.

It is observed that the magnitude of higher air velocity has greater value than that from lower air velocity cases within higher frequency region from 250 Hz to 500 Hz for all experiment and simulation cases. The reason of the result is due to higher air velocity induced higher turbulence level causing more fluctuating water surface and lead to higher magnitude in high frequency region. It is also observed that the result from both experiment and simulation, for the magnitude of the cases from Vair=40m/s is about one order greater than that from Vair =20m/s cases.

It is also observed that the peak frequency are similar for all cases and ranging at lower frequency region of 13Hz~20Hz, the peak frequency data for all cases from experiment and simulation are listed in Table 7-1. This could be explained by Froude number (Fr) which is defined as fluid velocity over square root of multiplication of gravitational constant and liquid depth. Since all cases has same setup of water depth of 30mm at entrance, the peak frequency will be similar for all cases. The result also shows that CFD simulation is also trustable in terms of wave frequency for all cases.
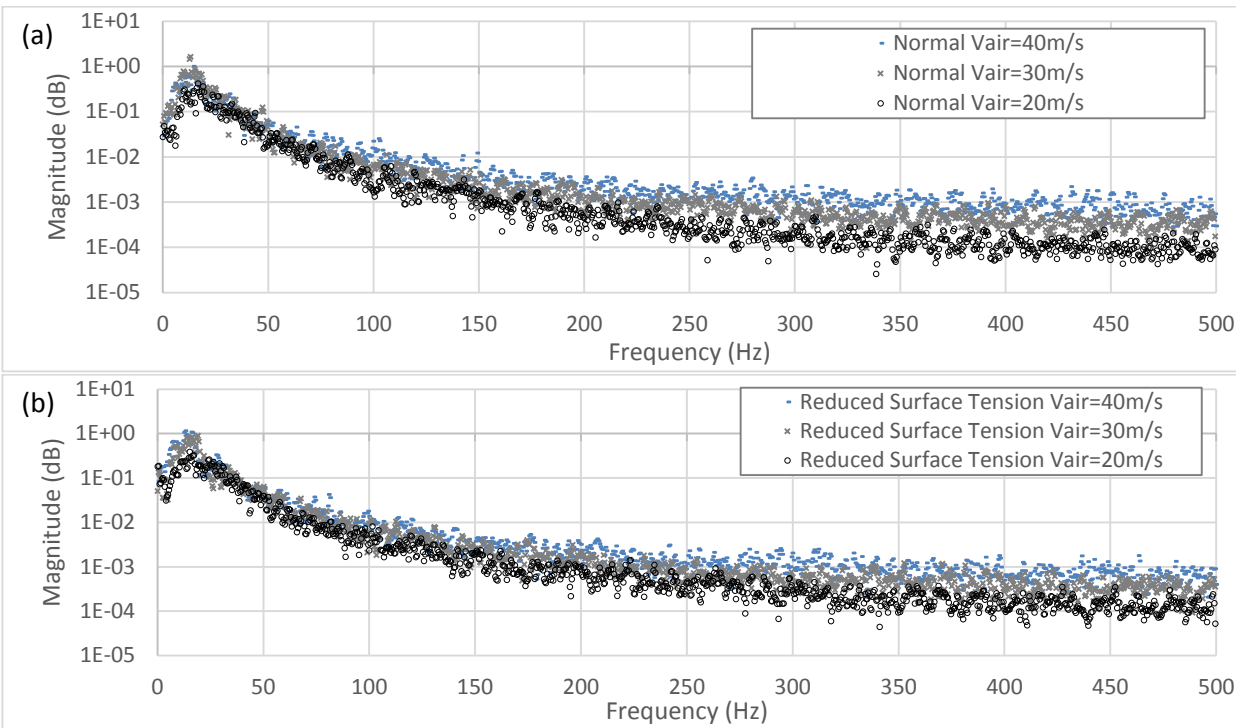
Figure 7-9 Flow channel experiment Welch frequency analysis comparison between Vair = 40 m/s, 30 m/s and 20 m/s of (a) Normal Water (b) Reduced surface tension
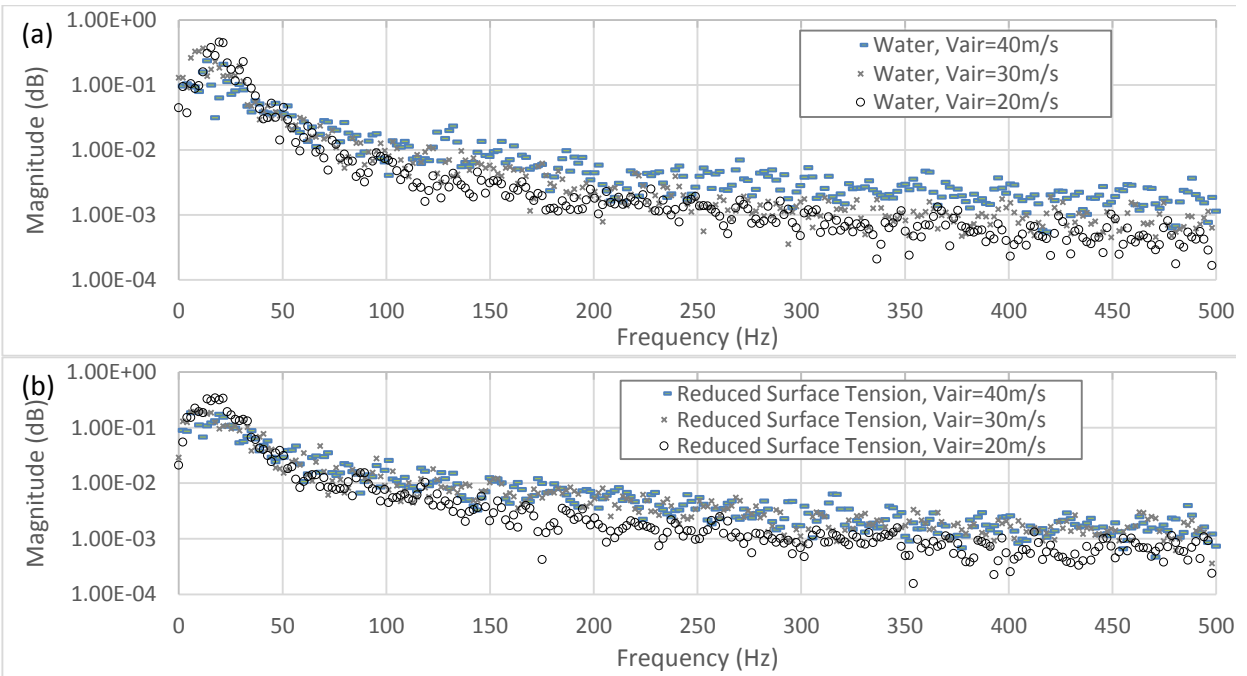
Figure 7-10 Flow channel simulation Welch frequency analysis comparison between Vair = 40 m/s, 30 m/s and 20 m/s of (a) Normal Water (b) Reduced surface tension

Table 7-1 Peak Frequency of experiment and CFD simulation from all cases

	Peak Frequency (Hz)		
	Vair=20m/s	Vair=30m/s	Vair=40m/s
Exp. Normal Water	16.5	13.1	14.1
Exp. Reduced Surface Tension	15.1	16.6	16.1
Sim. Normal Water	19.5	13.6	21.4
Sim. Reduced Surface Tension	15.5	12.7	17.5

7.3 Flow Channel Droplet Volume to Size Distribution Comparison

The flow channel droplet size and volume to size distribution comparison between experiment and 16M cell LES simulation will discussed in this paragraph. The data frame for droplet size information extraction of experiment and simulation are 6,540 msec and 2,000 frames respectively. The result from both experiment and CFD simulation are shown in Figure 7-11 and Figure 7-12. In those figure, the horizontal axis shows droplet size (mm) and volume (mm^3) shown in vertical axis.

It is clear to observe that result from both experiment and simulation has clear difference between different air velocity settings. For cases from higher air velocity setting has greater droplet volume to size distribution curve than those from lower air velocity setting. This result could be explained due to more liquid breakup activity bring by higher air velocity setting. However, the droplet distribution curve level from simulation prediction is less than that from experiment, the reason is due to current 16M cell simulation is insufficient in terms of mesh cell number setup. We already know that the 33M cell simulation shows better potential from result of chapter 6.1, however we need to pick 16M cell simulation as the setting in our study due to reasonable computational time

spend. The 16M cell simulation carried out in this study is already pushing our current research resource to envelop. We recommend to carry out 33M cell simulation or higher in the future if the research resource is enough to carry higher computation loading jobs.
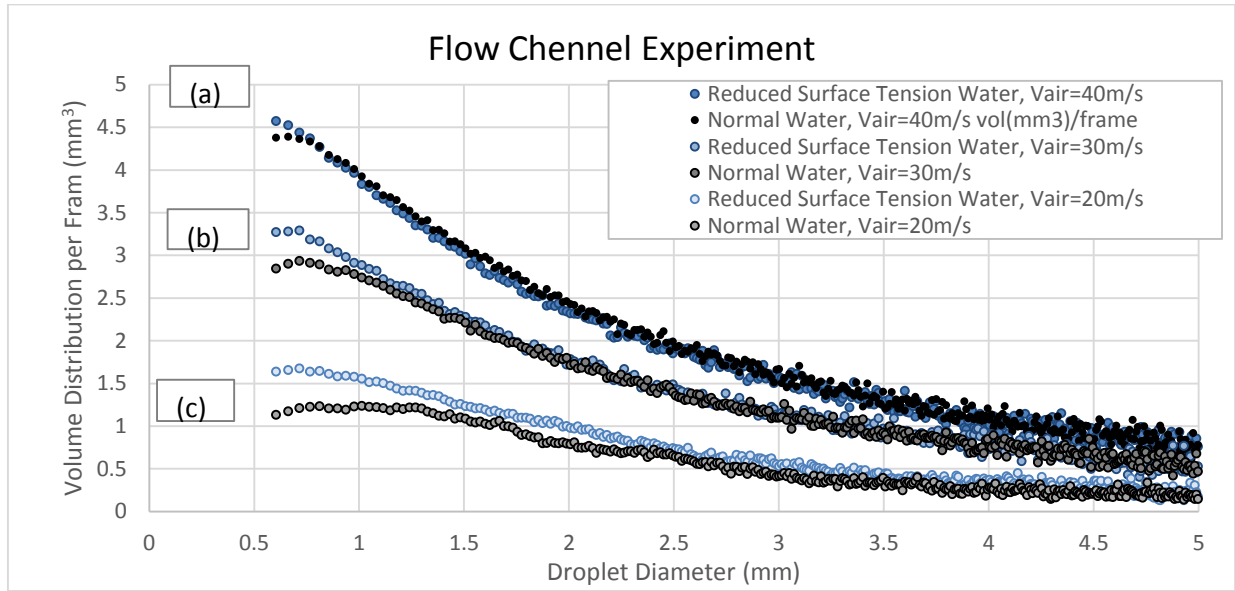
Figure 7-11 Flow channel experiment droplet volume to size distribution comparison between normal water and reduced surface tension water for cases (a) Vair=40m/s, (b) Vair=30m/s and (c) Vair=20m/s.
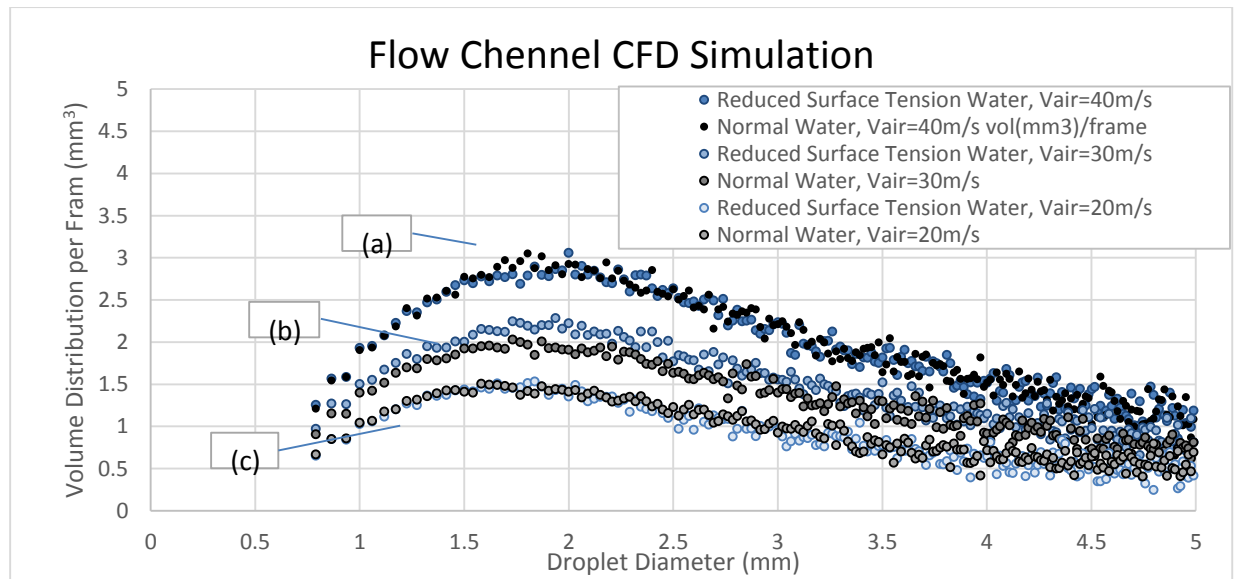
Figure 7-12 Flow channel simulation droplet volume to size distribution comparison between normal water and reduced surface tension water for cases (a) Vair=40m/s, (b) Vair=30m/s and (c) Vair=20m/s.

8 Individual Droplet Breakup Experiment

In this chapter, a precise controlled droplet experiment was carried out. The purposed of droplet experiment is to further explain the potential of enhance liquid breakup behavior by reducing liquid surface tension. Individual droplet breakup experiment provide a micro view to liquid breakup process.

8.1 Droplet Experiment Setup

A schematic of droplet experiment is demonstrated in Figure 8-1. Air pump in the left hand side is use to provide air with velocity of 22.5, 25.0 and 27.5 m/s for liquid breakup test. A droplet release device and liquid flow rate controller is used for generate droplet with size ranging from 1.0 mm to 1.8 mm with 0.1mm increment precisely. When droplet leave the droplet release device, its motion will controlled by gravity and fall perpendicularly to continuous air stream. Three water based liquid with different surface tension will be tested. The surface tension value are 0.074 N/m (water), 0.051 N/m and 0.035 N/m, the value also listed in Table 8-1.

Liquid breakup process have be record by high speed camera operate at 10,000 frame per second. The images from high speed camera will be used for analyzing the data and result.

Table 8-1 Test Liquid properties

	Water	Liquid #1	Liquid #2
Surface Tension (N/m)	0.074	0.051	0.035
Surface Tension (mN/m)	74	51	35
Viscosity (mPa-s) @ 20 ℃	1.0	1.0	1.0
Density (kg/m^3)	996.1	998.0	996.2
Detergent concentration (ppm)	N/A		
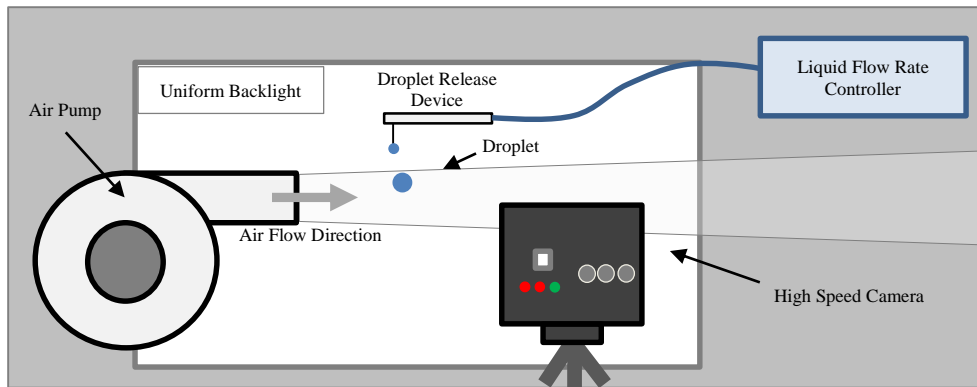
Figure 8-1 Droplet Experiment setup schematic.

8.2 Droplet Experiment Result

The droplet experiment capture image of three different air velocity 22.5, 25.0 and 27.5 m/s. Experiment result are shown from Figure 8-2 to Figure 8-4, respectively. In each of those three comparison figure, droplet size is compared side by side and liquid of three different surface tension are listed from top to bottom. The expose time interval is 1 msec.

Look into the test group of v_{air} = 22.5m/s as shown in Figure 8-2. When droplet size = 1.4 mm, the least surface tension liquid #2 start to breakup, water and liquid #1 shows no sign of breakup. When droplet size increase to 1.5mm the breakup of liquid #2 becomes more active, while water and liquid #1 still shows no sign of breakup. For droplet size equal to 1.6mm liquid #2 shows more active breakup than previous droplet size test, liquid #1 start to breakup as well, meanwhile water shows moderate breakup activity. When the droplet equal 1.7 mm, all three liquid breakup into smaller liquid. We could observe the trend that under same air velocity liquid droplet with lower

125

surface tension value tend to breakup while the size is still small compared to higher surface tension liquid.
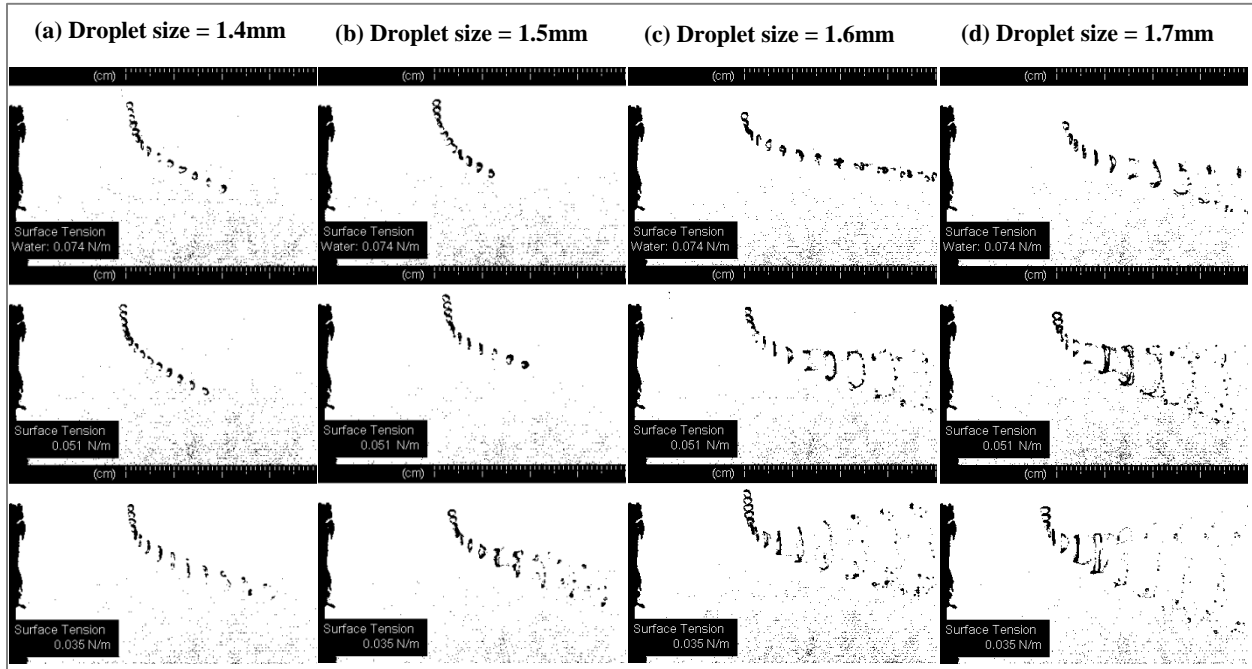
Figure 8-2 Continuous expose image of experiment droplet size of (a) 1.4 mm, (b) 1.5 mm, (c) 1.6 mm, (d) 1.7 mm are tested with Vair = 22.5 m/s and droplet surface tension of 74 mN/m (water), 51 mN/m and 36 mN/m from top to bottom, respectively (time interval = 1 msec).

Look into the test group of $v_{air} = 25.0$m/s as shown in Figure 8-3. When droplet size = 1.2 mm, the least surface tension liquid #2 start to breakup, the breakup size of liquid #2 is 0.2mm smaller comparing to $v_{air} = 22.5$ m/s test group. Water and liquid #1 shows no sign of breakup under same size. When droplet size increase to 1.3 mm liquid #2 is still the only liquid show breakup activity, water and liquid #1 shows no sign of breakup. For droplet size increase to 1.4mm, it could be observe that liquid #2 and liquid #1 start to breakup, meanwhile water shows no sign of breakup activity. When the droplet equal 1.5 mm, all three liquid breakup into smaller liquid.

126

(a) Droplet size = 1.2mm **(a) Droplet size = 1.3mm** **(a) Droplet size = 1.4mm** **(a) Droplet size = 1.5mm**
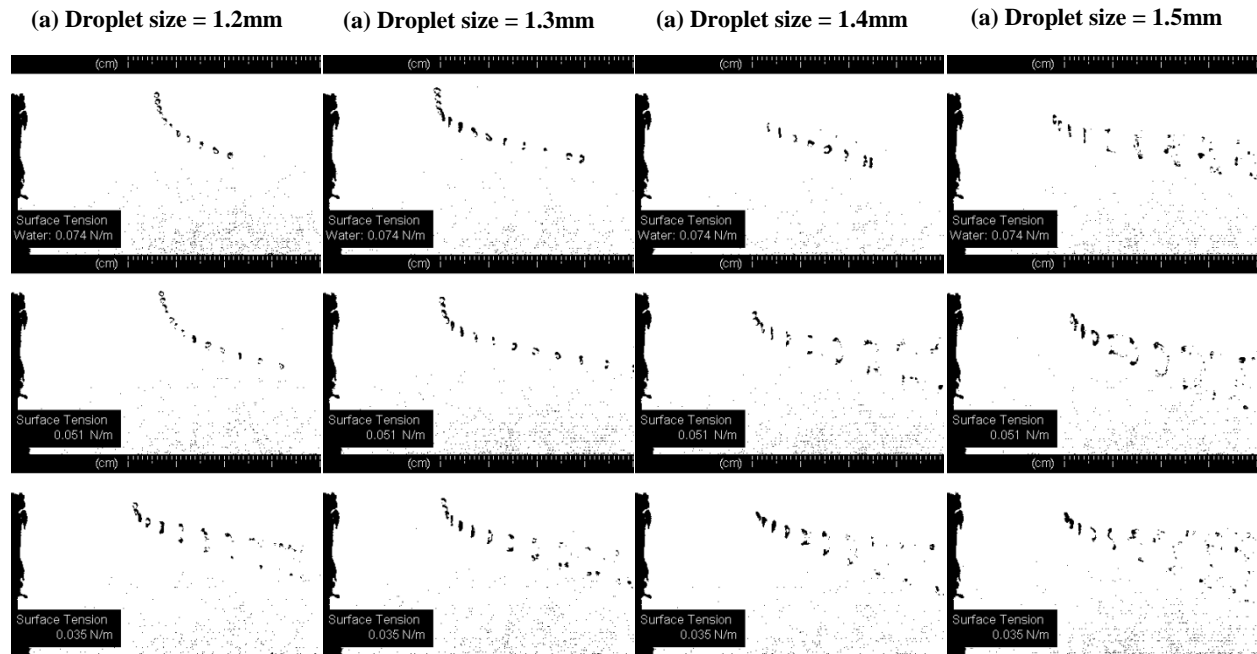
Figure 8-3 Continuous expose image of experiment droplet size of (a) 1.2 mm, (b) 1.3 mm, (c) 1.4 mm, (d) 1.5 mm are tested with Vair = 25.0 m/s and droplet surface tension of 74 mN/m (water), 51 mN/m and 36 mN/m from top to bottom, respectively. (time interval = 1 msec)

Look into the test group of $v_{air} = 27.5$m/s as shown in Figure 8-4. When droplet size = 1.0 mm, the least surface tension liquid #2 start to breakup, the breakup size of liquid #2 is 0.2mm smaller comparing to $v_{air} = 25.0$ m/s test group. Water and liquid #1 shows no sign of breakup under same size. When droplet size increase to 1.1 mm liquid #2 is and liquid #1 show breakup activity, water still shows no sign of breakup. When the droplet size increase to 1.2 mm, all three liquid shows breakup activity. When droplet size reaches to 1.3 mm, all three liquid show breakup activity which is more active than droplet size equal to 1.2mm.

127

(a) Droplet size = 1.0mm **(a) Droplet size = 1.1mm** **(a) Droplet size = 1.2mm** **(a) Droplet size = 1.3mm**
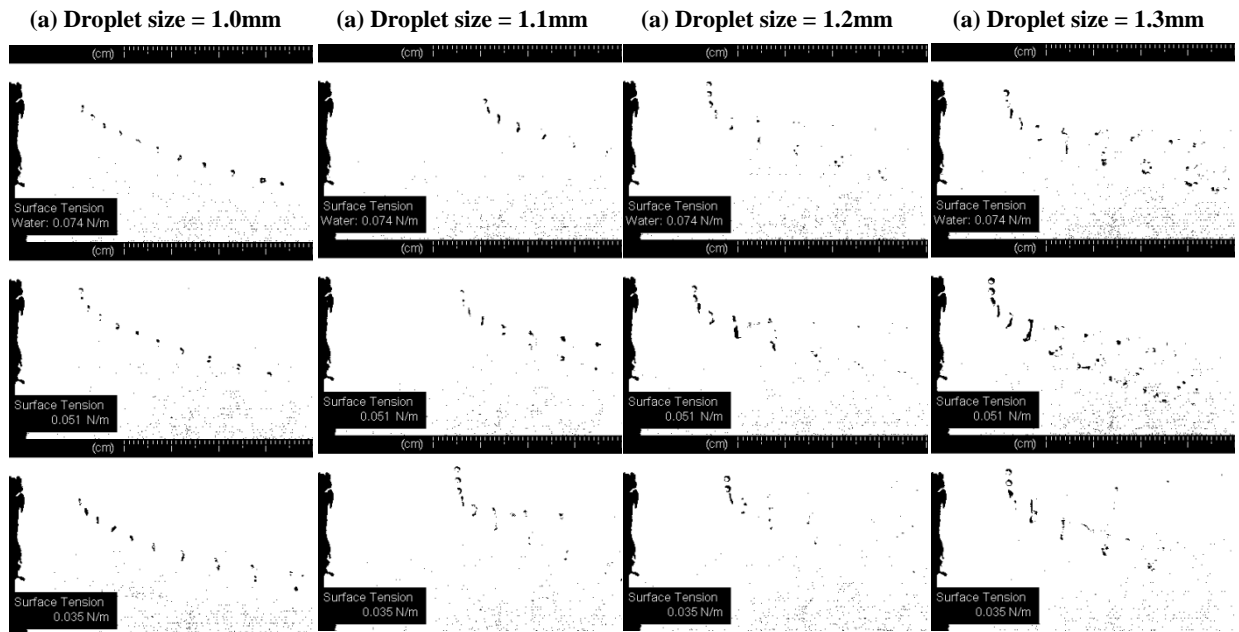
Figure 8-4 Continuous expose image of experiment droplet size of (a) 1.0 mm, (b) 1.1 mm, (c) 1.2 mm, (d) 1.3 mm are tested with Vair = 27.5 m/s and droplet surface tension of 74 mN/m (water), 51 mN/m and 36 mN/m from top to bottom, respectively (time interval = 1 msec).

Overall, smaller droplet is less easy to breakup due to larger Laplace pressure effect documented in chapter 1.7 which defines the droplet bounding pressure is proportional to liquid surface tension and inverse proportional to droplet radius. We observe two trends. First trend is that under same air velocity condition, liquid droplet with lower surface tension value shows breakup activity while droplet size is relative smaller comparing to higher surface tension liquid. The reason is due to Laplace pressure is proportional to surface tension, lower surface tension means lower droplet bounding pressure therefore droplet breakup will occur once external pressure is greater than bounding pressure. Second trend is under same surface tension setup, liquid droplet encountered with higher air velocity will breakup while droplet size is relative smaller comparing to lower air velocity setting.

8.3   Droplet Experiment Result and Conclusion
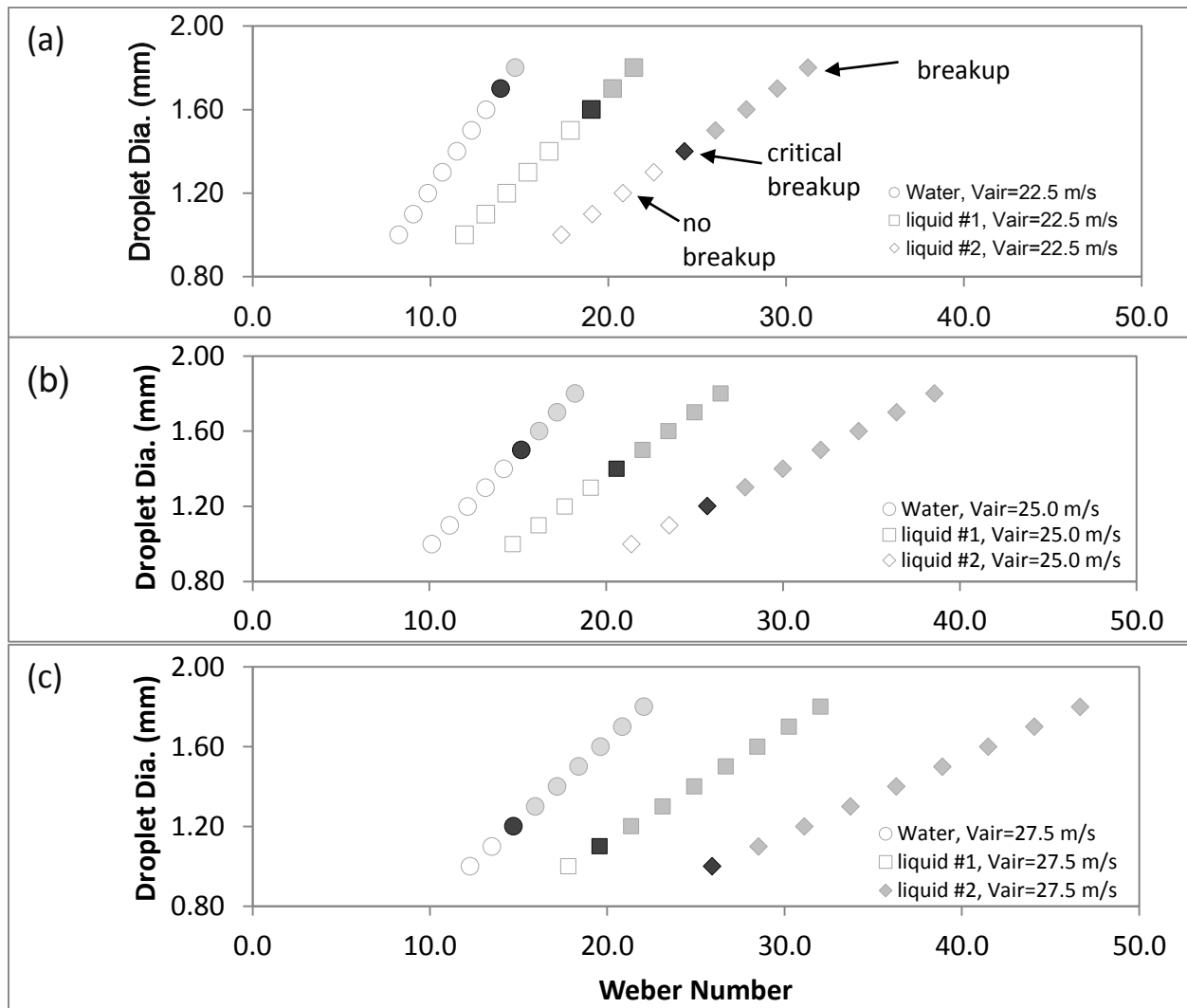
Figure 8-5 Experiment result of droplet size to Weber number with V_air of (a) 22.5 m/s (b) 25.0 m/s (c) 27.5 m/s. Critical breakup case are filled with dark gray. General breakup case are filled with light gray and no fill for no breakup case.

The total experimental result of droplet size to Weber number with different air velocity are shown in Figure 8-5. The critical breakup size is the size which droplet shows the transition from no breakup to liquid breakup phenomenon, and breakup phenomenon will be able to observe for any droplet size larger than critical droplet size. In this figure, Critical breakup case are filled with

black in color. General breakup case are filled with light gray and no fill for the case of no breakup. The critical breakup size for all cases of individual droplet breakup experiment are also listed in Table 8-2. The critical breakup size reduction in percentage compare to water are listed in Table 8-3. Liquid #1 and liquid #2 has surface tension reduction of 31.1% and 52.7% compare to water, the result of average reduction in critical breakup size is 7.0% and 18.1% for liquid #1 and liquid #2, respectively. From the data of this table we could conclude that liquid with lower surface tension will have smaller critical breakup size for all different air velocity setup.

Table 8-2 Critical breakup size in diameter for all cases in individual droplet breakup experiment shown in chapter 8.1

	Water $\sigma = 0.074$ N/m	Liquid #1 $\sigma = 0.051$ N/m	Liquid #2 $\sigma = 0.035$ N/m
Vair = 22.5m/s	1.7	1.6	1.4
Vair = 25.0m/s	1.5	1.4	1.2
Vair = 27.5m/s	1.2	1.1	1.0

Table 8-3 Critical breakup size reduction in percentage compare to water

	Water $\sigma = 0.074$ N/m	Liquid #1 $\sigma = 0.051$ N/m σ: -31.1%	Liquid #2 $\sigma = 0.035$ N/m σ: -52.7%
Vair = 22.5m/s	n/a	-5.9 %	-17.6 %
Vair = 25.0m/s	n/a	-6.7 %	-20.0 %
Vair = 27.5m/s	n/a	-8.3 %	-16.7 %

9 Conclusions and Future Research

The ultimate purpose of this study is to provide a solution to reduce the erosion problem take place at the nozzle region of Solid Rocket Motor (SRM). The SRM erosion problem will lead to thrust performance degradation and flight control difficulties. The erosion process starts due to alumina droplet impingement to the surface of nozzle section of SRM where alumina is the product of oxidized solid fuel of aluminum. Since smaller droplet show the tendency of following gas stream in the combustion chamber rather than impinge to the inner surface to SRM nozzle, the reduction of droplet size will be the key to reduce the level of erosion process at the nozzle region of SRM. In chapter 9.1, the discussion will focus on the main conclusions from two-phase flow channel experiment, CFD simulation and droplet experiment. In chapter 9.2, recommendation for future work research will be discussed.

9.1 Conclusions

9.1.1 Conclusions of Flow Channel Experiment

The purpose of two-phase flow channel experiment is to provide valuable data for liquid droplet breakup study. There are two control variable in this experiment which are the air velocity and surface tension. Three air velocity setting are 20m/s, 30m/s and 40m/s. Two surface tension setting are 0.074 N/m of water and 0.040 N/m for reduced surface tension water. Total control variable combination provide six experiment cases. The result of averaged wave location from all 6 cases

131

indicate the wave location will be lower when air velocity increases, this is due to air with higher velocity carring higher kinetic energy which result in more active liquid breakup behavior. When liquid breakup behavior becomes active, the water level at ramp will be lower due to significant amount of water are carried away from main water body. When comparing the averaged wave location data with different surface tension setup under same air velocity, it could be observed that the reduced surface tension group has lower water level than data from normal water, and this is the evidence of enhanced breakup activity caused by reduced surface tension treatment. The average reduction of water wave location at the top of ramp are 2.8, 2.0 and 3.0% for the case of Vair 20m/s, Vair 30m/s and Vair 40m/s, respectively.

In Welch's frequency analysis section, it is observed that within higher frequency region from 250 Hz to 500 Hz, the magnitude of higher air velocity has greater value than that from lower air velocity cases. The reason of the result is due to higher air velocity induced higher turbulence level causing more fluctuating water surface and lead to higher magnitude in high frequency region. It is also observed that the result from both experiment and simulation, for the magnitude of the cases from Vair=40m/s is about one order greater than that from Vair =20m/s cases. The data of higher frequency region in Welch's analysis could be an indicator for cases from different air velocity condition. It is also observed that the peak frequency are similar for all cases and ranging at lower frequency region of 13Hz~20Hz. The reason is due to same Froude number (Fr) setting in this experiment. Which is defined as fluid velocity over square root of multiplication of gravitational constant and liquid depth. Since all cases has same setup of water depth of 30mm at entrance, the peak frequency will be similar for all cases.

132

The flow channel experiment droplet volume to size distribution comparison provide a valuable data of direct liquid breakup count. From the data, it is clear to distinguish the data difference for the case with different surface tension in the Vair = 20m/s and Vair = 30m/s setup. The result is direct evidence that liquid with lower surface tension get the tendency of more active liquid breakup activity. We didn't observe significant difference between normal water and reduced surface tension water from the result of Vair = 40m/s. After investigation on this case we found that there is too many water droplet overlap to each other in the 3D domain of flow channel for Vair = 40m/s case, and this situation makes the image process tool difficult to recognize droplets. Therefore the droplet volume to size distribution curve will be trustable for the Vair = 20 m/s and 30m/s case. Even though, the data from lower air velocity is still valuable. We found by reducing the surface tension of 45% lead to total volume of droplet increases by around 20% in the flow channel experiment for the Vair = 20m/s case.

Overall, from the experiment of two-phase flow channel, we found the reduction of surface tension enhance the activity of liquid breakup. The flow channel experiment provide an aspect of macro liquid breakup activity and help us understand the droplet volume to size distribution. However, the flow channel cannot provide liquid breakup behavior of individual droplet, therefor droplet experiment is carried out and the conclusion will be discuss in Sec. 9.1.3.

9.1.2   Conclusions of Flow Channel Simulation

The first part of flow channel simulation is the mesh independent study. There are three different mesh setup for performance comparison they are 8M, 16M and 33M cell mesh simulation. Test

condition has same geometry of flow channel experiment. Air velocity setup is 20m/s in the study. From our computational intensive research we found that 33M cell mesh has best performance when compare the droplet volume to size distribution curve to experiment. However each of the computational time of 33M cell mesh took 117 days to finish and this is not practical selection for our study, therefore the final chose is 16M cell mesh simulation. 33M cell or more is recommend if the computational resource is enough in the future.

The second part of simulation is CFD approach selection. Four different CFD approaches of LES, DES k-w, URANS RSM and URANS k-e are testes. Test condition has same geometry of flow channel experiment. Air velocity setup is 20m/s in the study. Liquid droplet volume to size distribution are used for performance comparison. The result shows LES has best performance in terms of two-phase flow liquid breakup simulation. DES k-w is the second option for two-phase flow liquid breakup simulation. URANS approach failed to show liquid breakup under this setup, we do observe the URANS approach show breakup behavior in air velocity = 30m/s, however that is far off from what we have observed in experiment. The final selection is LES approach for the rest of study.

Third part of simulation result is the water surface location history and Welch's frequency analysis. Follows the same setting with experiment, six different cases from combination of two variables of air velocity and surface tension are studied. From the result we could conclude the simulation could show the difference between different air velocity settings, however it is unclear to distinguish the difference made from the variable of surface tension. For the result of Welch's analysis we observe the same result from experiment. The peak frequency for all cases are similar

and ranging at lower frequency region of 13Hz~20Hz. The reason is due to same Froude number (Fr) setting in experiment and simulation.

Final part of the simulation result is compare the droplet volume to size distribution curve. From the result we observe that the distribution curve shows the increasing trend with increasing air velocity. However, curve from simulation is not exactly matches with the curve from experiment. We also observed that the result from 33M cell mesh setup could fit experiment well. The conclusion is 16M cell simulation could predict some two-phase liquid breakup trend, however the mesh density is not enough to well predict all phenomenon observed from experiment. Even though, the total computational time required for six cases simulation are around 6 month under 192 CPU job script in HPC.

Overall, the 16M cell LES simulation shows good prediction trend for different air velocity, but the mesh is nor fine enough to predict the difference from surface tension.

9.1.3 Conclusions of Droplet Experiment

The individual droplet experiment in chapter 8 is to provide a micro scale liquid breakup observation compare to flow channel experiment done in macro scale. Three liquids with different surface tension setup of 0.074 N/m, 0.051 N/m and 0.035N/s was tested with three different air velocity of 22.5m/s, 25.0m/s and 27.5m/s. Liquid #1 and liquid #2 has surface tension reduction of 31.1% and 52.7%, the result of average reduction in critical breakup size is 7.0% and 18.1% for Liquid #1 and liquid #2, respectively. The reduction in critical droplet size is a considerable

number. From the result of all three different air velocity we could conclude that we observe liquid breakup phenomenon takes place earlier at smaller droplet stage for the liquid with lower surface tension. The result shows consistency with flow channel experiment from V air =20m/s and 30m/s.

9.1.4   Post Processing Analyze Tool

The difficulty of studying in two-phase flow is the quantification method. In this study, the quantification is achieved by post processing tool which is developed in UW-Milwaukee Wind Tunnel Lab based on MatLab platform. The code developed include wave location history tool, Welch's Analysis tool, and droplet volume to size distribution tool. Those software tools act as important roles of analyze two-phase flow characters in different conditions. In our study, we success develop and test the MatLab image process quantification tool, our lab will be benefit from the existing code and will extracting more valuable data in the future.

Overall conclusion from this study, it is confirmed that lower the surface tension of liquid will lead to droplet breakup into smaller size. The result could be a good solution for Solid Rocket Motor (SRM) to mitigate the erosion problem at the nozzle section. The reduction of surface tension of liquid aluminum could be achieved by adding magnisium and strontium, it is reported that the surface tension reeducation level could reach 10%~15% when those additive mension above are adding to aluminum.

9.2   Recommendations for Future Research

There is high potential for continue work on the CFD simulation for the research of two-phase flow study. Simulation work could help researcher understand more flow detail which is hard to capture in experiment like velocity, pressure, density for gas phase and liquid phase at any iteration. Those parameter is hard to extract in experiment.

The computational setup of this study is based on a 16 million cell mesh domain operate with Large Eddy Simulation (LES) approach. The 16M LES approach shows decent correlation with experiment result when only compare to the cases with different air velocity setup. However the simulation didn't shows significant difference for liquid with different surface tension cases. We do observe the potential of the LES approach with mesh setup of 33 million cell or more, especially for droplet size and volume curve comparison. It will be promising to setup a LES approach with high number of cell setup in the future.

References

[1] I. S. Grant and W.R. Phillips, in *The Elements of Physics*, Oxford University Press, 2001, pp. 37-38.

[2] W. Von Braun , History of rocketry & space travel, Thomas Y. Crowell Co, 1974.

[3] "History of rockets," NASA, [Online]. Available: https://www.grc.nasa.gov/www/k-12/TRC/Rockets/history_of_rockets.html.

[4] F. Verger, I. Sourbès-Verger, R. Ghirardi, S. Lyle, and P. Reilly, *The Cambridge encyclopedia of space : missions, applications, and exploration*. Cambridge ; New York: Cambridge University Press, 2003.

[5] "Motor 260-Sl-3 Program. Volume 2 - 260-Sl-3 Motor Propellant Development Final Phase Report," NASA, 1967.

[6] S. S. Zumdahl, Introductory Chemistry, Fifth Edition, Brooks Cole, 2006.

[7] A. Davenas, Solid Rocket Propulsion Technology, Pergamon, 1992.

[8] A. C. Cortopassi, E. Boyer and K. K. Kuo, "Update: A Subscale Solid Rocket Motor for Characterization," Denver, Colorado, 2009.

[9] K. Tsiolkovsky, in *The Exploration of Cosmic Space by Means of Reaction Devices (Исследование мировых пространств реактивными приборами)*, 1903.

[10] "Great images in NASA," NASA, 16 03 1926. [Online]. Available: http://grin.hq.nasa.gov/IMAGES/SMALL/GPN-2002-000132.jpg.

[11] R. M. Neilson, The steam turbine, London: Longmans, Green, and Co., 1903.

[12] T. Stevens and M. H. Hobart, Steam Turbine Engineering, MacMillan Company, 1906.

[13] Y.-H. Yen, *The Effects of Optimized Nozzle-Substrate Distance on Cold Gas Dynamic Spray (CGDS) Process,* Milwaukee, WI: University of Wisconsin Milwaukee, 2010.

[14] "Youtube Official NASA Channel: STS-129 HD Launch," NASA, 2009. [Online]. Available: https://www.youtube.com/watch?v=zsJpUCWfyPE.

[15] D. R. Lide and H. V. Kehiaian, CRC Handbook of Thermophysical and Thermochemical Data, CRC Press, 1994.

[16] H. Kim, D. Laredo and D. W. Netzer, "Measurement of Submicrometer Al2O3 Particles in Plume," *Applied Optics,* vol. 32, no. 33, pp. 6834-6840, 1993.

[17] D. D. Joseph, "Breakup of a liquid drop suddenly exposed to a high-speed airstream," Minneapolis, MN, 1999.

[18] "International Agency for Research on Cancer (IARC) - Summaries & Evaluations," International Programme on Chemical Safety (IPCS), [Online]. Available: http://www.inchem.org/documents/iarc/vol58/mono58-1.html.

[19] G. P. Sutton, "Solid Propellants," in *Rocket Propulsion Elements*, John Wiley & Sons, Inc., 1992, p. 436.

[20] T. Kuwahara and N. Kubota, "Role of Boron in Burning Rate Augmentation of AP composite propellants," *Propellants, Explosives, Pyrotechnics,* vol. 14, no. 2, pp. 43-46, 1989.

[21] S. Borass, "Modeling Slag Deposition in the Space Shuttle Solid Rocket Motor," *Journal of Spacecraft and Rockets. Vol 21,* pp. 47-54, 1984.

[22] M. Shorr and A. J. Zaehringer, Solid Rocket Technology, John Wiley & Sons, Inc., 1967.

[23] "Metal Prices.com," 2015. [Online]. Available: http://www.metalprices.com .

[24] S. Heister, "Solid Rocket Motors," in *Space Propulsion Analysis and Sesign*, McGraw-Hill Companies, Inc., 1995, pp. 324-325.

[25] "NASA Report CR-72262 Motor Propellant Developments," NASA, 1967.

[26] Xiao, Y.M.; R.S. Amano, "Aluminized composite solid propellant particle path in the combustion chamber of a solid rocket moter," *Advances in Fluid Mechanics VI, WIT Press,* 2006.

[27] D. C. Rapp, "High Energy-Density Liquid Rocet Fuel Performance," Sverdrup Technology, Inc; NASA Lewis Research Center, Brook Park, Ohio, 1968.

[28] J. Hinze, "Fundamentals of the Hydrodynamic Mechanism of Splitting in Dispersion Processes," *A.I.Ch.E. Journal,* vol. 1, no. 3, pp. 289-295, 1955.

[29] J. Hinze, "Critical Speeds and Sizes of Liquid Globules," *Applied Scientific Research,* pp. 273-288, 1949,.

[30] G. P. Sutton, "Solid Rocket Components and Motor Design," in *Rocket Propulsion Elements*, John Wiley & Sons, Inc., 1992, p. 484.

[31] Thakre, P.; Yang, V., "Chemical Erosion of Refractory-Metal Nozzle Inserts in Solid-Propellant Rocket Motors," *J. Propulsion and Power, Vol. 25, no.1,,* 2009.

[32] E. Y. Wong, "Solid Rocket Nozzle Design Summary," in *4th AIAA Propulsion Joint Specialist Conference*, Cleveland, OH, 1968.

[33] Nayfeh, A. H.; Saric, W. S.;, "Nonlinear Stability of a Liquid Film Adjacent to a Supersonic Stream," *Journal of Fluid Mechanics, Vol. 58,* pp. 39-51, 1973.

[34] M. Salita, "Deficiencies and Requirements in Modeling of Slag Generation in Solid Rocket Motors," *Journal of Propulsion and Power, Vol.11,* pp. 10-23, 1995.

[35] Hess, E.; Chen, K.; Acosta, P.; Brent, D.; Fendell, F.;, "Effect of Aluminized-Grain Design on Slag Accumulation," *Journal of Spacecraft and Rockets, Vol. 29,* pp. 697-703, 1992.

[36] Xiao, Y.; Amano, R. S.; Cai, T.; Li, J, "A New Method to Determine the Velocities of Particles on a Solid-Propellant Surface," *ASME Journal of Heat Transfer, Vol. 127,* pp. 1057-1061, 2005.

[37] Xiao, Yumin, Amano, R.S., Cai, T., and Li, J.,, "Particle Velocity on Solid-Propellant Surface Using X-Ray Real Time Radiography," *AIAA Journal, Vol. 41, No. 9,* pp. 1763-1770, September 2003.

[38] Bandera, A., Maggi, F., and Deluca, L.T.,, "Agglomeration of Aluminized Solid Rocket Propellants," in *45th AIAA/ASME/SAE/ASEE Joint Propulsion Conference & Exhibit*, Denver, Colorado.

[39] R. Holtzmann, "Introduction-The Nature of an Advanced Propellant," Aerojet-General Corporation Von Karman Center, [Online]. Available: web.anl.gov/PCS/acsfuel/preprint%20archive/Files/Volumes/Vol09-1.pdf.

[40] M. Lightfoot, H. Nguyen, S. A. Schumaker, and A. Ebnit, "Shear Driven Liquid Films and Particle Impingement in a Contoured Supersonic Nozzle," 2012.

[41] P. Pokhil, A. Belyayev, Y. Frolov, V. Logachev and A. Korotkov, "Combustion of Powdered Metals in Active Media," Nauka, Moscow, USSR, 1972.

[42] A. Gany and L. H. Caveny, "Agglomeration and ignition mechanism of aluminum particles in solid propellants," *Symposium (International) on Combustion,* vol. 17, no. 1, p. 1453–1461, 1979.

[43] L. Caveny and A. Gany, "Breakup of Al/Al2O3 agglomerates in accelerating flowfields," *AIAA Journal,* vol. 17, pp. 1368-1371, 1979.

[44] J. Happel and H. Brenner, Low Reynolds number hydrodynamics: with special applications to particulate media, Springer Science & Business Media, 2012.

[45] I.-S. Chang, "One-and Two-Phase Nozzle Flow," *AIAA Journal,* vol. 18, pp. 1455-1461, 1980.

[46] C. J. HWANG and G. C. CHANG, "Numerical study of gas-particle flow in a solid rocket nozzle," *AIAA Journal,* vol. 26, pp. 682-689, 1988.

[47] X. Yumin and A. S. Ryoichi , "X-ray real time radiography technique to determine the velocities of particles on the solid propellant surface," in *39th Aerospace Sciences Meeting and Exhibit*, Reno,NV, 2001.

[48] X. Yumin and A. Ryoichi, "Particle Velocity on Solid-Propellant Surface Using X-Ray Real-Time Radiography," *AIAA Journal,* pp. 1763-1770, 2003.

[49] P. Gentil, "Design and Development of a New Solid Rocket Motor Nozzle Based on Carbon and Carbon-Ceramic Materials," in *AIAA Joint Propulsion Conferences*, Boston,MA,U.S.A., 1988.

[50] Y. Yavor, V. Rosenband and A. Gany, "Reduced Agglomeration in Solid Propellants Containing Porous Aluminum," in *4th European conference for aerospace sciences*, 2011.

[51] V. Rosenband and A. Gany, "High-Reactivity Aluminum Powders," in *8th International Symposium on Special Topics in Chemical Propulsion*, Cape Town, South Africa, 2009.

[52] I. F. Bainbridge, and J. A. Taylor, "The surface tension of pure aluminum and aluminum alloys," *Metallurgical and Materials Transactions A,* pp. 3901-3909, 2013.

[53] J. Anson, R. Drew and J. Gruzleski, "The surface tension of molten aluminum and Al-Si-Mg alloy under vacuum and hydrogen atmospheres," *Metallurgical and Materials Transactions B,* pp. 1027-1032, 1999.

[54] E. River, V. Moureau, M. Garcia, T. Poinsot and O. Simonin, "Evaluation of numerical strategies for large eddy simulation of particulate two-phase recirculating flows," *Journal of Computational Physics,* pp. 539-564, 2009.

[55] J. Borée, T. Ishima and I. Flour, "The effect of mass loading and inter-particle collisions on the development of the polydispersed two-phase flow downstream of a confined bluff body," *Journal of Fluid Mechanics,* pp. 129-165, 2001.

[56] P. Auerkari, "Mechanical and physical properties of engineering alumina ceramics," VTT Manufacturing Technology, Espoo, Otaniemi, Finland, 1996.

[57] P.-F. Paradis and T. Ishikawa, "Surface Tension and Viscosity Measurements of Liquid and Undercooled Alumina by Containerless Techniques," *Japanese Journal of Applied Physics,* vol. 44, 2005.

[58] "UW Milwaukee High Performance Computing," University of Wisconsin Milwaukee, [Online]. Available: http://www4.uwm.edu/hpc/about/specifications.cfm.

[59] Hirt, C.W., Nichols, B.D., "Volume of fluid (VOF) method for the dynamics of free boundaries," *Journal of Computational Physics 39 (1),* pp. 201-225, 1981.

[60] G. W. R. B. E. Launder, "Progress in the development of a Reynolds-stress turbulence closure," *Journal of Fluid Mech,* vol. 68, no. 3, pp. 537-566, 1974.

[61] J. Smagorinsky, "GENERAL CIRCULATION EXPERIMENTS WITH THE PRIMITIVE EQUATIONS I. THE BASIC EXPERIMENT," *American Meteorological Society,* vol. 91, no. 3, pp. 99-164, 1963.

[62] F. Nicoud and F. Ducros, "Subgrid-Scale Stress Modelling Based on the Square of the Velocity Gradient Tensor," *Flow, Turbulence and Combustion,* vol. 62, no. 3, pp. pp 183-200, 1999.

[63] P. D. Welch, "The use of fast Fourier transform for the estimation of power spectra: A method based on time averaging over short, modified periodograms," *IEEE Transactions on audio and electroacoustics,* pp. 70-73, 1967.

[64] "Specific Impulse," National Aeronautics and Space Administration, [Online]. Available: http://www.grc.nasa.gov/WWW/K-12/airplane/specimp.html.

142

Appendix

Tsiolkovsky rocket equation

The rocket equation derivation is start in equation (43) from Newton's third law

$$M\frac{d\,V}{d\,t} = -v_e\,\frac{d\,M}{d\,t} - Mg \tag{43}$$

where M is the mass of rocket system, V is the velocity of rocket, v_e is the velocity of exhaust gas and g is standard gravity constant, by multiplying equation (43) by dt and dividing by M, leading to

$$-v_e\,\frac{d\,M}{M} - g\,dt = dV \tag{44}$$

Assume V=0 when lift-off at t=0, the mass of rocket is initially M_i and reduce to M_f at a time t_f with speed reach to V_f after fuel is burnt. Integrating equation (44)

$$-v_e \int_{M_i}^{M_f}\frac{d\,M}{M} - g \int_{0}^{t_f} dt = \int_{0}^{V_f} dV \tag{45}$$

and perform the integration of equation (45) we get

$$V_f = v_e ln \frac{M_i}{M_f} - g\, t_f \qquad (46)$$

equation (46) is also known as Tsiolkovsky rocket equation named after Russian scientist Konstantin Tsiolkovsky who derived it and published it in 1903 [9]. Form the result of equation (46) the speed v_e of exhaust gas must be high and the ratio M_i/M_f is considerably larger than one and t_f must be small, which means the fuel must be burnt as quickly as possible to give large final velocity.

Specific Impulse

When a rocket is working, the total impulse of rocket I_t is the thrust force F integrated over the burning time t.

$$I_t = \int_0^t F\, dt \qquad (47)$$

The definition of specific impulse I_{sp} is the total impulse per unit weight of propellant. If the total mass flow rate of propellant is $\dot{m}$ and the gravity of Earth at sea-level is g_0, then.

$$I_{sp} = \frac{\int_0^t F \, dt}{g_0 \int_0^t \dot{m} \, dt} \tag{48}$$

For constant measure of the thrust performance of unit fuel mass, by rearrange equation (48) we could express the specific impulse into

$$I_{sp} = \frac{F}{\dot{m} \, g_0} \tag{49}$$

This equation will give a time-averaged specific impulse value for any rocket propulsion system, higher specific impulse indicate higher exhaust gas velocity under same amount of propellant, less propellant is needed to produce a given thrust during a given time and more efficient in terms of fuel consumed by weight [64].

Isentropic Flow of an Ideal Gas

The reason of convergent divergent duct could accelerate gas to supersonic velocity could be derived by area variation for isentropic flow of an ideal gas.

$$\dot{m} = \rho A V \tag{50}$$

$$\frac{d\rho}{\rho} + \frac{dA}{A} + \frac{dV}{V} = 0 \tag{51}$$

$$\frac{dA}{A} = -\frac{dV}{V} - \frac{d\rho}{\rho} \tag{52}$$

$$\frac{dA}{A} = -\frac{dp}{\rho V^2} - \frac{d\rho}{\rho} \tag{53}$$

$$\frac{dA}{A} = -\frac{dp}{\rho V^2}\left[1 - \frac{V^2}{(dp/d\rho)}\right] \tag{54}$$

$$\frac{dA}{A} = -\frac{dp}{\rho V^2}\left[1 - \frac{V^2}{c^2}\right] = \frac{dp}{\rho V^2}[1 - Ma^2] \tag{55}$$

146

$$\frac{dp}{\rho V^2} = \frac{dA}{A} \frac{1}{[1 - Ma^2]} \tag{56}$$

$$\frac{dV}{V} = -\frac{dA}{A} \frac{1}{[1 - Ma^2]} \tag{57}$$

Drag Coefficient Equation

The drag coefficient equations used are:

$$C_D = \frac{24.}{Re} \text{ for } Re < 0.1;$$

$$C_D = 3.69 + \frac{22.73}{Re} + \frac{0.0903}{Re^2} \text{ for } 0.1 < Re < 1;$$

$$C_D = 1.222 + \frac{29.1667}{Re} - \frac{3.8889}{Re^2} \text{ for } 1 < Re < 10.;$$

$$C_D = 0.6167 + \frac{46.5}{Re} - \frac{116.67}{Re^2} \text{ for } 10. < Re < 100.;$$

$$C_D = 0.3644 + \frac{98.33}{Re} - \frac{2778}{Re^2} \text{ for } 100. < Re < 1000.;$$

$$C_D = 0.357 + \frac{148.62}{Re} - \frac{4.75 * 10^4}{Re^2} \text{ for } 1 * 10^3 < Re < 5 * 10^3;$$

$$C_D = 0.46 - \frac{490.546}{Re} + \frac{57.87 * 10^4}{Re^2} \text{ for } 5 * 10^3 < Re < 1 * 10^4;$$

$$C_D = 0.5191 - \frac{1662.5}{Re} + \frac{5.4167 * 10^6}{Re^2} \text{ for } 1 * 10^4 < Re < 5 * 10^4;$$

Image Process Code for Particle Volume to Size Distribution Information extraction

```matlab
%% Created by Yi-Hsin Yen 2016/02/23 @ 410 W Hampton
clear all; clc; close all;
%% Crop Status
%a00=a0;
    crop=[400, 90,870, 250];
    %a00=a0;
    %a00(:,crop(1) )=0;
    %a00(:,crop(1)+crop(3))=0;
    %a00(crop(2),:)=0;
    %a00(crop(2)+crop(4),:)=0;
    %imshow(a00);
%% 00 2nd back
%back0=imread('C:\Users\OneNew\Desktop\Matlab_Prelime\image\back_2.TIF');
%back1(:,:,1)=back0(:,:,1);
%back2=imcomplement(back1);
%% 00 <-----------------------------------------------------main
% Select right Folder in the following path
    %%%%%%%%%%
        spd=40;% <----change varialbe to locate folder (20,30,40)
    %%%%%%%%%%
folder = ['D:\Simulation_research\08_EXP\0RDST\02_Crop\', num2str(spd),'\'];
folder_imout_01=['D:\Simulation_research\08_EXP\0RDST\07_Status\',
num2str(spd),'\'];
figure_name=['Exp_RDST_', num2str(spd),'_'];
folder_out=['D:\Simulation_research\08_EXP\0RDST\07_Status\data\Exp_RDST_',
num2str(spd),'_1.xlsx'];
%folder = 'C:\Users\OneNew\Desktop\image\';
Files = dir(folder);
filename = {Files.name};
isdir = [Files.isdir];
filename(isdir) = [];

s = listdlg('ListString', filename);
filename = filename(s)';
jFL=length(filename);
image_number=j;
%% --------------[variable initialization]
m=1;
Np_t=0;
plot=1;%plot yes(1) or no(0),<---------------------[Check Plot]

ecc_filter=0.8; % <-------------------------[Set Eccentric filter]

thresh=200; % <------------------------[image filter (255 black,0 white)]
%% 01 image show
ttot=cputime;
```

149

```matlab
for m = 1:jFL;
tpic=cputime;
file = [folder '\' filename{m}];
    a0 = importdata(file);
  %   imshow(a0)
    %b0=a0;           %b is preserved, a is copy

%% 02 Crop region 2 water
               %[left top right Butom]
a1=imcrop(a0,[crop(1) crop(2) crop(3) crop(4)]);
% imshow(a1)
%a1_1=a1_1+back2;
%% 03 Segment by thresholding

a2=im2bw(a1,thresh/255);
%figure;
% imshow(a2)

%% 04 Clean up image
% Morphology can assit segmentation
% Remove small objects less then 5 pxl.
a3=bwareaopen(a2,4);
%imshow(a3)
%% 05 Complement
a4=imcomplement(a3);
%imshow(a4)
%% 05_2 Complement Clean up image
% Morphology can assit segmentation
% Remove small objects less then 5 pxl.
a5=bwareaopen(a4,4);
%imshow(a5)

%% 06 Find Boundary and Label
%holse, noholes,
%t=cputime;
[B,L]=bwboundaries(a5,'noholes');
% Get Labeled information
Status=regionprops(L,'Area','Eccentricity','EquivDiameter');
numReg=max(L(:));

%% 06_2 Ecc Check
Ecc_ck=cell2mat({Status(:).Eccentricity});


if plot==1; % if plot =1, plot droplet

% 07 Plot boundary
t=cputime;
clear a7;
%a7(476,681)=0;
a7=cat(3,a1,a1,a1);
```

```matlab
lenB=length(B);  % total number of particles

for j=1:lenB
    if Ecc_ck(j)<ecc_filter;

        bdl=B{j};        % find total boundary coordinate location
        len=length(bdl);

            for i=1:len % plot boundary loop
            a7(bdl(i,1),bdl(i,2),1)=1;
          % a7(bdl(i,1),bdl(i,2),2)=0.1;
            end
    else

    end

end


t=cputime-t;
imshow(a7)

 %08 combine plot boundary to a0
sza7=size(a7);
a8=cat(3,a0,a0,a0);
a8(crop(2):crop(2)+crop(4),crop(1):crop(1)+crop(3),1)=a7(1:sza7(1),1:sza7(2),
1);
imwrite(a8,[folder_imout_01,figure_name,num2str(10000+m),'.tif']);
else % belong to if plot command
end  % belong to if plot command
%% 09 assign data to cell
lenB=length(B);
Np_t=Np_t+lenB;
%info_Area(1:lenB,m)=(cell2mat({Status(:).Area}))';
info_Ecc(1:lenB,m)=cell2mat({Status(:).Eccentricity})';
info_Dia(1:lenB,m)=cell2mat({Status(:).EquivDiameter})'; % collacting data,
frames is in colume

%% remove large value in info (that is water body)

clear Status;
tpic=cputime-tpic;
fprintf(['process ', num2str(10000+m),'.tif with CPU Time of ',
num2str(tpic),' sec\n'])
end
%% Tabulate
ttot=cputime-ttot;
info_Dia2=single(info_Dia); % convert matrix to single precision
info_Ecc2=single(info_Ecc);
%info_Area2(info_Area2>10000)=0;  % clear oversize object
sz_info_A=size(info_Dia); % get matrix size
```

```matlab
info_Dia_v=reshape(info_Dia2,sz_info_A(1)*sz_info_A(2),1); % reshpe matrix to
single colume
info_Ecc_v=reshape(info_Ecc2,sz_info_A(1)*sz_info_A(2),1);
%--------screen particle ecentricity

info_Ecc_v2=info_Ecc_v;
info_Ecc_v2(info_Ecc_v2<ecc_filter)=1.1;
info_Ecc_v2(info_Ecc_v2<1)=0;
info_Ecc_v2(info_Ecc_v2>1)=1;  % screen matrix
%--------
info_Dia_v2=info_Ecc_v2.*info_Dia_v;

tul=tabulate(info_Dia_v2); % Tabulate info_Dia


pxl=4.17; %4.1pxl=1mm
tul(:,4)=tul(:,1)/pxl;     % convert Diameter to mm
 tul(:,5)=((tul(:,4)/2).^3)*(4*pi/3); % Volume of droplet
 tul(:,6)=tul(:,5).*tul(:,2)/jFL;  % total volume carried by droplet by
particular size
% add image process information log
tul(2,8)=ecc_filter; % Eccentricity filter
tul(3,8)=Np_t; % Total number of detected particles
tul(1,2)=0; % # of 0 particle is 0
tul(1,3)=0; % # of 0 particle is 0
tul(4,8)=sum(tul(:,2)); %calculate total particle # to compare with filted #
tul(5,8)=100*tul(4,8)/tul(3,8); % percentage of particle in analyse
tul(6,8)=jFL;     %number of inage analyse
tul(7,8)=thresh; %image contrast threshold
tul(8,8)=ttot; % total time used
%tul(1,1)='Area'
% [   1   ] [    2    ] [ 3 ]    [    4    ]    [    5    ]    [     6
]
% size (pxl)|| count ||  %   ||   Dia (mm)  ||  acumulate Vol ||  mass
distribution per frame
%% Final output
%xlswrite('C:\Users\OneNew\Desktop\test_image\out\20m_s_dropCunt.xlsx',info);
%xlswrite('D:\Simulation_research\00_PhD_Mesh_ind\07_Drop_Status\Excel\exp_Ar
ea.xlsx',info_Area2);
%xlswrite('D:\Simulation_research\00_PhD_Mesh_ind\07_Drop_Status\Excel\exp_Ec
centricity.xlsx',info_Ecc);
%xlswrite('D:\Simulation_research\00_PhD_Mesh_ind\07_Drop_Status\Excel\exp_Eq
vDia.xlsx',info_EqvDia);
xlswrite(folder_out,tul);


fprintf(['Total CPU Time of ', num2str(ttot),' sec\n'])
```

Free Surface Location History Extraction Code

```matlab
%% Created by Yi-Hsin Yen 2016/03/10 @ 410 W Hampton Ave
clear all; clc; close all;

%% 00
% Select right Folder in the following path
V=40;
n=['Nom'];
folder = 'D:\Simulation_research\08_EXP\0',n,'\02_Crop\',num2str(V),'\';
folder_out=['D:\Simulation_research\08_EXP\0',n,'\07_Status\',num2str(V),'\']
;

Files = dir(folder);
filename = {Files.name};
isdir = [Files.isdir];
filename(isdir) = [];

s = listdlg('ListString', filename);
filename = filename(s)';
jFL=length(filename);
image_number=j;
m=1;
%%
%ttot=cputime;
        %[left top left+ top+]
location=[692 280 100 200];
l=location;

%% 01 image show
for m = 1:jFL;
tpic=cputime;

file = [folder '\' filename{m}];
%%
a0 = importdata(file);
  % a0=rgb2gray(a0);
%imshow(a0)
      %b0=a0;         %b is preserved, a is copy
for i=1:3
      a1(:,:,i)=a0;
end
a1(l(2):l(2)+l(4),l(1):l(1)+l(3),1)=200; %location=l

%imshow(a1)
%% 02 Crop region 1 top
              %[Y     X           ]
              %[left top left+ top+]
a1_0=imcrop(a0,[location(1) location(2) location(3) location(4)]);
%figure;
%imshow(a1_0)
```

```matlab
%% 03 Segment by thresholding
% Becomes Logical Image
% select which level be included into black reigon,127 is defalt value,225
% is complet dark
%mn=min(a1_0);
thresh=90;
a2_0=im2bw(a1_0,thresh/255);%thresh and below are black
cus=10;%clean_up_size
a2_0=bwareaopen(a2_0,cus);
a2_0=imcomplement(a2_0);
a2_0=bwareaopen(a2_0,cus);
a2_0=imcomplement(a2_0);
%figure;
%imshow(a2_0);
%imwrite(Partic,[folder_out,'Image3.tif']);
%clear thresh;


%% 05 Complement
a3_0=imcomplement(a2_0);
%imshow(a3_0);
%a=imc;
%imwrite(a,[folder_out,'Image5.tif']);

%% 06 Find Boundary and Label
%holse, noholes,
%t=cputime;
[B,L]=bwboundaries(a3_0);
% Get Labeled information
Status=regionprops(L,'Area','Centroid');
%numReg=max(L(:)); % count the tot # of Label
%imshow(label2rgb(L))
%imwrite(a,[folder_out,'Image6_2.tif']);
%t=cputime-t
%% calculate object in test colume
num=length({Status(:).Centroid}); % particle number
Psz=cell2mat({Status(:).Area});
[M,I] = max(Psz);% return max indel
%% loop of overcome white region
Bsz=length(B);
if Bsz==0;
    dmax(m,:)= dmax(m-1,:); % if no object, use privious location.
else
BM=(B{I});
 szB=length(BM);
  for i=1:szB
  if BM(i,2)~=1
      BM(i,1)=1;
  end
  end
%dmax0=max(BM); % find particle I
```

```matlab
        data(m,1)=max(BM(:,1)); % list particle size for each frame m

    end
%clear Bsz;
%clear data0;
%clear Ar0;
%clear k;
%data(m,1)=dmax_k;
%% Test
% find boundary of BM
%a5=cat(3,a1_0,a1_0,a1_0);
%for i=1:113
%    a5(BM(i,1),BM(i,2),1)=255;
%end
%imshow(a5);

%% Adding Red Dot on location <---------------------------------------o
a4=cat(3,a0,a0,a0);
%% kk
for i=1:10
    for j=1:10
        %[left top left+ top+]
a4(location(2)+(data(m,1))+i-6,location(1)+j-6,1)=255;
a4(location(2)+(data(m,1))+i-6,location(1)+j-6,2:3)=0;
    end
end
imshow(a4);
%% kk

imwrite(a4,[folder_out,'Image_',n,'_',num2str(V),'_',num2str(m+10000),'.tif']
)
clear i j a4;


fprintf(['processing ', num2str(m),' pic\n']);
end

%%
%ttot=cputime-ttot;
%fprintf(['Total CPU Time of ', num2str(ttot),' sec\n'])
SZa0=size(a0);
data1=SZa0(1)-l(2)-data; % Vetical pxl - top-down location
xlswrite(folder_out,'\data\',n,'_',num2str(V),'_Frequency.xls',data1)
plot(data1);
```

Free Surface Location History Extraction Code

```matlab
% 151022 @ 401 W Hamptom
clear all, clc;


%% Select right Folder in the following path
folder =
'D:\Simulation_research\00_PhD_Mesh_ind\05_1_wave_location\Z_data\1ms';
%folder_out='G:\Photron\150201_Ramp\40m_s\0-80\1_image\1_cut\';
Files = dir(folder);
filename = {Files.name};
isdir = [Files.isdir];
filename(isdir) = [];
s = listdlg('ListString', filename);
filename = filename(s)';
jFL=length(filename);
%%
for i = 1:jFL;
t_in=cputime;
      file = [folder '\' filename{i}];
      a = xlsread(file);
 sz=size(a);
%% Data collector of all xls files
m(1)=mean(a);
a=a-m(1);
Data_raw(1:sz(1),i)=a(1:sz(1));
 end
 %% Truncate Data
clear Data;
start_location=500;
Data(1:1000,1)=Data_raw(start_location:start_location+999,1);
 %% Pre FFT
 Fs = 1000;                      % Sampling frequency
T = 1/Fs;                       % Sample time
L = sz(1);                       % Length of signal
t = (0:L-1)*T;                  % Time vector
% Sum of a 50 Hz sinusoid and a 120 Hz sinusoid
%x = 0.7*sin(2*pi*50*t) + sin(2*pi*120*t);
%y = x + 2*randn(size(t));       % Sinusoids plus noise
%plot(Fs*t(1:1000),a(1:1000))
%title('Signal Corrupted with Zero-Mean Random Noise')
%xlabel('time (milliseconds)')

%% FFT
%clf;
%NFFT = 2^nextpow2(L); % Next power of 2 from length of y
%Y = fft(a,NFFT)/L;
%f = Fs/2*linspace(0,1,NFFT/2+1);

% Plot single-sided amplitude spectrum.
```

```matlab
%plot(f,2*abs(Y(1:NFFT/2+1)))
%title('Single-Sided Amplitude Spectrum of y(t)')
%xlabel('Frequency (Hz)')
%ylabel('|Y(f)|')
 %% Welch
%clf;
%hold on;
for i = 1:jFL;
[pxx,f] = pwelch(Data(:,i),[],[],[],Fs);
szpxx=size(pxx);
PXX(1:szpxx(1),i)=pxx(1:szpxx(1));

figure;
plot(f,10*log10(PXX(:,i))); axis([0 500 -30 20]);
%plot(f,10*log10(PXX(:,i))); axis([0 50 -10 10]);
%plot(f,(PXX(:,i))); axis([0 100 0 10]);

xlabel('Frequency (Hz)')
ylabel('Magnitude (dB)')
end

%hold off;

%% Post process of PXX

for i=1:szpxx(1)
PXX2(i,1)=mean(PXX(i,1:2));
PXX2(i,2)=mean(PXX(i,3:4));
PXX2(i,3)=mean(PXX(i,5:6));
end

hold on;

  plot(f,10*log10(PXX2(:,1)),'black:'); axis([0 500 -40 10]);
  plot(f,10*log10(PXX2(:,2)),'black--');
  plot(f,10*log10(PXX2(:,3)),'color',[0.5,0.5,0.5]);

xlabel('Frequency (Hz)')
ylabel('Magnitude (dB)')
%legend('Exp V air=20m/s','Exp V air=30m/s','Exp V air=40m/s');
legend('Sim V air=20m/s','Sim V air=30m/s','Sim V air=40m/s');

hold off;


%% xls write
 %PXX3(:,1)=f;
%PXX3(:,2:4)=PXX2(:,1:3);
xlswrite('D:\Simulation_research\00_PhD_Mesh_ind\06_Frequency_Welch\1.0ms\Wel
ch_xls_EXP07',PXX);
```

Curriculum Vitae

Yen, Yi-Hsin (顏，一新)

Place of Birth: Kaohsiung, Taiwan (高雄，臺灣)

Education

- Ph.D. Candidate in Mechanical Engineering, May 2016
  University of Wisconsin-Milwaukee, Milwaukee, USA

  Dissertation: Experiment and Simulation Study of Liquid Breakup Process in Solid Rocket Motor

- Master of Engineering in Mechanical Engineering, May 2010
  University of Wisconsin-Milwaukee, Milwaukee, USA

  Thesis: The effects of optimized nozzle –substrate distance on Cold Gas Dynamic Spray (CGDS) process

- Bachelor of Science in Physics 2006
  TungHai University, Taichung, Taiwan

Industrial Experience

- June 2014 – Present, Ph.D. CFD Engineer Co-op, Harley-Davidson Motor Company, Wauwatosa, Wisconsin, US

- June 2012-Aug 2012, Phillips Healthcare (Dunlee) summer intern, Aurora, Il, US
  University of Wisconsin-Milwaukee, Milwaukee, USA

Research Experience

- June 2014 – Present, U.S. DoE Hydro-Turbine Project. (DOE: DE-FOA-0001227), Cadence, UW-Milwaukee Joint Project Research Assistance, University of Wisconsin-Milwaukee, WI, USA.

- June 2013-Dec 2013, U.S. Air Force Solid Rocket Motor Project Research Assistance, UW-Milwaukee Joint Project, University of Wisconsin-Milwaukee, WI, USA.

Teaching Experience in University of Wisconsin-Milwaukee, WI, USA

- ME 150 How Things Work, Jan 2009-May 2011

- ME 321 Basic Heat Transfer Sep 2011-May 2012

- ME 110 Engineering Fundamentals, Sep 2012-May 2013

- ME 323 Fluid Mechanics Lab, Sep 2013-May 2014

Award and Activity

- Execute Officer of UW-Milwaukee American Institute of Aeronautics and Astronautics (AIAA) in 2013

- Vice-President of UW-Milwaukee Taiwanese Student Association in 2009

- UW-Milwaukee Chancellor Award 2008

Publications

Y. Yen, R.S. Amano ," Investigation of Alumina Flow Breakup Process in Solid Rocket Propulsion Chamber," AIAA SciTech 2016 January, San Diego, CA, USA

R.S. Amano , Y. Yen, "Study of Alumina Flow in a propulsion Chamber," 2015 Propulsion and Energy, Orlando, Fl, USA

R.S. Amano , Y. Yen, "Study of Liquid Breakup Mechanism in Solid Rocket Motor Nozzle," 2015 ICJWSF, Stockholm, Sweden

Amano, R., Yen, Y-H., Hamman, "Study of Liquid Breakup Process in Solid Rocket Motor Nozzle" AIAA SciTech 2015 January, Kissimmee Fl, USA

Amano, R., Yen, Y-H., Hamman, M,. Peng, C-H,. "Study of Two Phase Flow on Solid Rocket Motor Nozzle" FEDSM2014-21256 August3-7, 2014, Chicago, Il, USA

Amano, R., Yen, Y-H., Hamman, Rocky, K., Stangelj, J., M,. Peng, C-H,. "Experimental validation of numerical Model for Liquid Phase Breakup in Solid Fuel Rockets" FEDSM2014-21224 August3-7, 2014, Chicago, Il, USA

Yi-Hsin Yen, Sung-Cheng Wong, Tien-Chien Jen, Qinghua Chen, Quan Liao, "The Effects of Optimized Nozzle-Substrate Distance on Cold Gas Dynamic Spray (CGDS) Process," IMECE2010-37536, ASME November, 2010, Vancouver, Canada

Tien-Chien Jen, Sung-Cheng Wong, Yi-Hsin Yen, "Thermal Analysis of The Particle Critical Velocity on Bonding Efficiency in Cold Gas Dynamic Spray Process," IMECE2010-37723, ASME November, 2010, Vancouver, Canada.

Book Chapter

Amano, Ryoichi S., Yi-Hsin Yen, and Michael L. Hamman. "Solid-Fuel Rocket Motor Efficiency Improvement Scheme." Novel Combustion Concepts for Sustainable Energy Development. Springer India, 2014. 535-560.